A NOVEL CHARACTERIZATION OF ORGANIC POLYMER INTERFACES USING REMOTE-GATE FIELD-EFFECT TRANSISTORS

by
Hyun-June Jang

A dissertation submitted to Johns Hopkins University in conformity with the requirements for the degree of Doctor of Philosophy

Baltimore, Maryland

March, 2020

Abstract

The scope of this work is to establish fundamental characterization of diverse reactions occurring at organic polymer interfaces using a remote-gate field-effect transistor (RGFET) system. Reactive interfaces are placed on a RG module, which is in turn translated by a Si-FET transducer that has an electrical connection with the RG module. Specifically, the Si-FET translates electrical potential perturbations resulting from specific reactions on the RG module as changes to threshold voltage of the RGFET system ($V_{th,RG}$). Basic semiconductor physics describing how $V_{th,RG}$ is changed by electrical potential perturbations is introduced in Chapter 1.

In Chapter 2, we discuss the RGFET characterization of molecular doping effects in a conductive polymer and physical diffusion in a passive polymer. A poly(3-hexylthiophene) (P3HT) film (hosting p-type semiconductor) is prepared on the RG module. $V_{th,RG}$ is reduced as solution concentration of 2,3,5,6-tetrafluoro-7,7,8,8-tetracyanoquinodimethane (F4TCNQ), p-type dopant, is increased on the P3HT RG surface. A new calculation method has been devised to calculate the induced hole concentrations and mobilities in doped P3HT films, using this $\Delta V_{th,RG}$. Meanwhile, the FET analysis tool offers a means of monitoring the physical diffusion of small molecules, exemplified by F4TCNQ, in the passive polymer polystyrene, driven by concentration gradients.

In Chapter 3, the RGFET system discriminates crucial mechanistic factors in an electrochemical drift occurring at polymer-solvent interfaces. We discuss a slow reorientation of dipoles at the interface induced by gate electric fields. The effects of orientational ordering on drift are studied on various RG surfaces, including indium tin

oxide (ITO), SiO_2, hexamethyldisilazane (HMDS)-treated SiO_2, polystyrene (PS), and poly(styrene-co-acrylic acid) (PSAA). Conductive and charged components on the surface decrease drift by promoting fast, stable arrangement of dipoles at the interface. Conjugated polymers such as P3HT and poly [3-(3-carboxypropyl) thiophene-2,5-diyl] (PT-COOH) display insignificant drift in aqueous media.

In Chapter 4, concentration-dependent electronic response to cortisol in physiological condition is demonstrated by introducing an antibody-embedded polymer on the RGFET system. The embedded structure of the receptor in polymer alleviates Debye screening length (λ_D) limitations that appear in the alternative surface-functionalized-polymer architecture. As a result, we accomplish a preliminary demonstration of cortisol detection in a lightly buffered artificial sweat that showed limit of detection of 1 ng/ml.

Official readers

Professor Howard E. Katz

Professor Patricia McGuiggan

Dedication

Dedicated to my family & friends.

Acknowledgement

Infinite thanks to all my mentors, advisors, and colleagues.

Table of Contents

List of Tables

List of Figures

Chapter 1

Chapter 2

Chapter 3

Chapter 4

Chapter 1

Threshold voltage model for RGFET

1.1. Introduction

1.1.1. Metal-oxide-semiconductor field-effect transistor

Since the advent of the prototype junction metal-oxide semiconductor field-effect transistor (MOSFET) at Bell Labs in 1959,[1] the MOSFET has gradually evolved as a basic building block of modern electronics and is one of the most frequently manufactured devices in history. Now, several billion MOSFETs are integrated in a single microprocessor, introducing a number of new functions to the basic computing systems in conjunction with other circuit elements.[2]

The heart of the MOSFET is a metal-oxide-semiconductor (MOS) structure known as a MOS capacitor that consists of a metal electrode, an insulating layer, and a semiconductor substrate (assuming p-type silicon in the following case) as illustrated in Figure 1.1.

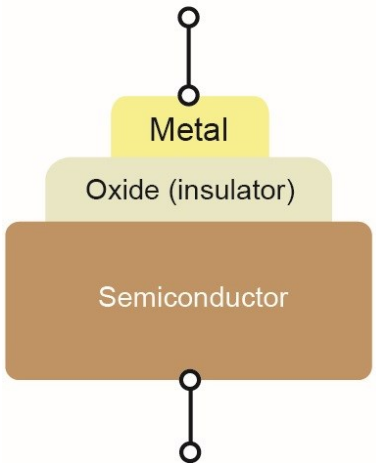

Figure 1.1. The basic MOS capacitor structure.

The metal electrode is typically referred to as the gate where the voltage is typically applied. There is no current flow through the MOS capacitor because of an extremely high input resistance from the presence of the insulator. Gate electric fields produced by the gate voltage (V_G), however, are transmitted through the insulator up to the semiconductor substrate. To be specific, the positive gate voltage holds electrons at the interface between p-type semiconductor and the insulator, which is called an inversion layer because they are oppositely charged to the majority of hole carriers that prevail in a p-type semiconductor. In contrast, an accumulation layer indicates hole carriers collected by the negative gate voltage.

The band theory of semiconductor is a way to describe this detailed mechanism. When atoms come together to form a compound, their atomic orbitals mix to form molecular orbitals. If more atoms are added to a system, more molecular orbitals start to overlap in energies. At this time, it is expected that many of these energy levels will be in great proximity or even completely degenerate. These energy levels in turn form bands of energy. At this point, an energy bandgap may appear where no electron states can exist. There is an energy level where electrons are actually occupied, called a valence band (E_v). The electrons at the valence band can jump up into a conduction band (E_c) when electrons are excited from the valence band. The Fermi level (E_F) is a hypothetical energy level that would have a 50% probability of being occupied at any given time. The position of the Fermi level can be changed by introducing different charge carrier densities in individual material or changing doping concentrations in a semiconductor. In the case of metals, there is no band gap due to a large population of delocalized electrons. Also, E_F of metals is equal to their E_c.

The energy band diagram of the MOS capacitor with a p-type semiconductor is described in Figure 1.2. E_F of a p-type semiconductor lies close to E_v. In contrast, E_F would appear close to E_c in the case of n-type semiconductors. The energy bands in the semiconductor near the oxide semiconductor interface are bent by the positive V_G across the MOS capacitor as shown in Figure 1.2. That is, the gate electric field varies the surface potential (ϕ_s) at the oxide semiconductor interface. ϕ_s is defined as the difference between E_{Fi} measured in the bulk semiconductor and E_{Fi} measured at the surface.

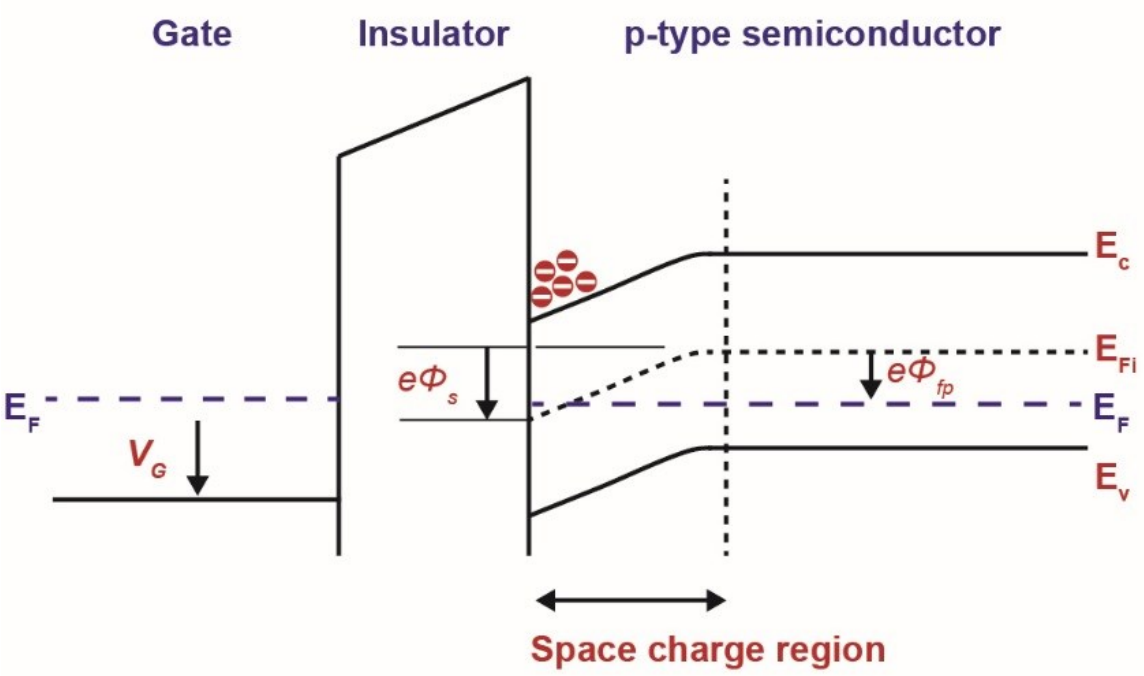

Figure 1.2. The energy-band diagram of MOS structure with a p-type semiconductor and a positive gate voltage applied through the gate at equilibrium. E_c: conduction level, E_v: valence level, E_F: Fermi level, E_{Fi}: intrinsic E_F without doping.

Accordingly, the characteristic of the semiconductor surface is inverted from p-type to n-type by making a very thin inversion layer of electrons at the semiconductor-oxide interface. Despite this being a p-type semiconductor, E_F is closer to E_c at the interface between the insulator and the semiconductor than that to E_v.

The only difference in device structure between the MOS capacitor and the MOSFET is that the MOSFET incorporates two additional terminals, called source (S) and drain (D), between which horizontal current flows at the semiconductor-oxide interface, as illustrated in Figure 1.3. The source of current is derived from electrons inverted by the positive gate voltage. If the inversion layer consists of electrons, we call it an n-channel MOSFET.

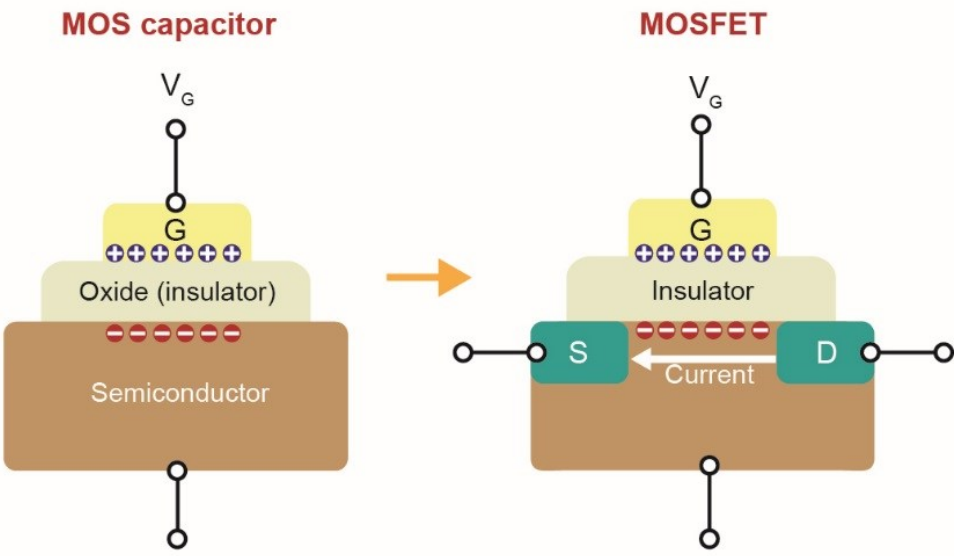

Figure 1.3. The basic MOFSET structure.

The threshold voltages (V_{th}) is the applied gate voltage required to create the inversion layer charge, which is one of the most important parameters of the MOSFET. Figure 1.4 shows charge distribution through a MOS capacitor with a p-type semiconductor substrate at the threshold voltage inversion point. Positive charges appear at the metal surface because of an application of positive gate voltages, designated as the region "a". Other positive charges have been typically shown at the region "b" at the interface between the insulator and the semiconductor due to charge trapping densities. Negative charges at the region "c" are the inverted electrons in the semiconductor resulting from the applied gate electric field. The charges at region "a", "b", and "c" are termed as Q_G, Q_{ox}, and Q_{semi}, respectively.

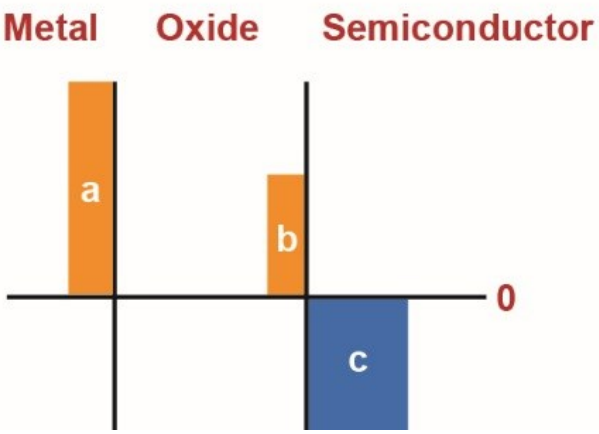

Figure 1.4. Charge distribution in a MOS capacitor with a p-type semiconductor at the threshold voltage point. Charges at the region "a", "b", and "c" are termed as Q_G, Q_{ox}, and Q_{semi}.

The net charge from each plate of a capacitor is zero. Therefore, the relationship between Q_G, Q_{ox}, and Q_{semi} is written:

$$Q_G + Q_{ox} = Q_{semi}$$

The gate voltage across the oxide (V_{ox}) at the threshold inversion point is related to the charge on the gate and to the oxide capacitance by

$$V_{ox} = \frac{Q_G}{C_{ox}} = \frac{1}{C_{ox}}(Q_{semi} - Q_{ox}) \qquad (1.1)$$

Except for the applied electric field, there is an additional factor that largely affects the levels of electrical potentials at the gate, which is the difference in work function between the gate (ϕ_m) and the semiconductor (ϕ_{semi}). The work function is the energy difference between Fermi level and vacuum level. Fermi level, however, should universally stay constant for connected systems between different materials in thermal equilibrium because all properties of materials existing in a system in thermal equilibrium will be independent of time. Accordingly, energy band structures of the MOS capacitor vary as a function of the difference in work functions between ϕ_m and ϕ_{semi}, denoted as ϕ_{ms}.

Figure 1.5 shows the energy-band diagram of cases when (a) $\phi_m > \phi_{semi}$, (b) $\phi_m = \phi_{semi}$, and (c) $\phi_m < \phi_{semi}$ in thermal equilibrium without the applied gate voltage (i.e. when $V_G = 0$ V). At this time, we assume that there are no charge traps between the

insulator and the semiconductor. The only variable in this system is work function of the gate.

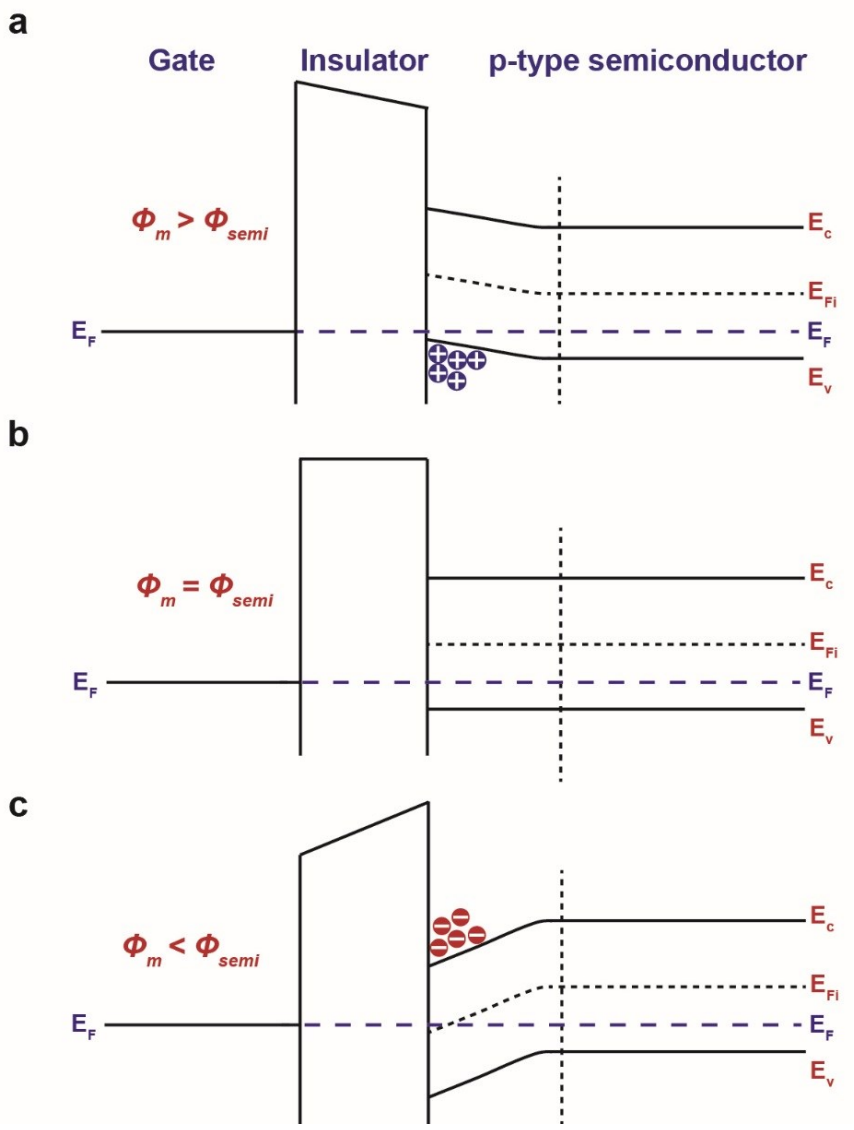

Figure 1.5. The energy-band diagram of cases of (a) $\phi_m > \phi_{semi}$ (b) $\phi_m = \phi_{semi}$, and (c) $\phi_m < \phi_{semi}$ without applications of the gate voltage in thermal equilibrium.

The case (a) demonstrates that hole carriers are naturally accumulated at the semiconductor-insulator interface. If $\phi_{ms} = 0\ eV$ (case (b)), there is no band bending in the semiconductor. When $\phi_m < \phi_{semi}$, the conduction level of E_c is closer to E_F, indicating the presence of inverted electrons at the semiconductor interface.

Hence, the total potential energy (V_{total}) actually applied across the MOSFET system has two components: (1) applied gate voltage and (2) additional electrical potentials associated with ϕ_{ms}. Total potential energy will be dropped to insulator (V_{ox}) and the surface potential (ϕ_s) at silicon-insulator interface, respectively, which can be written as:

$$V_{total} = V_G - \phi_{ms} = V_{ox} + \phi_s \qquad (1.2)$$

We introduce the definition of potential ϕ_{fp} which is the difference between E_{Fi} and E_F at the bulk region of the semiconductor and is given by:

$$\phi_{fp} = \frac{kT}{q} \ln\left(\frac{N_a}{n_i}\right) \qquad (1.3)$$

where k is Boltzmann constant, T is absolute temperature, q is electric charge, N_a is acceptor doping concentration, and n_i is the intrinsic carrier concentration of a semiconductor. That is, ϕ_{fp} is the potential difference at the bulk region resulting from doping, relative to that of intrinsic semiconductor. The schematic definition of ϕ_{fp} is also shown in Figure 1.2. The threshold inversion point is also quantitatively described as the condition when the surface potential is $\phi_s = 2\phi_{fp}$.

At the threshold inversion point, $V_G = V_{th}$. Therefore, in equation (1.2), we have[3]:

$$V_{th} = V_{ox} + \phi_s + \phi_{ms} \qquad (1.4)$$

By combining equation (1.1), (1.3), and (1.4) together, we finally have a classic definition of threshold voltage of the MOSFET expressed as:

$$V_{th} = \frac{1}{C_{ox}}(Q_{semi} - Q_{ox}) + \frac{2kT}{q}\ln\left(\frac{N_a}{n_i}\right) + \phi_{semi} - \phi_m \quad (1.5)$$

According to the developed equation (1.5), there are three imperative factors that could change the threshold voltage of the MOSFET: (1) capacitance of insulator (C_{ox}). This is further related to dielectric constant and thickness of insulator. In case of n-channel MOSFETs, high C_{ox} reduces V_{th} of the MOSFET, meaning that the MOSFET turns on easier. (2) Doping concentrations of semiconductor associated with N_a and ϕ_{semi}. Heavily-doped p-type semiconductors result in increased V_{th}. (3) Work function of gate ϕ_m. A high work function of the gate electrode results in the increased V_{th}[4] but without changes in the shape of transfer curves of the MOFSET as shown in Figure 1.6.

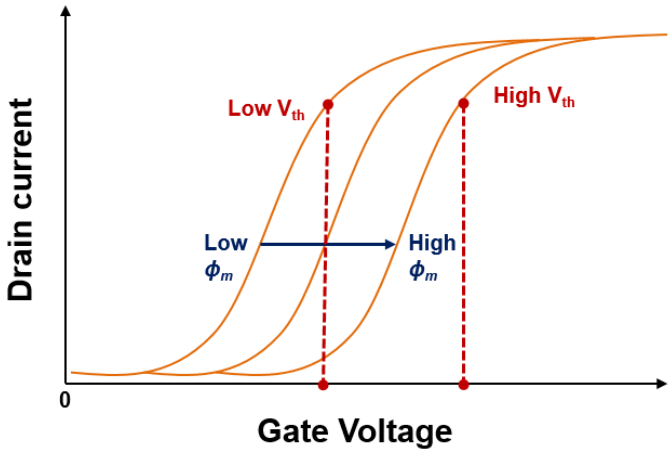

Figure 1.6. Schematic image of shifts in transfer curve (on semi-log scale) as a function of ϕ_m.

Figure 1.6 is an example of how the MOSFET responds to changes in the electrical potential at the gate. This property of MOSFETs has opened new frontiers for their application in memory devices and in a wide variety of state-of-the-art sensors. That is, ϕ_m in equation (1.5) implicates diverse functionality of the MOSFET.

We could rewrite V_{th} in equation (1.5) by combining two separated systems associated with (1) insulator/semiconductor (V_{FET}) and (2) latent variables at the gate, expressed as $f(G)$ that could be transformed for diverse objectives as:

$$V_{th} = V_{FET} + f(G) \qquad (1.6)$$

where $V_{FET} = \frac{1}{C_{ox}}(Q_{semi} - Q_{ox}) + \frac{2kT}{q}\ln\left(\frac{N_a}{n_i}\right) + \phi_{semi}$ and $f(G) = -\phi_m$ in this case.

1.1.2. Ion-sensitive FET

In this section, the application of the MOSFET as an electrochemical sensor is introduced. An ion-sensitive FET (ISFET) was first reported by Bergveld in 1970[5], which has been used for measuring ion concentrations in solution. The interaction between ions and amphoteric surface sites on sensing membranes provokes variations of surface potential, which leads to changes in V_{th} of the ISFET ($V_{th,ISFET}$). The device geometrics of the ISFET originated from that of the MOSFET. The metal gate electrode of the MOSFET is replaced by a solution system incorporating an ion-sensitive membrane, electrolyte solution, and solution gate as shown in Figure 1.7. An Ag/AgCl reference electrode has been widely used for the solution gate.

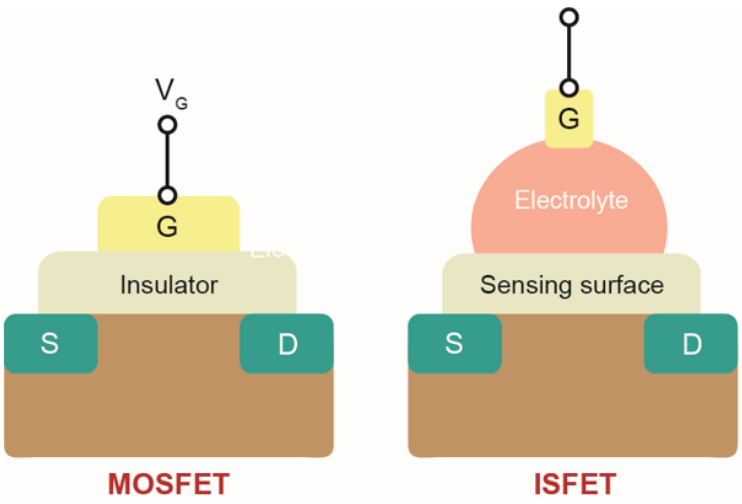

Figure 1.7. The basic ISFET structure

The ISFET was the first FET biosensor as well. A sensing surface in Figure 1.7 is typically ion-sensitive but can be functionalized with diverse specific targeting moieties

for applications of the ISFET to biosensors.[6] Since the advent of the ISFET, a great deal of attention has been paid to the development of FET biosensors because of numerous advantages such as high sensitivity, fast response time, miniaturization, low–cost manufacturing, and label-free detections.

The ISFET operational mechanism is deeply associated with the theoretical backgrounds of the MOSFET because the ISFET is a special type of MOSFET. We further expand equation (1.6) to express $V_{th,ISFET}$ from now on. There is no difference in the system regarding insulator/semiconductor between the ISFET and MOSFET except that the ISFET incorporates an electrochemical environment at the gate. Assume any variation in electrical potentials comes from the electrochemical environment as V_{chem}. For this case, $f(G) = V_{chem}$ in equation (1.6) and $V_{th,ISFET}$ is:

$$V_{th,ISFET} = V_{FET} + V_{chem} \qquad (1.7)$$

V_{chem} is described as[7]:

Electrolyte/sensing surface terms

$$V_{chem} = E_{ref} + \phi_{lj} - \varphi_s + \chi_{sol}$$

Reference electrode terms

where E_{ref} is absolute potential of the reference electrode, χ_{sol} is the electrolyte insulator surface dipole potential, φ_s is the surface potential at the electrolyte/sensing film interface,

and ϕ_{lj} is the liquid junction potential difference. Implicitly, the ϕ_m term existing in equation (1.6) is already included in V_{chem}, differently, expressed as E_{ref} and ϕ_{lj}. All parameters in equation for V_{chem} remain consistent except for φ_s.

According to the site-binding model, φ_s for proton concentrations is expressed as[8]:

$$\varphi_s = \frac{kT}{q} \ln\left(\frac{aH^+_{bulk}}{aH^+_{surface}}\right)$$

where a denotes the proton activity in the bulk electrolyte and at the gate dielectric-electrolyte interface. That is, change in φ_s is the actual driving force of threshold voltage shift in the ISFET. Hence, the shift in threshold voltage of ISFET is given by:

$$\Delta V_{th,ISFET} = -\Delta\varphi_s$$

The ISFETs, however, displayed chronic problems in device stability and reliability for long-term use. This is because the insulating oxide between the silicon and the solution is slowly penetrated by various ions such as OH^- or Na^+, causing a change in the characteristics of the device, or malfunction, resulting in poor thermal stability of the ISFET. Furthermore, the ISFET with no metal gate has undesirable sensitivity under light since the light is transmitted to the semiconductor across the insulator. This means that noise factors are enhanced in the ISFET structure in the presence of light. Additionally, the transducing part in the ISFET is not reusable because the sensing surface is directly

fabricated on the semiconductor, inferring that complex FET fabrication processes should be repeated for other use.

1.1.3. Remote-gate FET

To address disadvantages of ISFETs, the remote-gate FET (RGFET) was first proposed by J. Van der Spiegel in 1983.[9] The RGFET stemmed from the ISFET structure is shown in Figure 1.8.

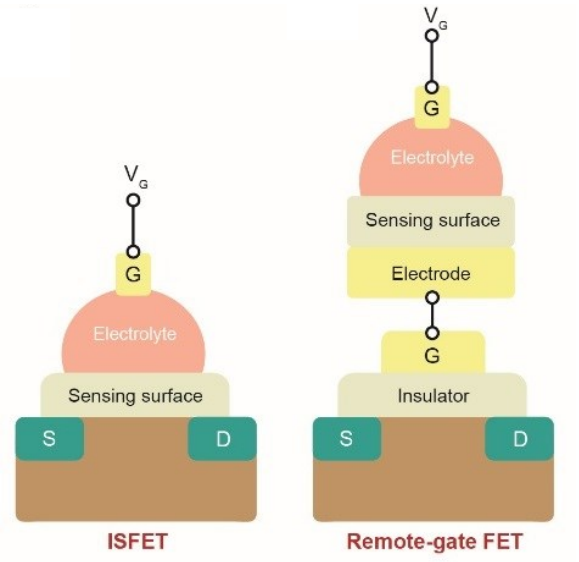

Figure 1.8. The basic RGFET structure.

The RGFET is electrically combined with two separated parts of the MOSFET and a remote-gate (RG) module. The RG module is simply coupled to the gate of a typical MOSFET. By adopting the RGFET structure, the solution system that largely incorporates unstable factors is totally isolated from the transducing system. Nonetheless, any variation in electrochemical potentials on the RG module is transferred up to the gate of the

MOSFET. Hence, the RGFET has more advantages such as low cost, simple structure, easy packaging, long term stability, insensitivity to light and temperature as well as disposability of the gate compared to the ISFET.[10]

We can define V_{th} of the RGFET ($V_{th,RG}$) by modifying equation (1.7) developed for $V_{th,ISFET}$. Most factors remain the same except for the RG module. The RGFET has three separated systems: (1) MOSFET, (2) solution system, and (3) RG module. $V_{th,RG}$ would be a combination of individual parts as shown below:

$$V_{th,RG} = V_{th,FET} + V_{chem} + f(RG) \qquad (1.8)$$

where $V_{th,FET}$ is threshold voltage of the MOSFET and $f(RG)$ is a function possibly including variables of electrical potential and impedance associated with intrinsic properties of the RG material. $V_{th,FET}$ in our RGFET system remains consistent throughout all the experiments discussed in this thesis, since the same commercial silicon MOSFET was used. The property of V_{chem} is already discussed in Chapter 1.1.2. We will figure out what factors exist in $f(RG)$ terms especially in our RGFET system in the following sections.

1.2. Results and Discussion

1.2.1. Factors to make change in $V_{th,RG}$

In order to understand equation (1.8) systematically, we first evaluate basic electrical properties of the MOFSET transducer (CD4007UB) used for our RGFET. The MOSFET is totally isolated from the solution system and RG module. Basic transfer curves

of the MOSFET are evaluated in Figure 1.9a. For this, we repeated measurements of transfer curves for 100 cycles with a double sweep mode at the V_G ranges from 0 to 5 V. Drain voltage (V_D) was set at 50 mV. No observable change in transfer curves was recorded during the measurement. $V_{th,FET}$ is tracked over time as shown in Figure 1.9b. $V_{th,FET}$ of 1.5 V remains constant during repeating measurements. Also, $V_{th,FET}$ of the MOSFET measured by each forward and reverse sweeping mode completely overlaps, revealing the ideal behavior as a reliable transducer.

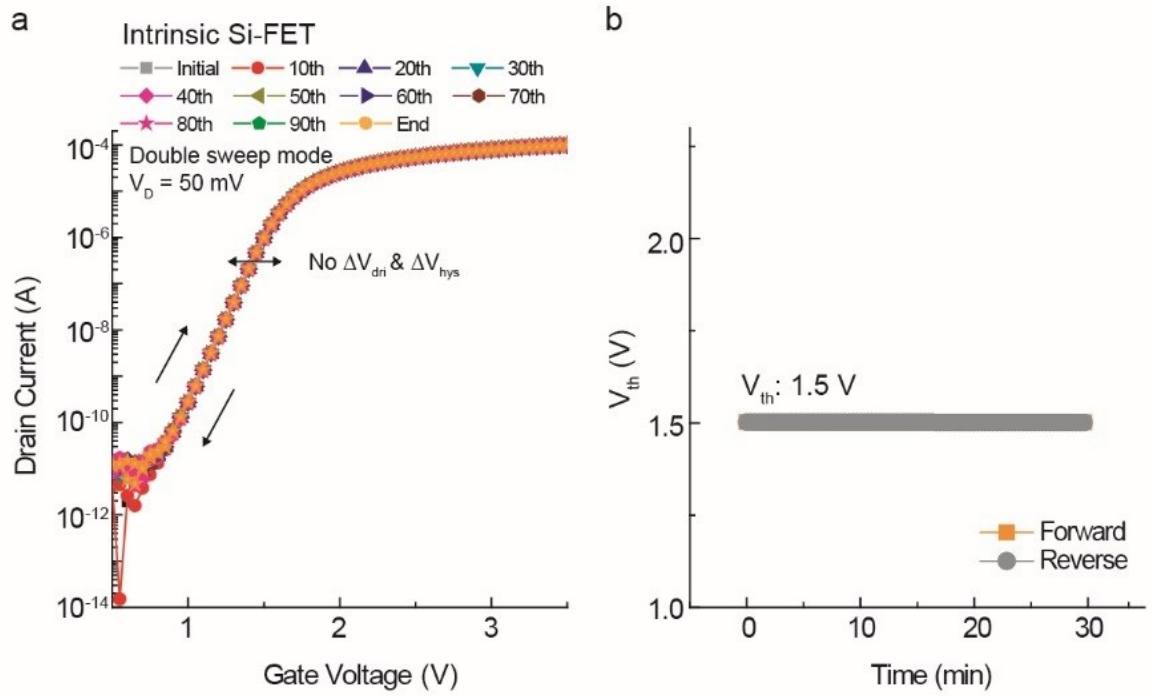

Figure 1.9. (a) Zoomed-in representative transfer curves of Si-FET with the double sweeping mode at the V_G ranges from 0 to 5 V for 100 cycles of transfer curve. (b) $V_{th,FET}$ of the MOSFET measured by each forward and reverse sweeping mode over time.

In the meantime, the influence on impedance (resistance and capacitance in our case) of RGs has to be considered as one of variables in $f(RG)$ in equation (1.8) because the connection of the RG module to the gate of the MOSFET results in addition of impedance of RGs in series over the RGFET system. When the impedance of the RG module is much larger than that of the MOSFET, properties of the RG module govern the RGFET system, which is not a favorable case for us.

Figure 1.10 shows an equivalent circuit model of the RGFET system listing major impedance components. There are capacitors connected in series over the RGFET system. C_{EDL}, C_{RG}, and $C_{G,FET}$ are capacitance of electrical double-layer between solution and RG surface, RG material, and MOSFET, respectively.

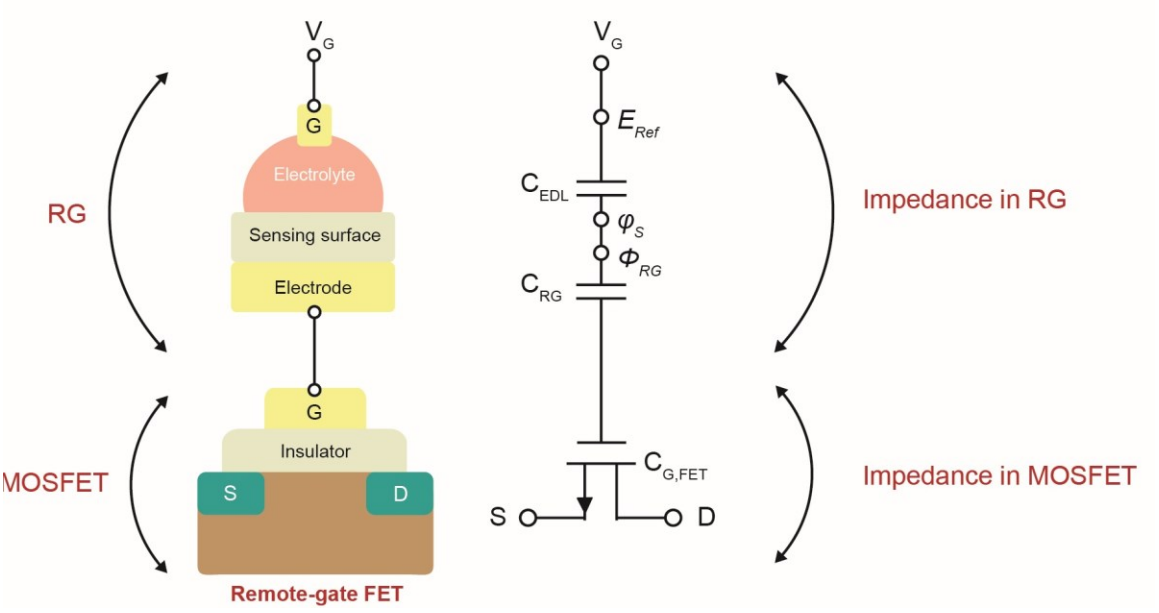

Figure 1.10. Schematic image of the RGFET system and equivalent circuit model of the RGFET system. C_{DL}, C_{RG}, and $C_{G,FET}$ are capacitance of the electrical double-layer between solution and RG surface, RG material, and silicon FET, respectively. Resistors are assumed to be in parallel with the capacitors.

We assume that combining all capacitors and electrical potentials in series shown in Figure 1.10 would determine $V_{th,RG}$ of the RGFET system. When we apply gate voltage into the RGFET, the actual voltage would be divided into three separated systems: the MOSFET (V_{MOSFET}), solution system (V_{chem}), and RG module (V_{RG}). By Ohm's law, we can describe:

$$V_{RGFET} = V_{MOSFET} + V_{chem} + V_{RG}$$

In other words, the current over the RGFET is the same, we can express the relation above in terms of resistance of each part as shown below:

$$R_{RGFET} = R_{MOSFET} + R_{chem} + R_{RG} \qquad (1.9)$$

The voltage drops across each part will be directly proportional to the size of the resistor of each part. Hence, measurement of resistance of each part will be required.

Meanwhile, total capacitance of the RGFET (C_{RGFET}) is described as the sum of capacitance from major three components originating from each system of solution interface (C_{EDL}), substrate of RG (C_{RG}), and the gate insulator of FET ($C_{G,FET}$):

$$\frac{1}{C_{RGFET}} = \frac{1}{C_{EDL}} + \frac{1}{C_{RG}} + \frac{1}{C_{G,FET}} \qquad (1.10)$$

In our case, $C_{G,FET}$ is invariable from the intrinsic silicon FET. We hypothesize that the influence of C_{EDL} would be insignificant on the C_{RGFET} because of extremely thin thickness of electrical double layers on the order of angstroms. All RG modules used for this thesis have a large area of solution contact at least with a diameter of 0.5 cm. Presumably, the effect of C_{RG} that is a capacitance much larger than that of C_{RGFET} would be trivial as was the case for C_{EDL}.

In order to verify the hypothesis above, two different RGs of SiO_2 and polystyrene (PS)/SiO_2 were prepared (Figure 1.11a). SiO_2 substrate has a 300 nm thickness. PS layer deposited on the same SiO_2 substrate has about 100 nm thickness. Resistance and capacitance of each RG is measured by the following description.

The same volume of pH7 solution (50 μL) is added on each SiO_2 and PS/SiO_2. For the volume of 50 μL, a large diameter of solution of over 0.5 cm is achieved on RG surfaces. AC frequency is applied between the Ag/AgCl reference electrode and the Si electrode at the bottom of each RG. The level of voltages is set at 1 V during the measurement of capacitance and resistance. At the same measurement condition, the impedance of commercial MOSFET is measured by using two terminals from the drain to the gate.

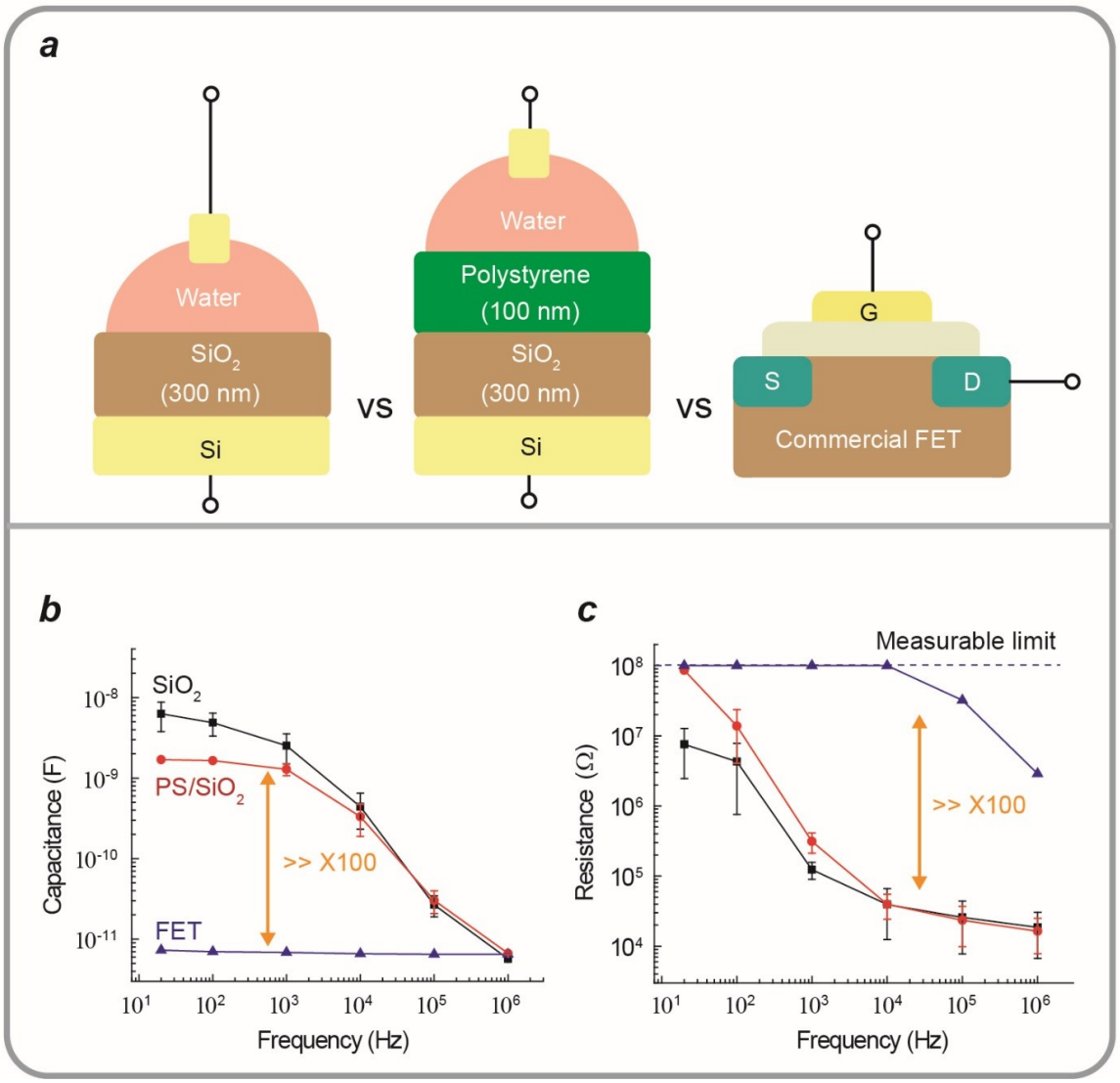

Figure 1.11. (a) Schematic image of impedance measurement setups of RGs and MOSFET. Frequency vs (b) capacitance and (c) resistance from RGs of SiO_2 and PS/SiO_2 and Si-FET. At least 3 samples of each RG were measured.

Capacitance and resistance from both RGs are compared with that of the MOSFET as shown in Figure 1.11b and 1.11c, respectively. PS/SiO_2 RG has a lower capacitance than that of SiO_2 due to the deposition of thick PS layer on SiO_2. Also, the PS has even lower

dielectric constant (2.56) than that of SiO_2 (3.9). Nonetheless, the capacitance of the MOSFET is at least 100 times smaller than any RG surfaces (Figure 1.11b). The total capacitive system over the RGFET is mostly determined by that of the MOSFET.

The resistance of the MOSFET is also much larger than those of RGs (Figure 1.11c). The gate voltage applied over the RGFET system is mostly dropped to the MOSFET. These results indicate that effects of the impedance of RGs are highly insignificant on the total impedance of the RGFET. Therefore, each equation (1.9) and (1.10) becomes:

$$\mathrm{R_{RGFET}} \approx \mathrm{R_{MOSFET}}$$

$$\mathrm{C_{total}} \approx \mathrm{C_{G,FET}}$$

This indicates that the impedance of the RG module is not a critical factor that is able to change $\mathrm{V_{th,RG}}$ in our RGFET.

Figure 1.12 shows a simplified equivalent circuit model from Figure 1.9 by removing negligible parameters. We know that V_{chem} term in equation (1.8) already includes E_{Ref} and φ_s as shown in Chapter 1.1.2. The ϕ_{RG} term that was not included in any equation yet would be associated with $f(RG)$ term. Now, we finally have an expression of $\mathrm{V_{th,RG}}$:

$$\mathrm{V_{th,RG}} = \mathrm{V_{th,FET}} + E_{ref} + \phi_{lj} - \varphi_s + \chi_{sol} + \frac{\Phi_{RG}}{q} \qquad (1.11)$$

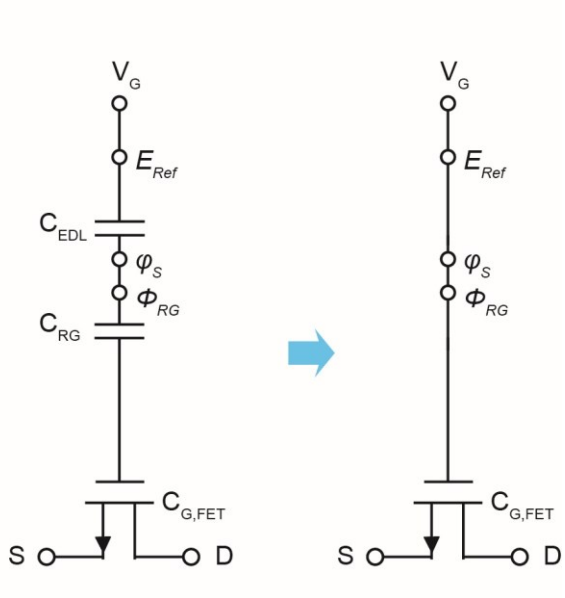

Figure 1.12. Simplified equivalent circuit model of the RGFET system from Figure 1.9.

It is noted that there is no current flow (~ pA) through the gate of the RGFET due to significantly large gate input impedance as shown in Figure 1.13.

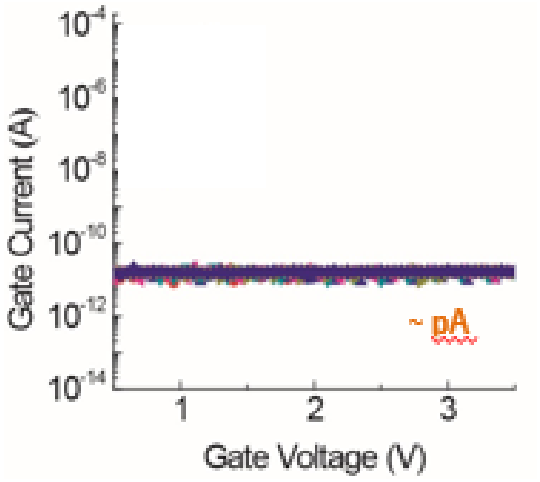

Figure 1.13. Gate leakage current levels during operations of the RGFET.

Thus, no possible change in electrochemical potentials exists in terms of redox reactions of RG surfaces assisted by the gate currents, which also supports equation (1.11). As a result, the shift in $V_{th,RG}$ in our RGFET setup would be related to $\Delta\varphi_s$ or $\Delta\Phi_{RG}$:

$$\Delta V_{th,RG} = \Delta\varphi_s \; or \; \Delta\Phi_{RG} \qquad (1.12)$$

1.2.2. Applications of RGFET detection system

FETs, beyond their conventional roles of switching building blocks in integrated circuits, have evolved as electrochemical sensors and biosensors as described above. The application of the RGFET is not limited to biosensors, the most used application. I believe that the RGFET is comparable to a new type of "scale" in the microscopic world, capable of characterizing any chemical reaction with a difference in potential energy, work function, and surface potentials as shown in Figure 1.14. In this dissertation, I demonstrate new applications of the RGFET as an analytical platform to characterize interface properties of organic polymer materials. This RGFET characterization provides new information, perspective, and insight into the chemical reactions occurring at the surface of organic materials. Better understanding of the fundamental mechanisms in organic electronics will lead to better designed materials that could overcome current limitations of organic electronics performance.

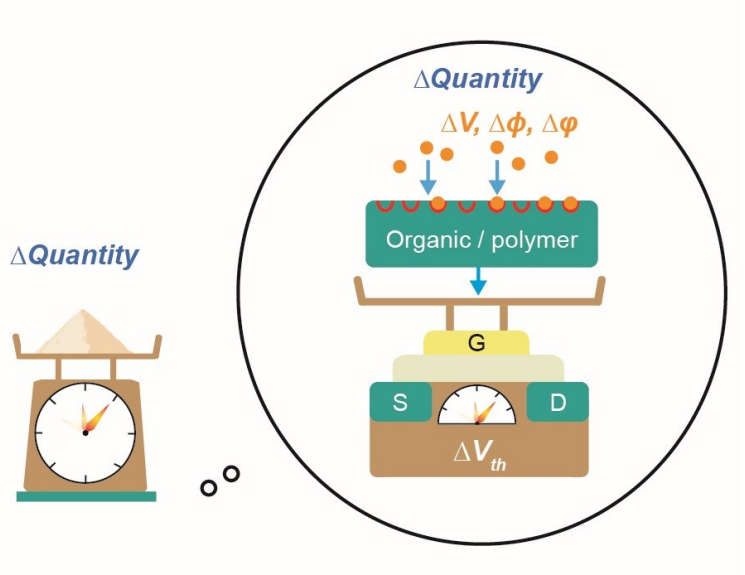

Figure 1.14. The RGFET used for characterization of electrochemical reactions at organic polymer materials.

The aim of this thesis is to investigate fundamental mechanisms of diverse electrochemical interactions occurring at the interface of organic/polymer materials in terms of the RGFET.

In Chapter 2, molecular doping effects in a conjugated polymer and diffusion of small chemical molecules are characterized by the RGFET system.[11] Hole concentrations and mobility of doped polymers are also quantified using the RGFET characterization.

In Chapter 3, the dependence between orientational ordering of dipoles on the polymer interface and typical electrical drift occurring at electrochemical FET sensors was elucidated. As a result, it was discovered that conjugated polymers truly enhance the electrochemical stability of their charged groups.

In Chapter 4, a novel method was devised and tested to overcome Debye length issues of FET biosensors based on newly proposed polymer sensing membranes incorporating antibodies in the polymer[12].

1.3. References

(1) KAHNG, D. *US Patent* **1963**, *US3102230A*.

(2) Deleonibus, S. *Electronic Device Architectures for the Nano-Cmos Era: From Ulitmate Cmos Scaling to Beyond Cmos Devices* **2009**, Ix.

(3) Fjeldly, T. A.; Shur, M. *Ieee T Electron Dev* **1993**, *40*, 137.

(4) Hashemi, P.; Behnam, A.; Fathi, E.; Afzali-Kusha, A.; El Nokali, M. *Solid State Electron* **2005**, *49*, 1341.

(5) Bergveld, P. *IEEE transactions on bio-medical engineering* **1970**, *17*, 70.

(6) Bergveld, P. *Sensor Actuat B-Chem* **2003**, *88*, 1.

(7) Barabash, P. R.; Cobbold, R. S. C.; Wlodarski, W. B. *Ieee T Electron Dev* **1987**, *34*, 1271.

(8) Jang, H. J.; Cho, W. J. *Appl Phys Lett* **2012**, *100*.

(9) Vanderspiegel, J.; Lauks, I.; Chan, P.; Babic, D. *Sensor Actuator* **1983**, *4*, 291.

(10) Guliga, H.; Abdullah, W. F. H.; Herman, S. H. *2014 2nd International Conference on Electrical, Electronics and System Engineering (Iceese)* **2014**, 11.

(11) Jang, H. J.; Wagner, J.; Li, H.; Zhang, Q. Y.; Mukhopadhyaya, T.; Katz, H. E. *J Am Chem Soc* **2019**, *141*, 4861.

(12) Jang, H. J.; Lee, T.; Song, J.; Russell, L.; Li, H.; Dailey, J.; Searson, P. C.; Katz, H. E. *Acs Applied Materials & Interfaces* **2018**, *10*, 16233.

Chapter 2

Characterization of molecular doping and diffusion by RGFET

2.1. Introduction

Conjugated polymers are recognized as a class of organic materials incorporating delocalized electrons in their backbones.[13] Conductivity of conjugated polymers can be effectively tuned over several orders of magnitude depending on the amount of dopant in conjugated polymers. For instance, a p-type dopant that has high electron affinity takes electrons from the backbone of a conjugated polymer, leaving behind mobile hole carriers in the host semiconductor.

The first demonstration of dopant-induced conductivity of a conjugated polymer was shown in polyacetylene upon treatment with iodine vapor.[14] The initial reports of electrical conductivity on the order of 1000 S/cm[15] is the promising value that has been mostly observed in inorganic materials. Despite early optimism, such high conductivity has been only maintained for a short period, resulting from a high volatilization of iodine dopant because of its small size.[16-18] The dopant counter-ions are not covalently bonded to the organic semiconductors so they are free to diffuse out of films or into other layers under an application of electric fields. This has provoked critical issues in the device stability which is a reason why the popular dopant, iodine, has been mostly abandoned. In recent years, intense study has been performed to increase electrical stability of doped polymers although there is a loss of conductivity. Stable doping of regioregular poly-3-hexylthiophene (P3HT) has been observed by using a relatively large molecular dopant like F4TCNQ.[19]

In theory, F4TCNQ has a deep LUMO level (-5.2 eV) which is energetically in the vicinity of the HOMO level of many organic semiconductors. Doping is facilitated by charge transfers from the HOMO level of the host to the LUMO level of the dopant molecule. The doping mechanism is relatively straightforward but various unexplored parameters exist because of limitations in observing the doping process via current analysis tools.

The most common doping method involves a solution blending of polymers and dopant before deposition as shown in Figure 2.1a. However, solution blending often drastically reduces the solubility of the polymer, leading to difficulties in processing doped films. Also, this effect resulted in decreases in mobility caused by the structural disruption resulting from dopant incorporation.[20] Some of the highest recent polymer conductivities have been obtained by a sequential solution doping method[21-23] shown in Figure 2.1b.

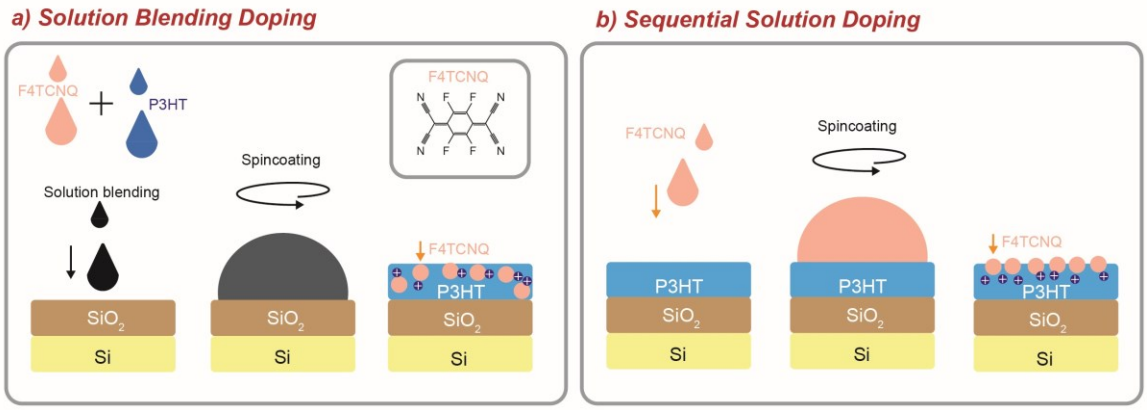

Figure 2.1. Schematic images of doping methods based on (a) solution blending and (b) sequential solution.

Sequential doping methods overcame issues of poor solubility of solute mixtures, produced more uniform morphology and are compatible with roll-to-roll solution processing. Therefore, it is of particular interest to characterize the solution-doping process to best evaluate the usefulness of this process.

In classic semiconductor physics, conductivity of a thin film can be described by a simple relation, $\sigma = e\mu_h p$ where e, μ_h, and p are electron charge, hole mobility, and hole carrier concentration, respectively. However, it has been challenging to extract even basic electrical parameters listed above because of the complexity and diversity of organics affecting multiple variables.[24-26] For example, μ_h of organic films varies depending on morphology and microstructures further influenced by doping concentrations and fabrication methods. Specialized ways to calculate carrier concentrations such as capacitance-voltage[27] and photoelectron spectroscopy measurements[28] were established but they require specially designed sample fabrication or complicated experimental setups.

The first part of chapter 2 demonstrates a new platform technology to characterize hole carrier concentrations and mobility of a conductive polymer film doped sequentially in terms of using RGFET system. The RGFET system measures perturbations of the electrical potential of the polymer film on the RG. Figure 2.2 shows schematic images of the RGFET system to analyze molecular doping effects. P3HT film made on SiO_2/Si substrate is electrically coupled to the gate of a commercial silicon FET first. That is, the P3HT/SiO_2/Si substrate is loaded as an RG module while the Si is used as an electrode of the RG module.

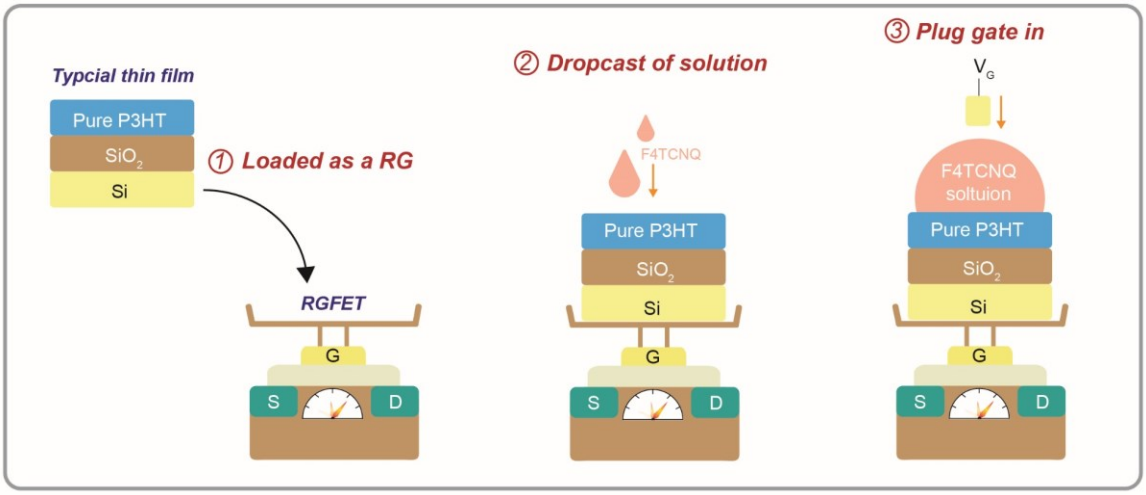

Figure 2.2. Schematic images of the RGFET system to characterize molecular doping effect between P3HT film and F4TCNQ.

Different F4TCNQ concentrations are dissolved in solvent acetonitrile (ACN) that is orthogonal to P3HT. Each prepared F4TCNQ solution is applied to the pure P3HT surface on the RG module for doping. An Ag/AgCl reference electrode is immersed in the F4TCNQ solution to apply the gate voltage of the whole RGFET system. Finally, we measure changes in $V_{th,RG}$ from the solution doping on the RG module. Interestingly, the charge transfer between F4TCNQ and P3HT film on the RG module is expressed as a reduction of $V_{th,RG}$.

Using this observation, a new formula is established to calculate the induced hole carrier concentrations in the doped P3HT in terms of variations of $V_{th,RG}$. Also, the responsiveness of the other dopants such as 7,7,8,8-tetracyanoquinodimethane (TCNQ) and tetracyanoethylene (TCNE) related to their reduction potentials is observed using the RGFET system on P3HT film.

Meanwhile, the diffusion of small molecules between organic layers provokes other serious issues in stability and lifetimes of organic electronics. The counterions formed from dopant molecules are free to drift under an electric field, either within films or into adjacent films, because they are not covalently bonded to the organic semiconductor.[29] The diffusion of a relatively large p-dopant, F4TCNQ, over a layer consisting of either conjugated small molecules or polymer such as P3HT was investigated in recent work.[30-32] Despite these influences on electronic performance, they are rarely discussed because of limitations of current analysis tools. To be specific, monitoring diffusion using UV−vis−NIR[30] and photoluminescence (PL) spectroscopy[33] requires an observable interaction between host materials and diffused molecules. It is even more challenging to measure simple physical diffusions of molecules through passive polymer dielectrics driven by concentration gradients and electric fields.

Herein, we also develop a way to characterize diffusion of small molecule such as F4TCNQ in passive polymers such as PS by using the RGFET setup. I discovered that F4TCNQ also reacts with the inorganic electron donor surfaces of gold (Au) and indium tin oxide (ITO) by making surface dipoles which results in the same $V_{th,RG}$ shift trend. Interestingly, I observed a similar range in electrical potentials of P3HT, Au, and ITO regulated only by concentrations of F4TCNQ while F4TCNQ fully occupied the electroactive sites on those donor surfaces. I also confirmed the responsiveness of the other dopants such as TCNQ and TCNE related to their reduction potentials with both ITO and P3HT RG. Meanwhile, signaling of F4TCNQ by ITO offers a new approach to monitor diffusion of small molecules through the passive, non-interaction polymer PS as shown in Figure 2.3. F4TCNQ and ITO are used as a tracer and a sensing layer of the tracer,

respectively. Thus, the dynamic doping of a conjugate polymer and transport of a dopant through an insulating polymer could both be observed and be quantified on the RGFET.

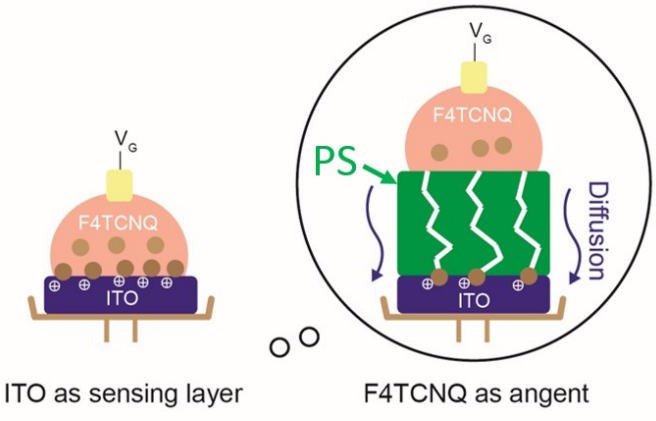

Figure 2.3. Schematic image of the RGFET system for characterization of diffusion.

2.2. Experimental section

2.2.1. Sample preparations (molecular doping)

SiO_2/Si substrates, with a 70 nm and 300 nm thickness of oxide, are prepared via standard RCA cleaning process. A concentration of 10 mg/ml of P3HT (Solaris, SOL4106) was prepared by dissolving polymer in chlorobenzene, sonicating for 1 hour, and then heating at 60 °C overnight, respectively. The solution is then filtered using a hydrophobic PTFE syringe filter and is spin-coated on cleaned SiO_2/Si substrate under 1800 RPM for 1 min, respectively. Post annealing of P3HT is done using heat plate under 60 °C for 1 h. The surface images of the P3HT film are acquired by using the Optical Profilometer/3D laser scanning microscope (VK-X100). The P3HT had a thickness of 46.5 nm measured

using the Thin Film Analyzer (F20-NIR). A 1 mg/mL solution of F4TCNQ (Ossila, 29261-33-4), TCNQ (Alfa Aesar, 1518-16-7), and TCNE (Sigma Aldrich, 670-54-2) is prepared by dissolving the dopant in ACN aided by ultrasonication for 30 minutes, filtered using a hydrophobic PTFE syringe filter membrane. A series dilution of the prepared dopant solution is conducted in order to create the range of solution concentrations from 1 mg/ml to 100 ng/ml.

2.2.2. Sample preparations (diffusion monitoring)

PS (Sigma Aldrich, 430102) solutions were prepared at concentrations of both 10 mg/ml and 35 mg/ml PS and were dissolved in toluene under ultrasonication. In order to synthesize polystyrene-co-4- vinylbenzocyclobutane (XLPS), a solution of styrene, 4-vinylbenzocyclobutane (10% in weight ratio), and 2,2′- azobis(isobutyronitrile) (AIBN, 2% in weight ratio) in chlorobenzene (2 mL for 10 mmol total monomers) in a high-pressure vessel was bubbled with nitrogen for 10 min and then sealed rapidly under a nitrogen atmosphere. The mixture was stirred vigorously at 65 °C for 18 h in the dark. After cooling to room temperature, the resulting viscous solution was precipitated into methanol (150 mL) and stirred for 1 h. The precipitated polymer was dissolved in tetrahydrofuran (THF) and then reprecipitated into methanol. The purification procedure was repeated twice, and the precipitate was dried under vacuum (at 60 °C in the vacuum oven) to yield XLPS in 90% yield. The concentrated solutions were then filtered using a hydrophobic PTFE syringe filter. The solutions were then spin-coated to SiO_2/Si under 1800 RPM for 1 min, respectively. Post annealing of PS was done using heat plate under 100 °C for 1 h. XLPS was baked in vacuum oven for cross-linking under 180 °C for 2 h.

2.2.3 Characterization by UV-Vis-NIR spectroscopy and XPS

Doping is performed by wetting the surface of pure P3HT film on ITO with each F4TCNQ solutions in different concentrations, waiting 5 seconds, then spinning off the excess solution at 1800 rpm. Absorption peak intensity is measured with a LAMBDA 950 UV/Vis Spectrophotometer with incremental increase of wavelength by 1 nm. All spectra are normalized to 1 at the maximum of the P3HT absorption at 540 nm. The X-ray Photoelectron Spectroscopy (XPS) spectra are analyzed using a PHI 5600 XPS (58.7 eV pass energy, 0.250 eV/step, Mg Kα X-rays) and processed with CasaXPS software (Teignmouth, UK).

2.2.4 Measurement of conductivity and capacitance

Sheet resistance of each doped P3HT film on SiO_2/Si processed identically above is measured by four-point probes measurements. To make contact on the four-point probe, Au was deposited on doped P3HT film with a shadow mask (width: 2 mm and length: 250 μm between two Au electrodes). Metal-insulator-semiconductor structure is achieved from P3HT/SiO_2 in order to measure capacitance values of pure and doped P3HT. The area of doped P3HT for the capacitor is defined by O_2 plasma etching using Au gate mask with 4 types of length: 0.95, 1.1, 1.25, and 1.4 mm and the same width of 2 mm.

2.2.5 Basic electrical performance of Si-FET transducer

Figure 2.4 shows representative transfer curve (a) and output characteristic (b) of the commercial FET, CD4007UB. A CD4007UB chip is comprised of three n-channel and three p-channel enhancement-type MOSFETs.

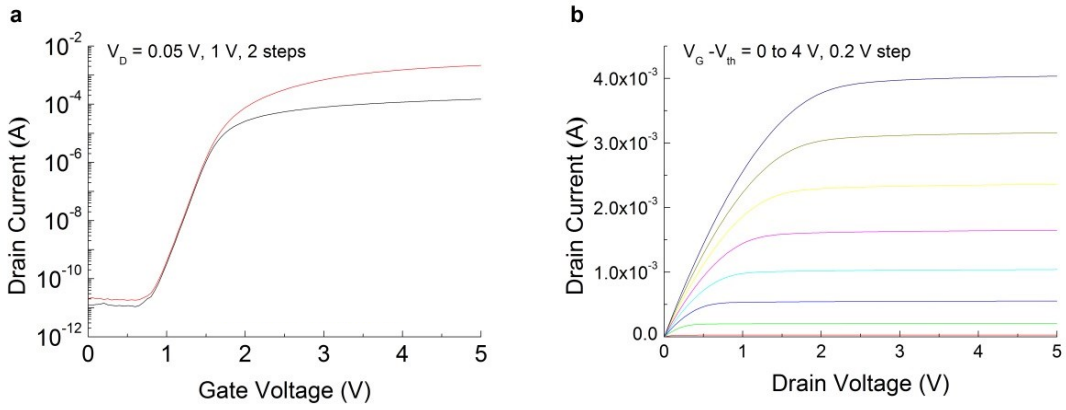

Figure 2.4. Representative (a) transfer curve and (b) output characteristic of commercial FET, CD4007UB.

The transistor elements are accessible through the package terminals to provide a convenient means for constructing the various typical circuits. We used the same n-type FET over all experiments in order to remove any possible variable coming from a transducer part. Subthreshold swing of 136 mV/dec and V_{th} of 1.5 V are observed in the n-type FET. High on/off ratio up to 10^8 is obtained (Figure 2.4a).

2.2.6 Basic electrical properties of P3HT OFET

Before investigations of molecular doping effects between P3HT and F4TCNQ, the semiconducting activity of P3HT is confirmed by making an organic FET (OFET). Figure 2.5a shows the transfer curve of a P3HT OFET measured by double sweeping mode. A 300-nm-thick SiO_2 dielectric is used as the gate dielectric of P3HT OFET. Width and length of OFET are 2 mm and 0.25 mm, respectively. Transfer curves are repeated 10 times under V_g sweeping ranging from -100 V to 25 V while the drain voltage is set as -100 V.

V_{th} of P3HT OFET calculated from Figure 2.5b is 11 V. μ_h at saturation regime is calculated as 0.008 cm^2/Vs at V_g of -40 V by using the following equation below:

$$I_D = \frac{W}{2L}\mu_{sat}C_i(V_g - V_{th})^2$$

where I_D is drain current and C_i is capacitance per area of gate dielectric. It is noted that a typical value of μ_h for spin-coated undoped P3HT is 0.01 cm^2/Vs in the literature[34].

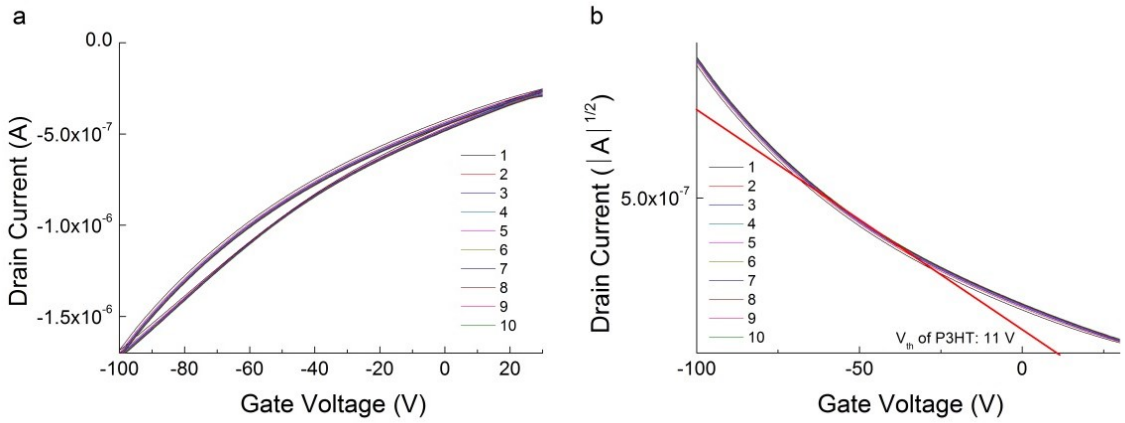

Figure 2.5. (a) Representative transfer curve of P3HT OFET measured by the double sweeping mode. (b) $\sqrt{|I_D|}$ vs gate voltage plot.

2.2.7 Construction of RGFET detection system

The RGFET detection system is divided into two parts: a commercial Si-FET (CD4007UB) and an RG module. Si is used as electrode for P3HT/SiO_2/Si substrate on an RG module and is electrically coupled to the gate of Si-FET. 25 µl of each varying

concentration of dopant dissolved in ACN is placed on the P3HT surface of the RG module. An Ag/AgCl reference electrode is placed in the solution in order to apply the gate bias for all measurements. Any potential variation on the RG modules is transferred to the gate of the FET by shifting $V_{th,RG}$. All transfer curves are measured by using a Keithley semiconductor analyzer with a drain voltage set at 50 mV. Each $V_{th,RG}$ is extracted from the gate voltage which corresponds to a drain current of 1 μA. After the stabilization process, varying concentration solutions of F4TCNQ, from low to high concentrations, are placed on the surface of each RG module and $V_{th,RG}$ shifts are monitored. After injecting 1 mg/ml of F4TCNQ solution, remote modules were then repeatedly washed 3 times with pure ACN and then the RG is remeasured under a new pure ACN.

2.3 Results and Discussion

2.3.1 Conventional spectroscopic observations

UV-Vis-NIR spectroscopy is the most typical way to analyze the doped films. There is a charge transfer reaction involving an appropriate donor (P3HT) and acceptor (F4TCNQ) that produces polaronic species creating many sub-gap absorptions.[35] Figure 2.6 presents the UV-Vis-NIR spectra of P3HT films doped sequentially with varying F4TCNQ concentrations that range from 100 ng/ml to 1 mg/ml.

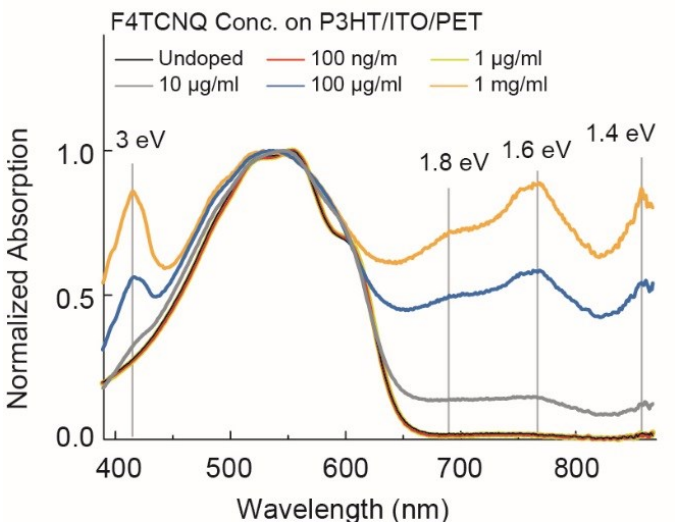

Figure 2.6. UV-Vis-NIR spectra of P3HT films doped by F4TCNQ dissolved in ACN ranging from 100 ng/ml to 1 mg/ml.

The spectra of the lightly doped P3HT films (≤1 µg/ml) are comparable to that of undoped P3HT film. Higher F4TCNQ concentrations (≤10 µg/ml) on P3HT begin to produce distinguishable changes in optical absorbance. A pronounced sub-band gap absorption occurs at 3.0, 1.8, 1.6, and 1.4 eV from heavily-doped P3HT films (≤100 µg/ml). In particular, the prominent 1.4 and 1.6 eV peaks describe singly negatively charged F4TCNQ as F4TCNQ undergoes integer charge transfers with P3HT sites[36].

XPS study of the doped P3HT film processed identically to Figure 2.6 is performed in Figure 2.7. For the surface of undoped P3HT, only the S 2p peak is observed which originates from the thiophene backbone in P3HT. In case of the doped P3HT surfaces, higher intensity signals of both F 1s and N 1s which originates from F4TCNQ are shown with a less intense peak of 2s. In particular, the P3HT surface doped by 1 mg/ml F4TCNQ

solution presents an insignificant peak of S 2p, indicating that F4TCNQ radical anions fully cover the surface of P3HT by taking a form of the additional layer of F4TCNQ as increasing concentration of F4TCNQ.

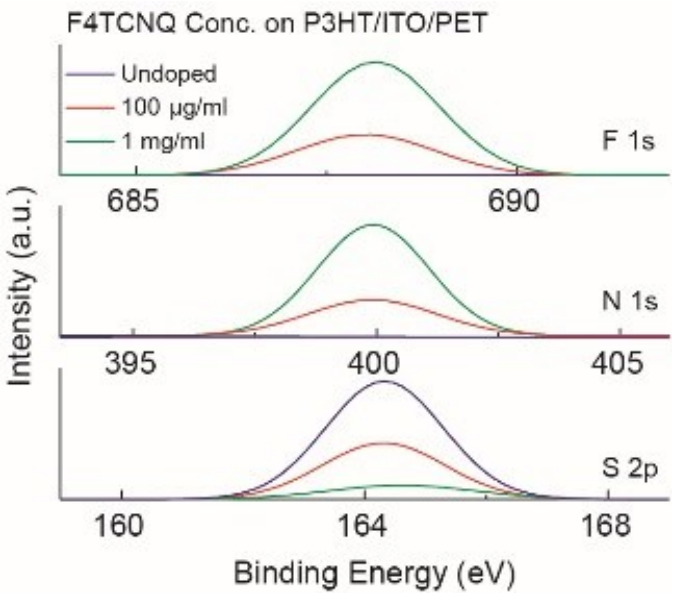

Figure 2.7. XPS spectra of doped P3HT films processed identically to Figure 2.6.

Figure 2.8 shows the microscopic images of the doped P3HT films made identically to Figure 2.6. No observable changes are shown until the addition of F4TCNQ solution concentration of 10 μg/ml onto the P3HT surface. Heavily-doped P3HT films (≥100 μg/ml) start to show phase-segregated F4TCNQ domains on the P3HT surface, which corresponds to the XPS observation in Figure 2.7. This F4TCNQ aggregate layer on the P3HT surface is caused by the solubility limit of F4TCNQ in P3HT (4.9 mol%) as reported.

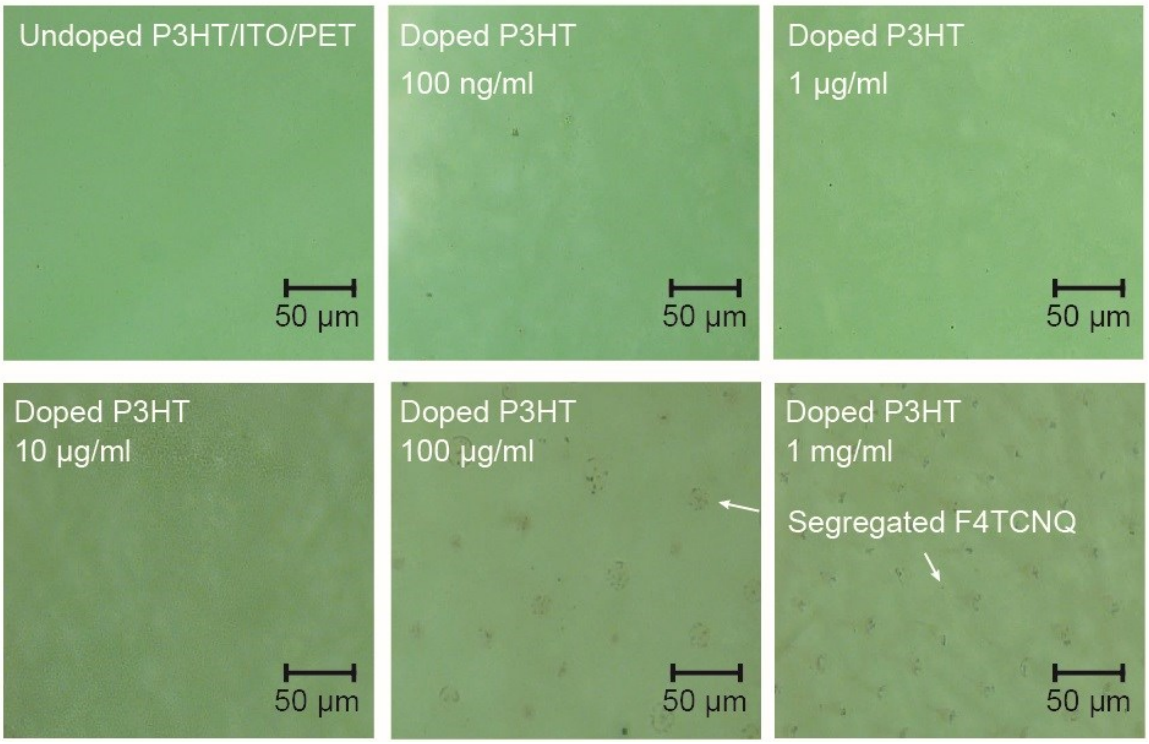

Figure 2.8. Microscopic images of doped P3HT films processed identically to Figure 2.6.

This overlaying F4TCNQ layer or aggregation of F4TCNQ on the P3HT surface is also confirmed by XPS depth profiling of P3HT surface exposed to 1 mg/ml F4TCNQ as shown in Figure 2.9. The peak of S 2p (indicating P3HT) is higher at the shallow surface where the surface is sputtered for 20 min as shown in Figure 2.9a. After continuing sputtering this film, the S 2p peak steadily reduces and eventually disappears because of completely removed P3HT from the substrate by sputtering. Likewise, the initial doped P3HT displays higher concentrations of F4TCNQ on the surface shown as higher peak of F 1s at the initial state (Figure 2.9b). That is, F4TCNQ counter-ions fully cover the P3HT surface. After sputtering surface, intensity of F 1s is largely reduced. Similar decreased amounts of dopants are observed from the shallow surface towards the SiO_2 surface (Figure

2.9b). Remaining F4TCNQ even after 60 min sputtering is totally removed by further sputtering (75 min) as shown in Figure 2.10.

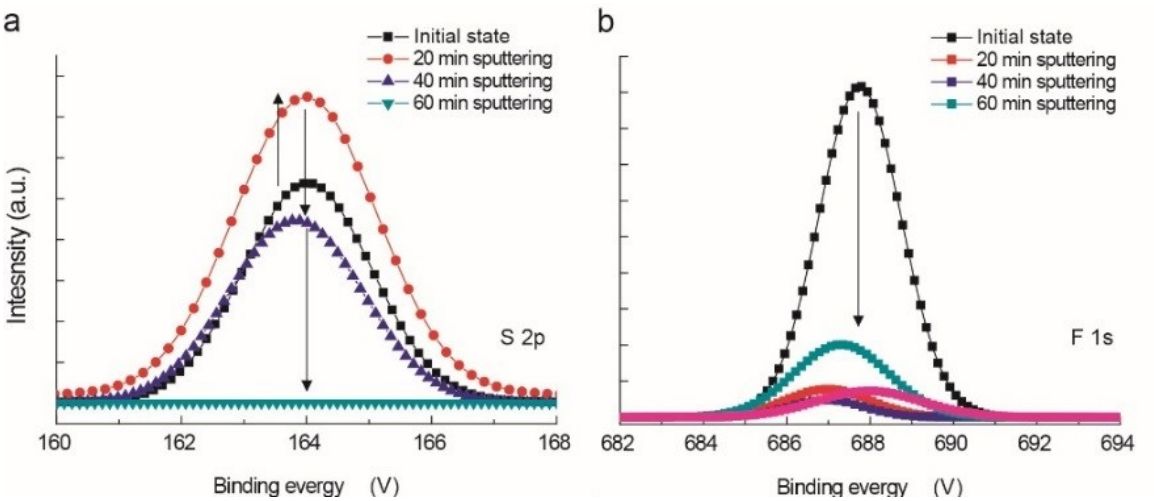

Figure 2.9. XPS depth profiling of P3HT/SiO_2 exposed to 1 mg/ml F4TCNQ. XPS spectra of the doped P3HT film depending on sputtering times: (a) sulfur, (b) fluorine.

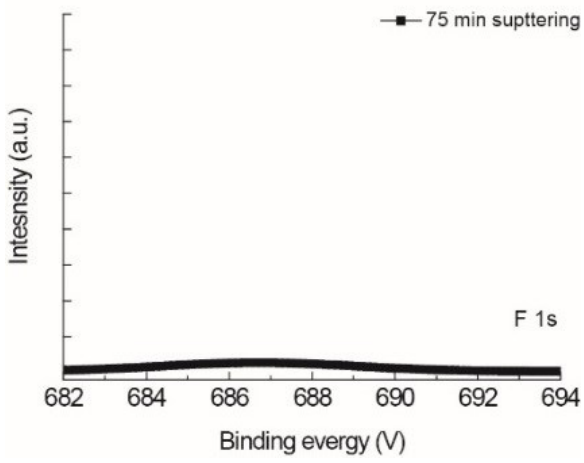

Figure 2.10. Fluorine peak from the P3HT/SiO_2 exposed to 1 mg/ml F4TCNQ after 75 min sputtering.

2.3.2 Molecular doping characterized by RGFET

Herein, the molecular doping effects of P3HT films characterized by the conventional spectroscopies are newly analyzed by using the RGFET described in Figure 2.2. The doping effect of F4TCNQ on a P3HT RG is expressed as horizontal shifts in transfer curves of the RGFET as shown in Figure 2.11. Particularly, F4TCNQ imposes positive charges on the P3HT RG relative to the solution potentials, indicating increased hole concentrations of P3HT film due to doping effects.

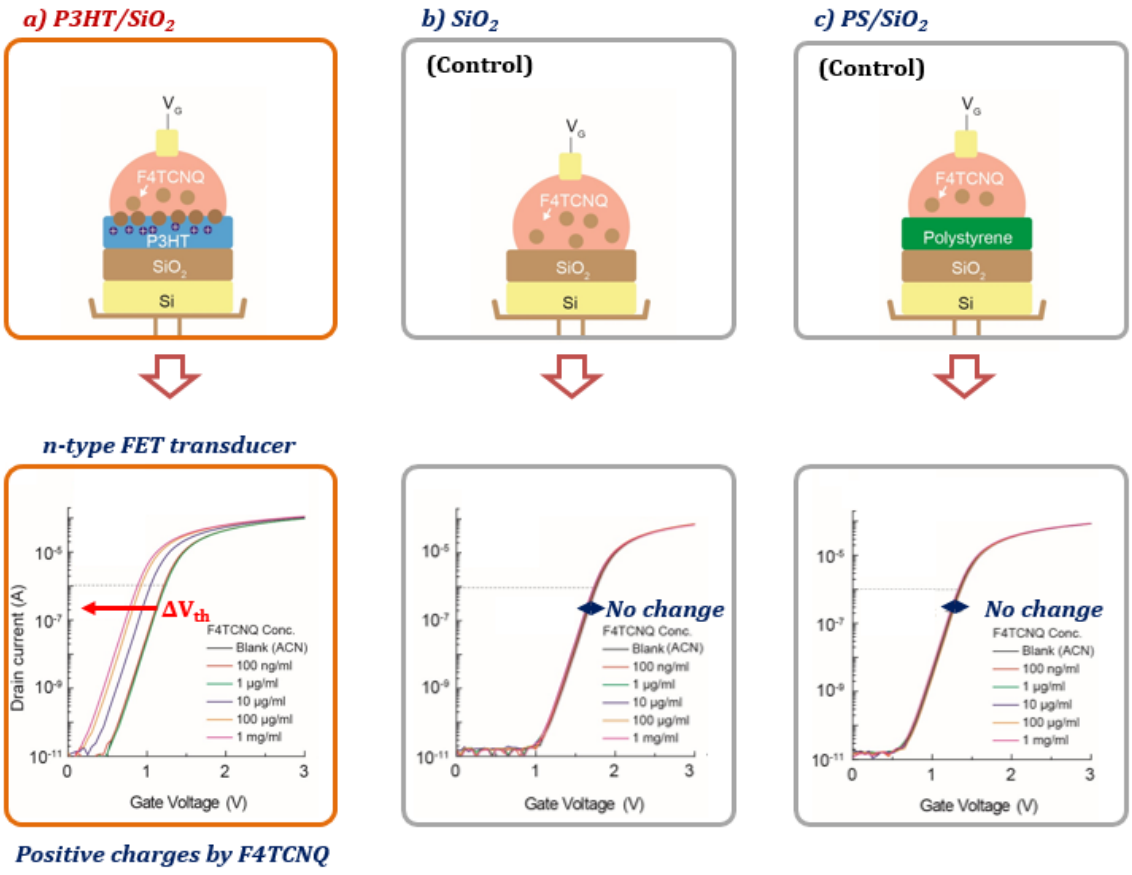

Figure 2.11. Response of representative transfer curves of RGFET for F4TCNQ solution concentrations from RGs of (a) P3HT/SiO_2, (b) SiO_2, and (c) PS/SiO_2.

On the other hand, no responses are shown from two different control RGs upon exposure to F4TCNQ which consist of pure SiO_2 (Figure 2.11b) and PS/SiO_2 (Figure 2.11c) because of the lack of interaction between F4TCNQ molecule and materials in control RGs.

Figure 2.12 presents $V_{th,RG}$ variations of P3HT/SiO_2, SiO_2, and PS/SiO_2 with increasing F4TCNQ concentrations over time. Each step includes 5 consecutive measurements taken at incremental times under a specific dopant concentration, demonstrated in Figure 2.12. The first three steps are measured under pure ACN without injections of any dopant in RG surfaces for stabilization of the measurement system.

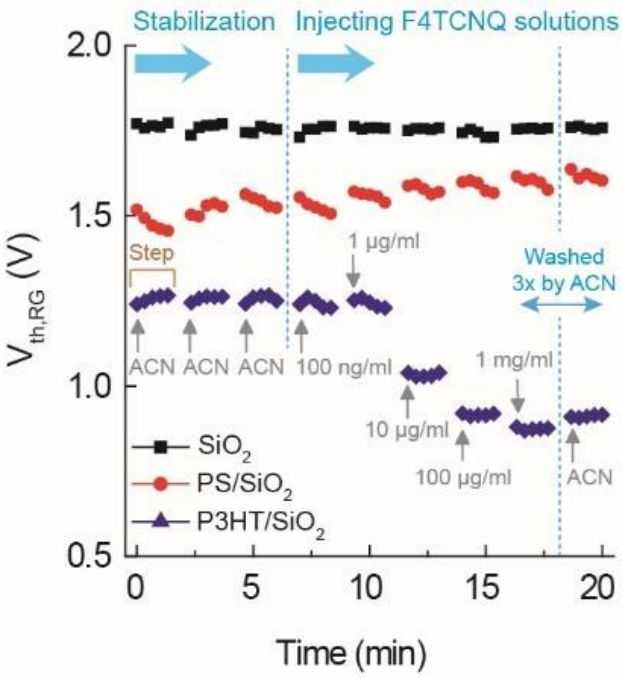

Figure 2.12. Representative $V_{th,RG}$ response from RGs of P3HT/SiO_2, SiO_2, and PS/SiO_2 on the time scale for F4TCNQ solution concentrations.

Therefore, initial $V_{th,RG}$ (V_{th0}) obtained during the stabilization process reflects intrinsic properties of RG material surfaces. When the P3HT RG surface is exposed to F4TCNQ solutions higher than 1 μg/ml, a sharp shift in $V_{th,RG}$ occurs, indicating the doping process is completed rapidly. V_{th0} levels from both control RGs (SiO_2, PS/SiO_2) are maintained with increasing F4TCNQ concentrations. Following all the dopant injections up to 1 mg/ml F4TCNQ concentration, the doped P3HT surface is aggressively washed 3 consecutive times with the pure ACN. The washed RG surface is measured again under the pure ACN. Even after aggressive washing of the doped P3HT film surface with pure ACN at the end, the change in $V_{th,RG}$ was insignificant (Figure 2.12). That is, there is no full retrieval of the V_{th0}, implying that only a slight portion of counter-ions were forced off by the physical force of fluid flow and the effect of doping is irreversible.

F4TCNQ counter-ions remaining on the P3HT surface even after washing are also observed by XPS data in Figure 2.13. Peaks of F 1s and N 1s (indicating F4TCNQ) are reduced after washing surfaces as some portion of F4TCNQ counter-ions covering the surface is washed off. Owing to this, the peak of S 2p (indicating P3HT) is increased after washing.

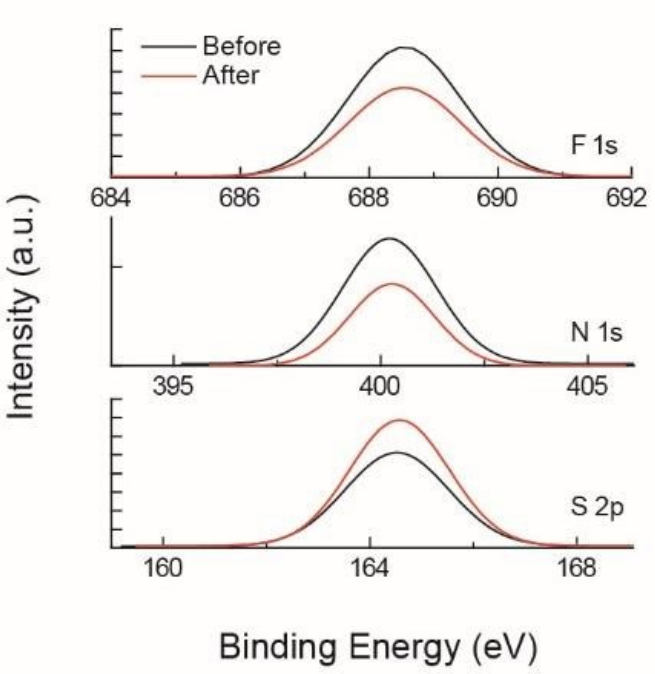

Figure 2.13. XPS spectra of F 1s, N 1s, and S 2p from P3HT/SiO_2 exposed to 1 mg/ml F4TCNQ before/after washing.

Figure 2.14 demonstrates $V_{th,RG}$ distributions in terms of increasing F4TCNQ concentrations over at least 8 samples of each RG. Error bars represent standard error that is the standard deviation of its sampling distribution. The measured $V_{th,RG}$ from respective RG is highly reproducible with a small standard deviation. In case of the P3HT RGs, $V_{th,RG}$ varies by responding to 1 μg/ml solution concentration of F4TCNQ. A saturated trend in $V_{th,RG}$ shifting is shown when the F4TCNQ concentration reaches 1 mg/ml. This saturation obviously reflects a solubility limit of F4TCNQ in P3HT. P3HT reveals non-linear and irreversible shifts in $V_{th,RG}$ depending on F4TCNQ concentrations. The slope is measured to be 113 mV/M ranging from 1 μg/ml to 1 mg/ml of F4TCNQ, beyond the Nernst limit, and $V_{th,RG}$ shifts. This may have indicated directional electrostatic interactions between

F4TCNQ and P3HT at multiple depths of the films. It is noted that the minimum detectable dopant concentration by UV-VIS NIR spectroscopy shown in Figure 2.6 was 10 µg/ml solution concentration.

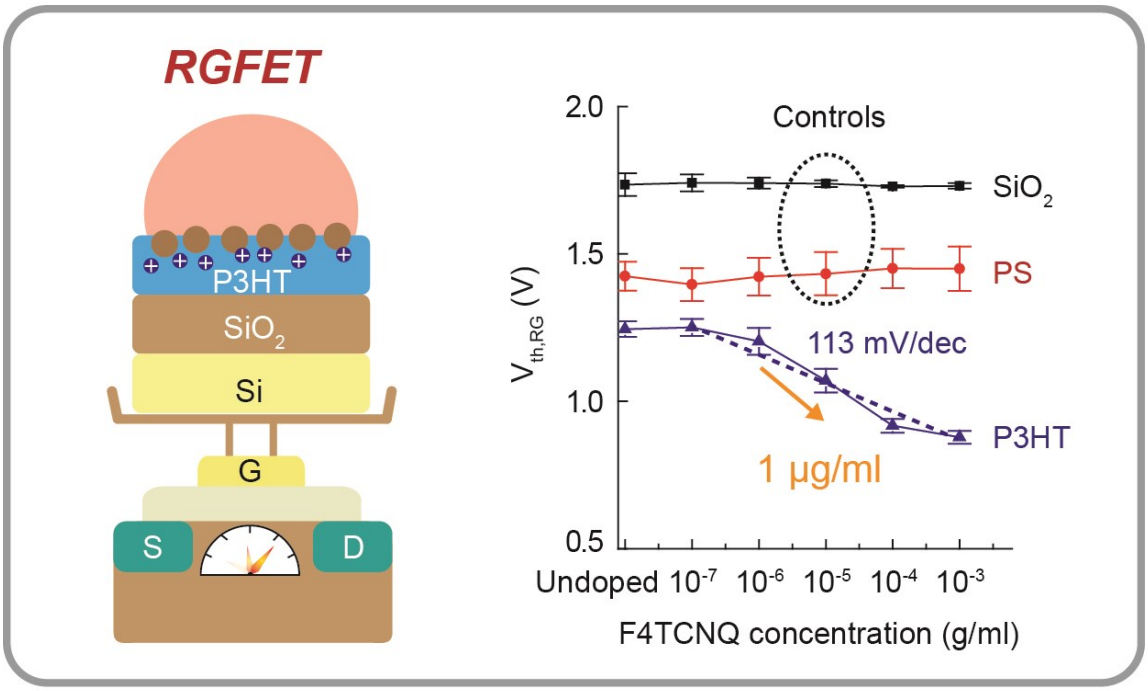

Figure 2.14. $V_{th,RG}$ distributions of each RG in terms of increasing F4TCNQ concentrations over at least 8 samples.

Figure 2.15 shows specificity of $V_{th,RG}$ response only by the P3HT RG to F4TCNQ concentrations. $\Delta V_{th,RG}$ is calculated by subtracting $V_{th,RG}$ values at each F4TCNQ solution concentration from each V_{th0}. $\Delta V_{th,RG}$ at P3HT RG increases almost up to 30% at 1 mg/ml F4TCNQ solution concentration compared to V_{th0} at undoped P3HT RG. The control RGs have almost no $\Delta V_{th,RG}$ for F4TCNQ solution concentrations.

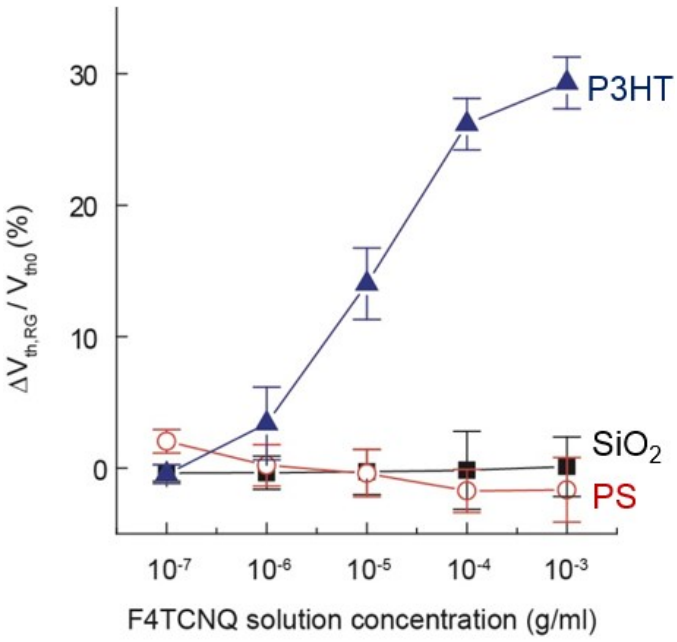

Figure 2.15. Distributions of $\Delta V_{th,RG}$ of each RG normalized with respect to each V_{th0} over at least 8 samples.

Figure 2.16 shows conductivity of the doped P3HT films processed identically to Figure 2.6 that is measured by four-point probe. Increasing conductivity is shown from dopant concentrations higher than 1 μg/ml. This propensity exactly corresponds to that of $V_{th,RG}$ shifting shown in Figure 2.15. Initial conductivity of 3.2×10^{-4} S/cm from the undoped P3HT increases up to about 10 S/cm by doping P3HT films at 1 mg/ml F4TCNQ solution concentration. At this point, the initial hole concentration (p_0) of 2.4×10^{17} cm^{-3} in the pure P3HT film can be calculated via $\sigma = e\mu_h p_0$ based on the initial conductivity of 3.2×10^{-4} S/cm and μ_h of 8.4×10^{-3} cm^2/Vs (Figure 2.16).

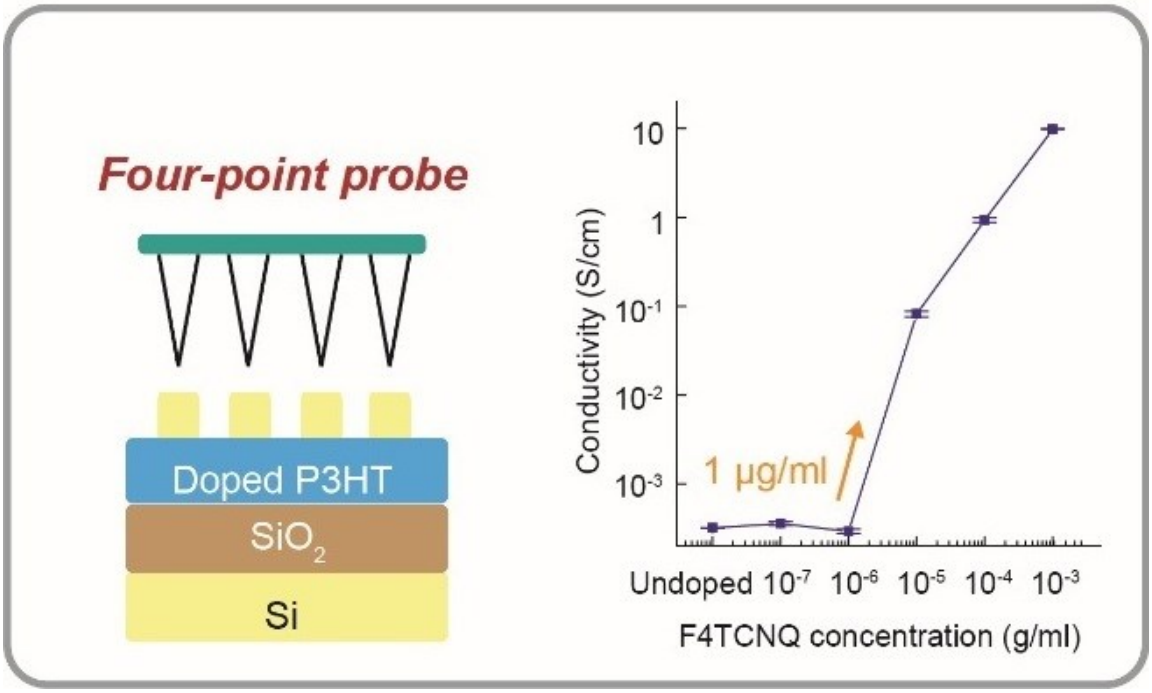

Figure 2.16. Conductivity of doped P3HT films calculated from sheet resistances measured by four-point probe over 4 samples.

We investigate whether there are significant variations in C_{RG} levels from molecular doping effects. C_{RG} is evaluated via MOS capacitors of a bare SiO_2 and doped P3HT/SiO_2 substrates as shown in Figure 2.17. No dramatic changes in C_{RG} are observed upon doping of F4TCNQ in Figure 2.17. Rather, a similar level of capacitance is obtained from all P3HT films doped with different concentrations of F4TCNQ.

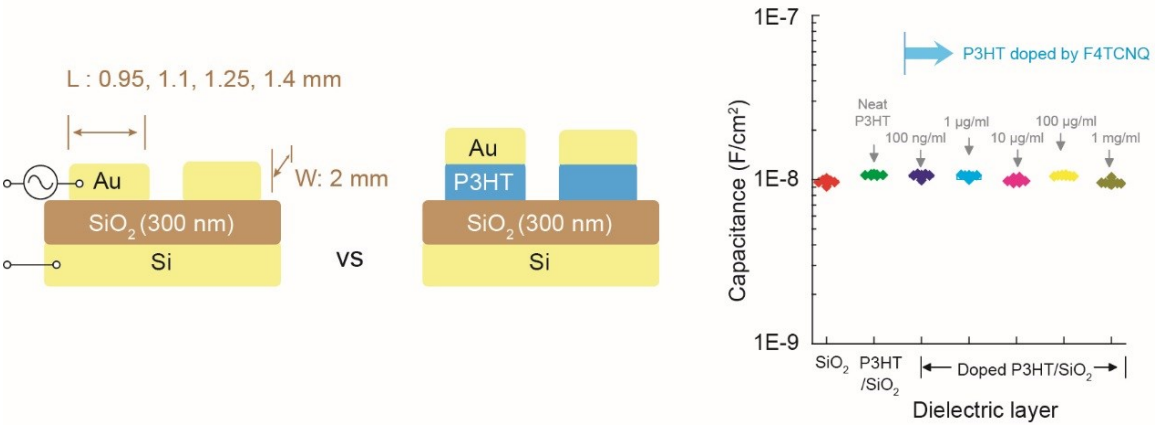

Figure 2.17. Capacitance distributions of doped P3HT/SiO_2 films over 8 samples measured via metal-insulator-semiconductor structure.

Each doped P3HT film is connected as extra resistance and capacitance inputs on the RG as shown in Figure 2.18. No changes in $V_{th,RG}$ are observed from this connection. $V_{th,RG}$ levels from all doped P3HT films remain the same as V_{th} of the intrinsic Si-FET. This result infers that change in conductivity and resistance on the RG system does not lead to a factor to change $V_{th,RG}$.

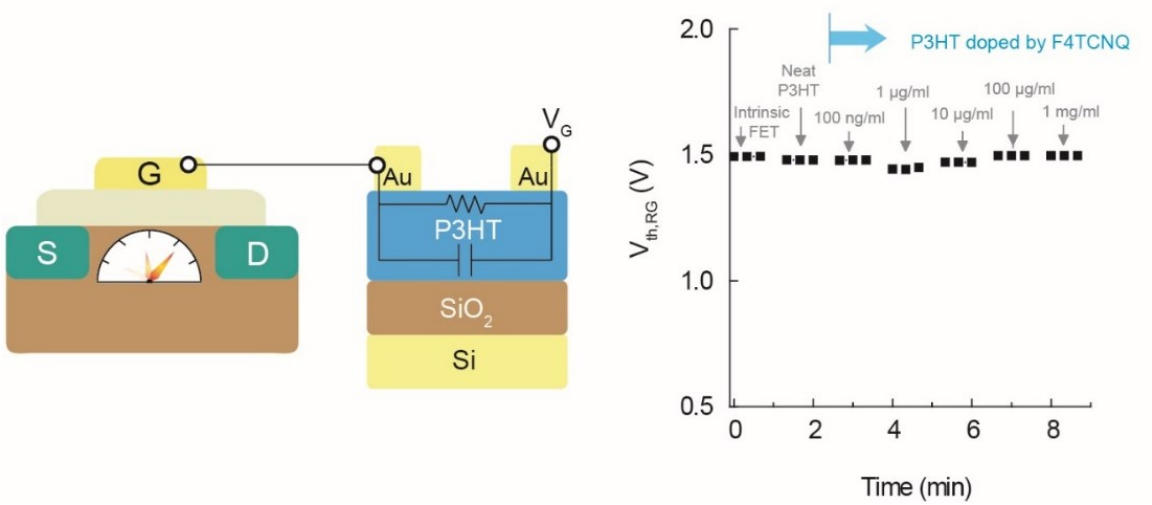

Figure 2.18. $V_{th,RG}$ response of doped P3HT films connected as an extra resistance or capacitance input to the gate of FET.

Figure 2.19 shows V_{th0} distributions of P3HT RGs in the pure ACN but having divergent structures of the P3HT RG such as different thickness of SiO_2 and P3HT layer, a solution contact area, and a type of electrode. A 46-nm-thick P3HT layer is spin coated on an ITO/PET substrate and Si/SiO_2 substrates with different oxide thicknesses of 70 nm and 300 nm, respectively. Much thicker P3HT (~1 mm) is achieved by drop-casting on a 300-nm-thick SiO_2 substrate. Interestingly, any structural variation in the RG leads to a similar level of V_{th0} once they have the same interface (i.e. P3HT and ACN). This indicates that the fabrication variables in C_{RG} applied above are insignificant compared to our large measured doping area of C_{RG} (at least 0.5 cm diameter) which is used to make a contact with F4TCNQ solution on $P3HT/SiO_2$. Likewise, a larger doping area (2 cm diameter) leads to a similar V_{th0} level. This is because the large measured area enables the effect of C_{RG} negligible in relation to the total capacitance of RG FET as is a case for the C_{DL}.

Therefore, V_{th0} is given by the intrinsic property of P3HT in the pure ACN and $V_{th,RG}$ shifts from V_{th0} reflecting the changed series voltage perturbation by P3HT as doped by F4TCNQ.

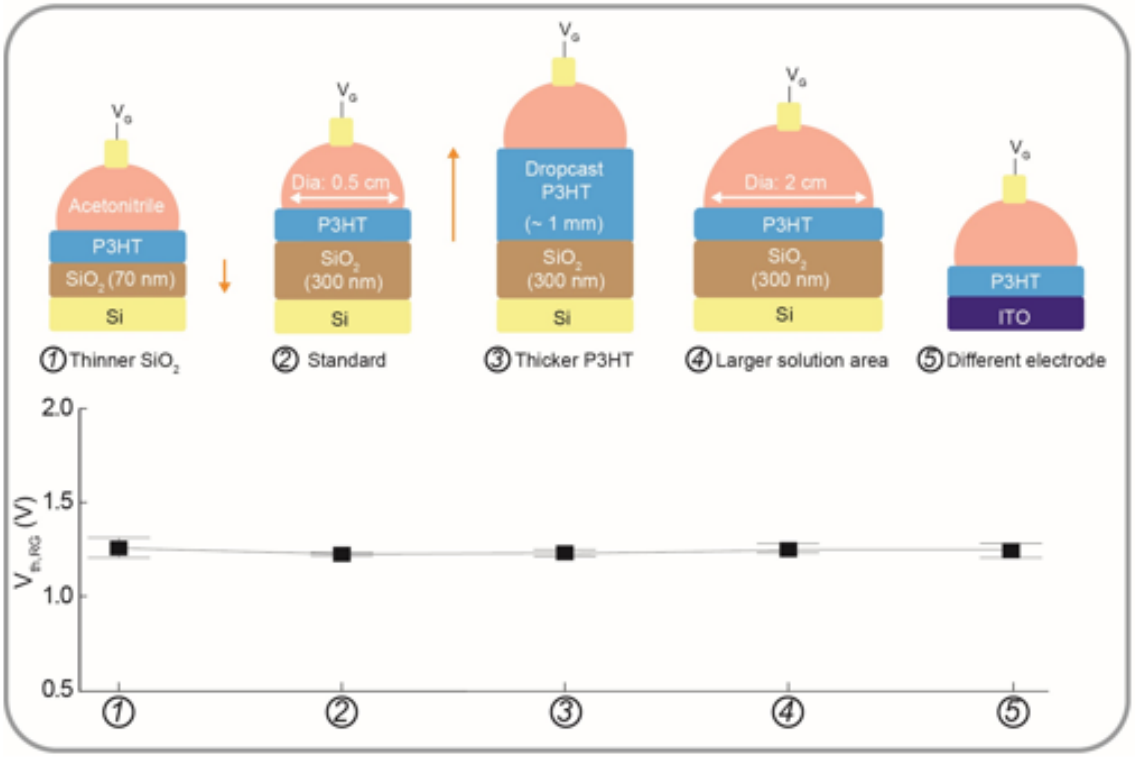

Figure 2.19. $V_{th,RG}$ distributions over at least eight samples of each case of P3HT RG measured in the same ACN. Different structures of P3HT RGs are prepared: 1. Spin-coated P3HT (46 nm) on SiO_2 (70 nm); 2. Spin-coated P3HT (46 nm) on SiO_2 (300 nm); 3. Drop-casted P3HT (1 mm) on SiO_2 (300 nm); 4. Spin-coated P3HT (46 nm) on SiO_2 (300 nm) but having larger solution contact (Diameter: 2 cm); 5. Spin-coated P3HT (46 nm) on ITO/PET substrate.

Fabrication variables above results in no changes in V_{th0}. This supports equation (1.12), $\Delta V_{th,RG} = \Delta\varphi_s \; or \; \Delta\Phi_{RG}$, inferring the RGFET only translates interface potentials on RG modules.

Thicker P3HT layers, however, provoke larger shifts in $V_{th,RG}$ during doping reactions. Figure 2.20 shows $V_{th,RG}$ responses from RGs with different thickness of SiO_2 and P3HT layer. Insignificant difference in $V_{th,RG}$ curves is observed from different thicknesses of SiO_2 (70 nm vs 300 nm) with the same P3HT layer (45 nm). This is because the same amount of F4TCNQ interacts with the same P3HT layer.

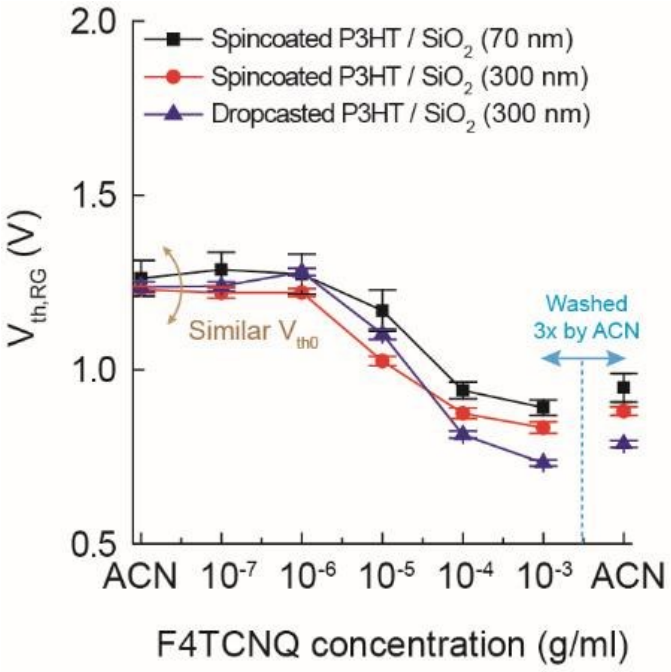

Figure 2.20. $V_{th,RG}$ distributions of RGs with spin-coated P3HT on a 70-nm- and 300-nm-thick SiO_2 and drop-casted P3HT on a 300-nm-thick SiO_2 for F4TCNQ solution concentrations over at least 8 samples.

However, a thick P3HT film (~ 1 mm) made by drop-casting produces larger $V_{th,RG}$ shifts over all ranges of F4TCNQ concentrations, compared to those of thin P3HT layers. This indicates the increase in number of electroactive sites per area in thick P3HT layer because of diffusion of F4TCNQ into the thick P3HT layer.

Our RGFET also characterizes different redox potentials of electron acceptors such as TCNQ and TCNE in terms of different $V_{th,RG}$ shifts as shown in Figure 2.21. Fluorine atoms shown in F4TCNQ with higher electronegativity promote more electron transfer than TCNQ (Figure 2.21a).

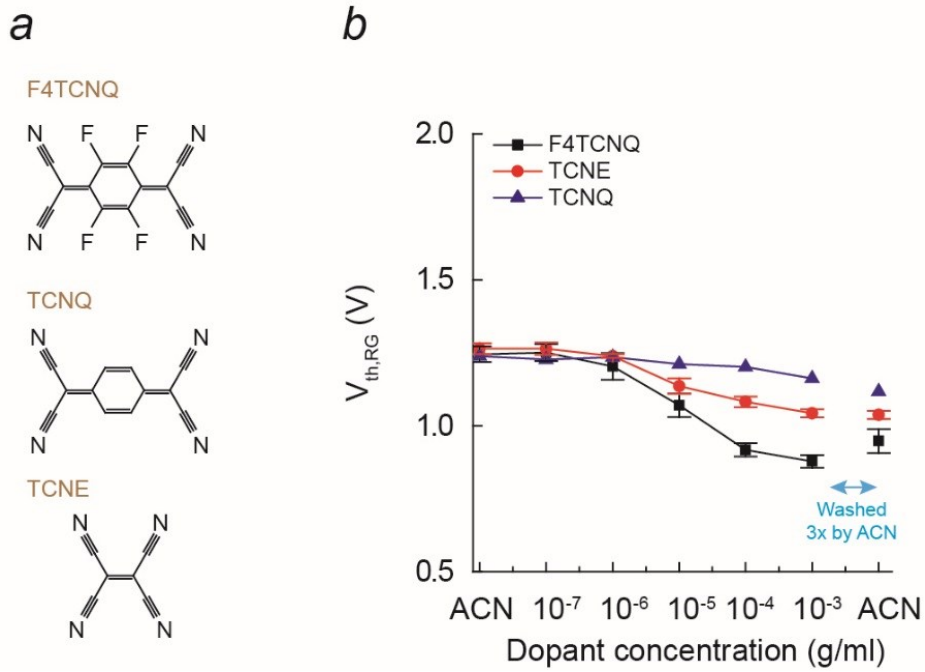

Figure 2.21. (a) Chemical molecule structure of F4TCNQ, TCNQ, and TCNE. (b) $V_{th,RG}$ distributions of P3HT/SiO_2 RG over at least 6 samples vs. each dopant concentration of F4TCNQ, TCNE, and TCNQ.

TCNE has a similar electronegativity to that of TCNQ but the molecular size of TCNE is much smaller than that of TCNQ. Figure 2.21b presents $V_{th,RG}$ distributions from each dopant. While all electron accepters reduce $V_{th,RG}$ levels relative to their each V_{th0} with increasing dopant concentrations, there is no full restoration of the changed $V_{th,RG}$ after washing off surfaces as was a way of F4TCNQ.

The weaker electron acceptor TCNQ presents relatively smaller shifts in $V_{th,RG}$ compared to that of F4TCNQ. Interestingly, TCNE reveals a larger $V_{th,RG}$ shift than TCNQ despite their similar redox potentials in both molecules. $V_{th,RG}$ at 1 mg/ml concentration of each dopant are compared in Figure 2.22. A larger $V_{th,RG}$ shift in TCNE is possibly because of the smaller size of TCNE which allows better diffusion into P3HT domains. This is an example that the RGFET characterization offers new information and insight into conventional chemical reactions.

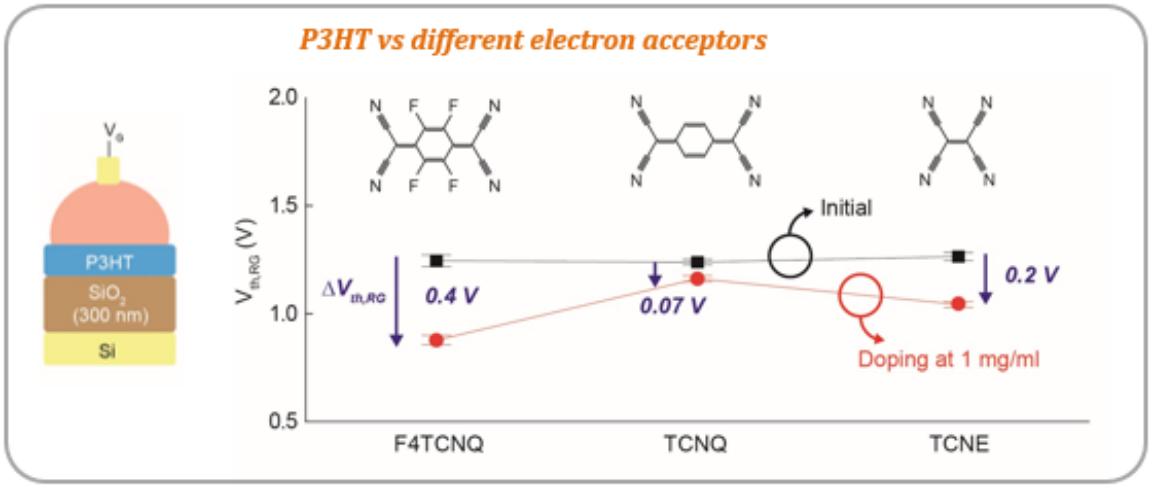

Figure 2.22. Distributions of V_{th0} and $V_{th,RG}$ at 1 mg/ml concentration of each dopant from P3HT RG contacting with F4TCNQ, TCNE, and TCNQ over at least 6 samples.

2.3.3 Calculations of hole carrier concentrations and mobilities

A new model to quantify hole carrier concentrations in the doped P3HT is proposed by connecting model of $V_{th,RG}$ shift with the generation of holes upon doping the surface of the P3HT film with varying concentrations of F4TNCQ. Electrochemical fluctuations in the potential of Ag/AgCl reference electrodes is negligible (~μV/min). That is, Φ_{Ref}, E_{Ref}, and χ^{Sol} shown in equation (1.11) are almost consistent in the RGFET system. As we only vary the concentration of F4TCNQ in ACN solution, ϕ_S that relied on proton concentrations would be constant in the measurements. $\Delta\Phi_{RG}$ in equation (1.12) is the only possible factor to cause $\Delta V_{th,RG}$.

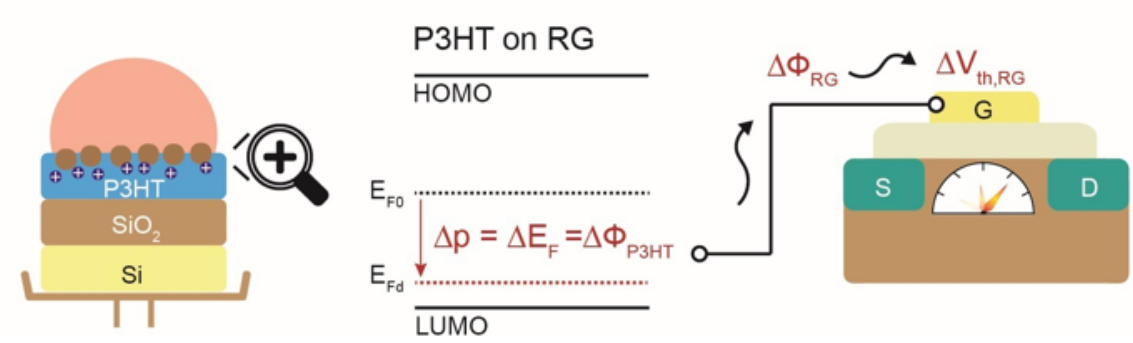

Figure 2.23. Schematic image of a concept to relate $\Delta V_{th,RG}$ to the induced hole concentrations in P3HT.

It is well known that change in hole concentrations in a semiconducting layer results in change in Fermi level and in a work function of a semiconducting layer. The same principle is applied to the case of P3HT film as described:

$$\Delta E_F = \Delta \Phi_{P3HT} \qquad (2.1)$$

We assume no loss in hole concentrations from any electron transfer and interface traps between SiO_2 and P3HT. By combining equation (1.12) and (2.1), the following relation can be newly derived:

$$\Delta E_F = \Delta \Phi_{P3HT} = \Delta \Phi_{RG} = \Delta V_{th,RG} \qquad (2.2)$$

Figure 2.23 shows a schematic image to depict the equation (2.2). At equilibrium, the Fermi levels of undoped (E_F) and doped P3HT (E_{Fd}) are described with the equations of classic semiconductor physics as following:

$$E_F = -kT \ln\left(\frac{p_0}{N_v}\right) + E_{HOMO}$$

$$E_{Fd} = -kT \ln\left(\frac{p_d}{N_v}\right) + E_{HOMO}$$

where p_0 and p_d are hole carrier concentration before and after doping, respectively. E_{HOMO} is energy level of the highest occupied molecular orbital, k is the Boltzmann constant, and T is temperature (K). N_v is defined as

$$N_v = 2\left(\frac{2\pi m_p^* kT}{h^2}\right)^{3/2}$$

where m_p^* is effective mass of holes and h is Planck's constant.

ΔE_F ($E_{Fd} - E_F$) would be:

$$\Delta E_F = kT\ln\left(\frac{p_0}{p_d}\right) \qquad (2.3)$$

By relating equation (2.2) to (2.3) together, ΔE_F can be described in terms of $\Delta V_{th,RG}$:

$$\Delta E_F = kT\ln\left(\frac{p_0}{p_d}\right) = \Delta V_{th,RG}$$

Finally, we arrive at equation to describe hole concentrations after doping in terms of $\Delta V_{th,RG}$ by rearranging the equation above:

$$p_d = p_0 \exp\left(-\frac{\Delta V_{th,RG}}{kT}\right) \qquad (2.4)$$

where p_0 of 2.4×10^{17} cm^{-3} is calculated from Figure 2.16.

Meanwhile, hole concentrations of the doped P3HT are calculated by using spectra of UV-Vis NIR spectra (Figure 2.6) by the conventional method, which starts with the following equation:

$$c = \frac{A}{\varepsilon l} \qquad (2.5)$$

where c is molar charge carrier concentration, l is thickness of the P3HT film (46 nm), A is absorbance of the species formed after doping, and ε is molar extinction coefficient. A value was calculated by subtracting absorption peak at 644 nm (baseline) from that of F4TCNQ at 771 nm. ε of $2 \times 10^5\ /Mcm$ was used according to the literature value for P3HT (Journal of Colloid and Interface Science 2017, 488 373–389). Finally, the acutual p_d in the doped P3HT is obtained from the following equation:

$$p_d = c \times 6.023 \times 10^{23}$$

However, the reliable values in hole concentrations are only shown from heavily doped films (F4TCNQ solution concentrations ≥100 $\mu g/ml$). Otherwise, dopant peaks for lightly-doped films are indistinguishable (Figure 2.6).

Hole concentrations calculated by equation (2.4) and (2.5) are shown in Figure 2.24. For heavily doped films ($\geq 100\ \mu g/ml$), calculated hole concentrations are comparable from both analyses. However, UV-VIS NIR spectroscopy is limited in its ability to characterize lightly doped P3HT films. RGFET characterization of doping effects provided higher resolutions for molecular doping effects and precise quantification of carrier concentrations compared to the conventional spectroscopic analysis.

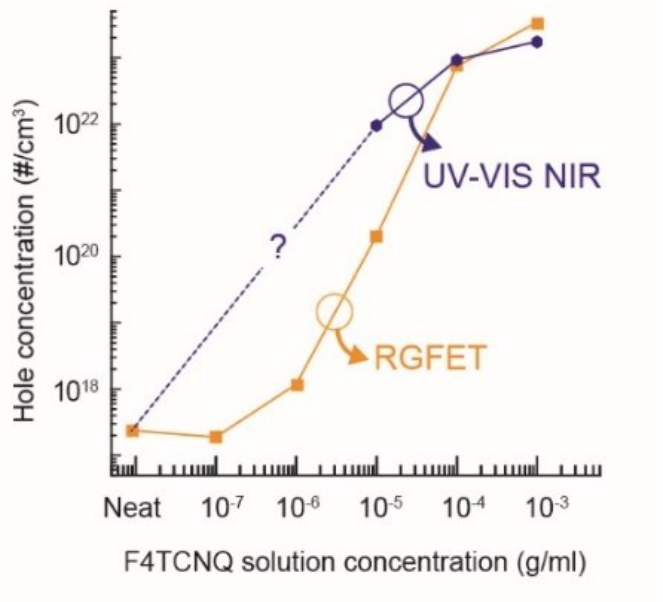

Figure 2.24. Hole concentrations calculated by $V_{th,RG}$ shifting model of RGFET and UV-Vis NIR spectra.

We further expand equation (2.4) for calculation of mobility by using the very basic equation, $\sigma = e\mu_h p_0$ as shown below:

$$\mu_h = \frac{\sigma}{ep_0} \exp\left(\frac{\Delta V_{th,RG}}{kT}\right) \qquad (2.6)$$

Figure 2.25 shows hole mobility derived from equation (2.6). It should be noted that hole mobility calculated here is only based on $\Delta V_{th,RG}$. The mobility value of the pure P3HT film calculated by the RGFET system (8.39 x 10^{-3} cm^2/Vs) is comparable to that of the P3HT OFET (8 x 10^{-3} cm^2/Vs) in Figure 2.5, which verifies equation (2.6). In Figure 2.25, heavily doped P3HT layers show the reduction tendency in hole mobility possibly because of being rougher morphology by F4TCNQ aggregations on P3HT surfaces. The

F4TCNQ that is sequentially added to the P3HT surfaces leads to crystallites of a certain size at high concentrations of F4TCNQ, making rougher morphology. All electrical parameters that have been used for calculations are tabulated in Table 2.1.

As a result, this technique shows a new way to calculate hole mobility of conjugated polymer thin films by placing them on the RG module without needing to achieve FET structures of the conjugated polymer.

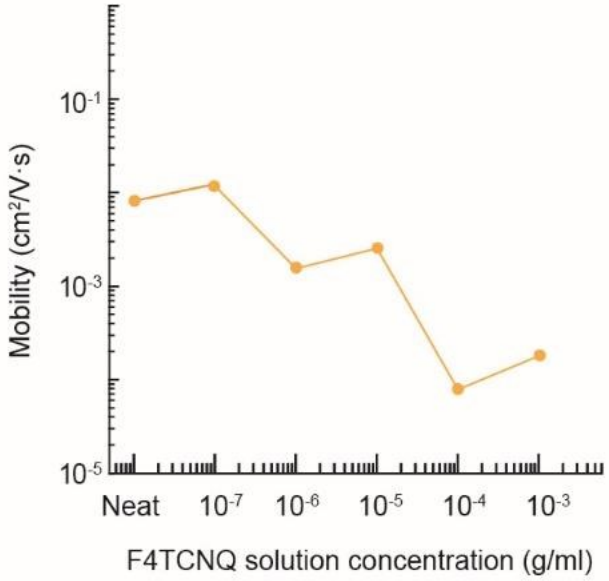

Figure 2.25. Hole mobility calculated by equation 2.6.

Table 2.1. Electrical parameters used in calculations.

Samples	σ (S/cm)	$\Delta V_{th,RG}$ (V)	p (#/cm^3) : RGFET	p (#/cm^3) : UV-Vis NIR	μ_h (cm^2/Vs) : RGFET
Neat P3HT	3.18 x 10^{-4}	1.24 (initial)	2.37 x 10^{-17}	N/A	8.39 x 10^{-3}
100 ng/ml F4TCNQ: P3HT	3.57 x 10^{-4}	0.0059	1.88 x 10^{17}	N/A	1.18 x 10^{-2}
1 μg/ml F4TCNQ: P3HT	2.91 x 10^{-4}	-0.041	1.17 x 10^{18}	N/A	1.55 x 10^{-3}
10 μg/ml F4TCNQ: P3HT	0.081	-0.174	2.01 x 10^{20}	9.36 x10^{21}	2.52 x 10^{-3}
100 μg/ml F4TCNQ: P3HT	0.933	-0.327	7.47 x 10^{22}	9.23 x10^{22}	7.80 x 10^{-5}
1 mg/ml F4TCNQ: P3HT	9.88	-0.367	3.42 x 10^{23}	1.75 x10^{23}	1.80 x 10^{-4}
After washing	Not measured	-0.309	3.72 x 10^{22}	Not measured	Not measured

2.3.4 Interface dipoles between metals and F4TCNQ

Interestingly, pure ITO and Au surfaces showed a response similar to that of P3HT films with varying concentrations of F4TCNQ using the same measurement setup. Figure 2.26 shows representative transfer curves from Au and ITO RG with increasing F4TCNQ concentrations.

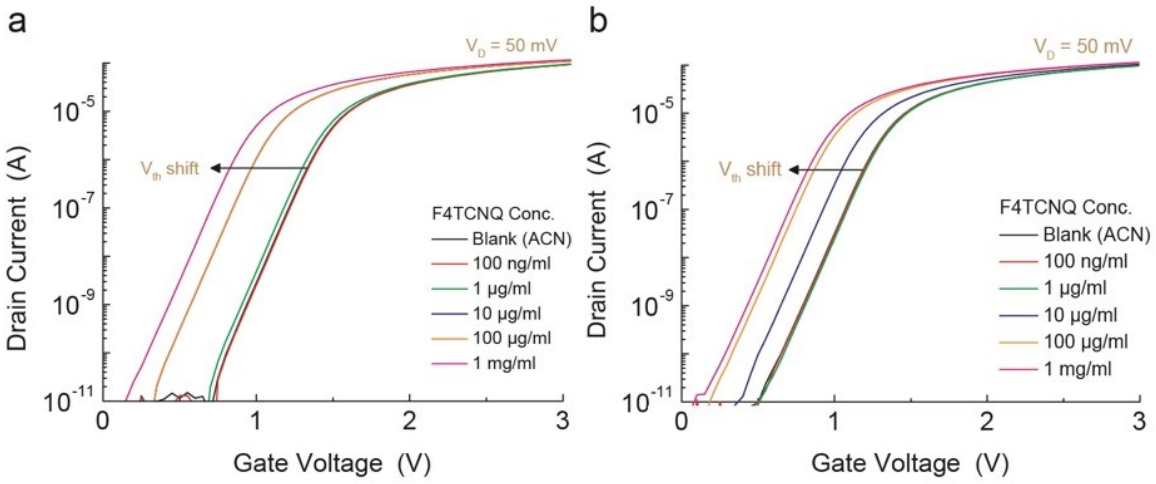

Figure 2.26. Response of representative transfer curves of RGFET with (a) ITO and (b) Au RGs in terms of increasing F4TCNQ concentrations.

This is explained as electron transfer from inorganic electrodes into F4TCNQ occurring by making interface dipoles between F4TCNQ and ITO when it is energetically favorable as shown in energy band diagram in Figure 2.27.

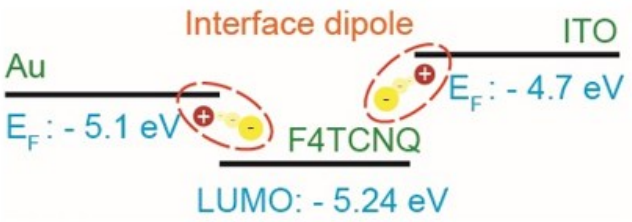

Figure 2.27. Presumed energy band diagram between Au or ITO and F4TCNQ.

Figure 2.28 presents the $V_{th,RG}$ responses as a function of F4TCNQ concentration. A higher V_{th0} in the RGFET setup was observed for the more negatively charged (oxyanionic) ITO surface than that of Au. In addition, ITO responds to even lower concentration of F4TCNQ below 1 μg/mL via charge transfer.

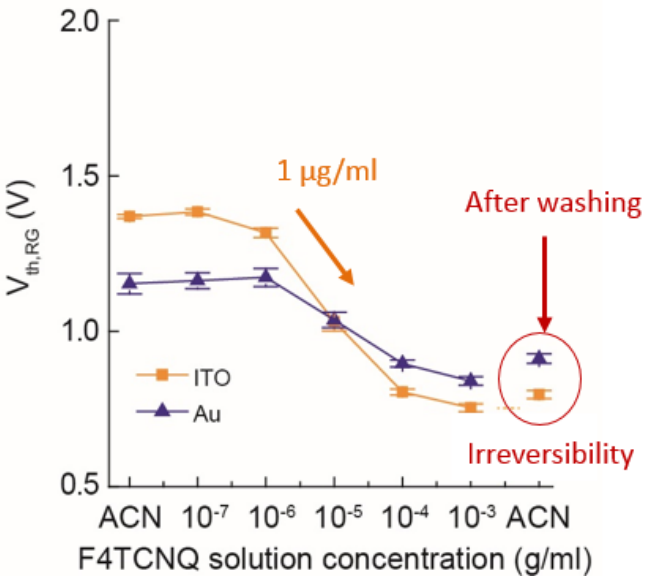

Figure 2.28. $V_{th,RG}$ distributions over at least eight samples of ITO, P3HT/ITO, and Au RGs vs F4TCNQ concentrations.

Saturated shifts in $V_{th,RG}$ upon increasing F4TCNQ concentrations are even shown with ITO and Au. That is, $V_{th,RG}$ is similarly saturated as surface dipole sites were fully occupied by F4TCNQ, as was the case for P3HT. In Figure 2.28, the restoration of $V_{th,RG}$ of ITO and Au RGs to each original value after washing off 1 mg/mL F4TCNQ solution using pure ACN is not observed, just as for the case of P3HT. We further investigate washing effects of ITO surface reacted with F4TCNQ in Figure 2.29.

Despite adding four more washing steps for F4TCNQ:ITO, F4TCNQ still remains on the ITO as shown in Figure 2.29a. Variation of $V_{th,RG}$ according to additional washing steps is compared in Figure 2.29b. After 3 times washing steps, $V_{th,RG}$ becomes stable, meaning that excessed F4TCNQ is washed off and stable F4TCNQ layer remains on the ITO.

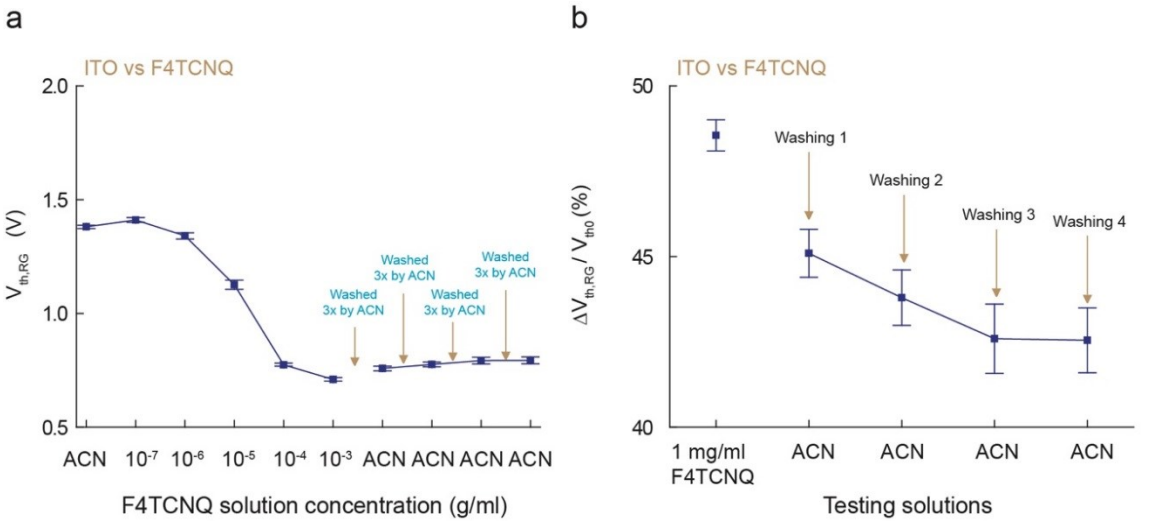

Figure 2.29. (a) $V_{th,RG}$ distributions over at least 6 samples vs F4TCNQ solution concentrations with 4 more washing steps. (b) Variation of $V_{th,RG}$ at 1 mg/ml F4TCNQ and the neat ACN after each washing step with respect to V_{th0}.

This is more clearly shown in XPS spectra of the washed F4TCNQ:ITO surface by flowing the pure ACN for 5 s (Figure 2.30). Despite significant decreases of intensity of F 1s and N 1s peaks, there is remaining F4TCNQ on ITO surfaces. Such an irreversibility of reactions between ITO and F4TCNQ indicates the ionized F4TCNQ on the electron donor surfaces of ITO, either by doping or very strong intermolecular interactions, creating surface dipoles.

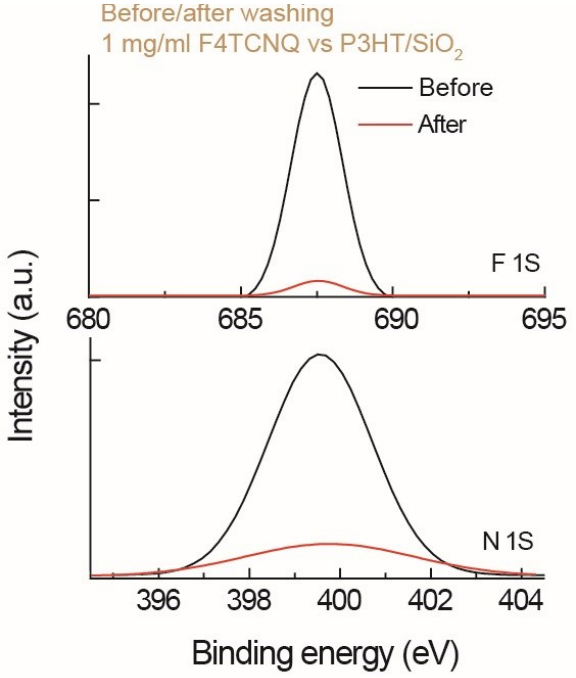

Figure 2.30. XPS spectra regarding fluorine and nitrogen on 1 mg/mL F4TCNQ:ITO surface before/after washing.

It would be interesting to compare ITO response with either concentrations of proton or F4TCNQ at the same plot to understand better about general characteristics of

interface dipoles. ITO reveals $V_{th,RG}$ shift in terms of changes in surface potential, which is described with a site-binding model. The maximum sensitivity achievable in terms of a variable of concentration is 59 mV/pH at 25 °C, the well-known Nernst limit. Also, ITO reversibly retrieves electrochemical potentials for each pH value.

Figure 2.31 shows $V_{th,RG}$ response of ITO surfaces for proton and F4TCNQ. ITO has a linear response of 51 mV/M for every 10-fold increase in proton concentration. ITO, however, reveals non-linear and irreversible shift in $V_{th,RG}$ for F4TCNQ concentrations. The slope is measured to be 145 mV/M, beyond the Nernst limit, and $V_{th,RG}$ shifts. This may have indicated chemical reactions beyond simple Coulomb attractions between F4TCNQ and ITO, or interactions on a rough ITO surface. Saturated tendency in $V_{th,RG}$ at high concentrations of F4TCNQ suggests that there are limited electroactive sites for F4TCNQ binding on electron donor ITO surfaces.

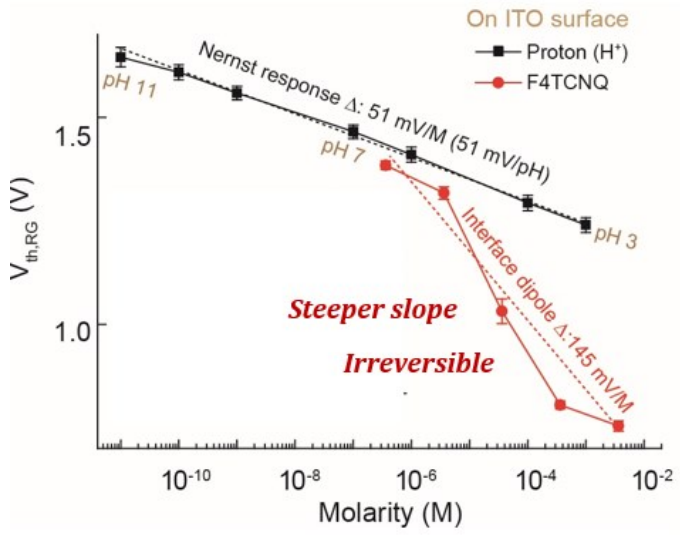

Figure 2.31. $V_{th,RG}$ response of ITO surfaces for proton and F4TCNQ over at least eight samples.

At this point, we compare V_{th0} and $V_{th,RG}$ values at 1 mg/mL F4TCNQ as a function of type of RG substrates in Figure 2.32. V_{th0} levels from each RG are uniform, respectively, reflects initial electrochemical potentials of each surface in ACN. Therefore, V_{th0} only varies with intrinsic properties of materials.

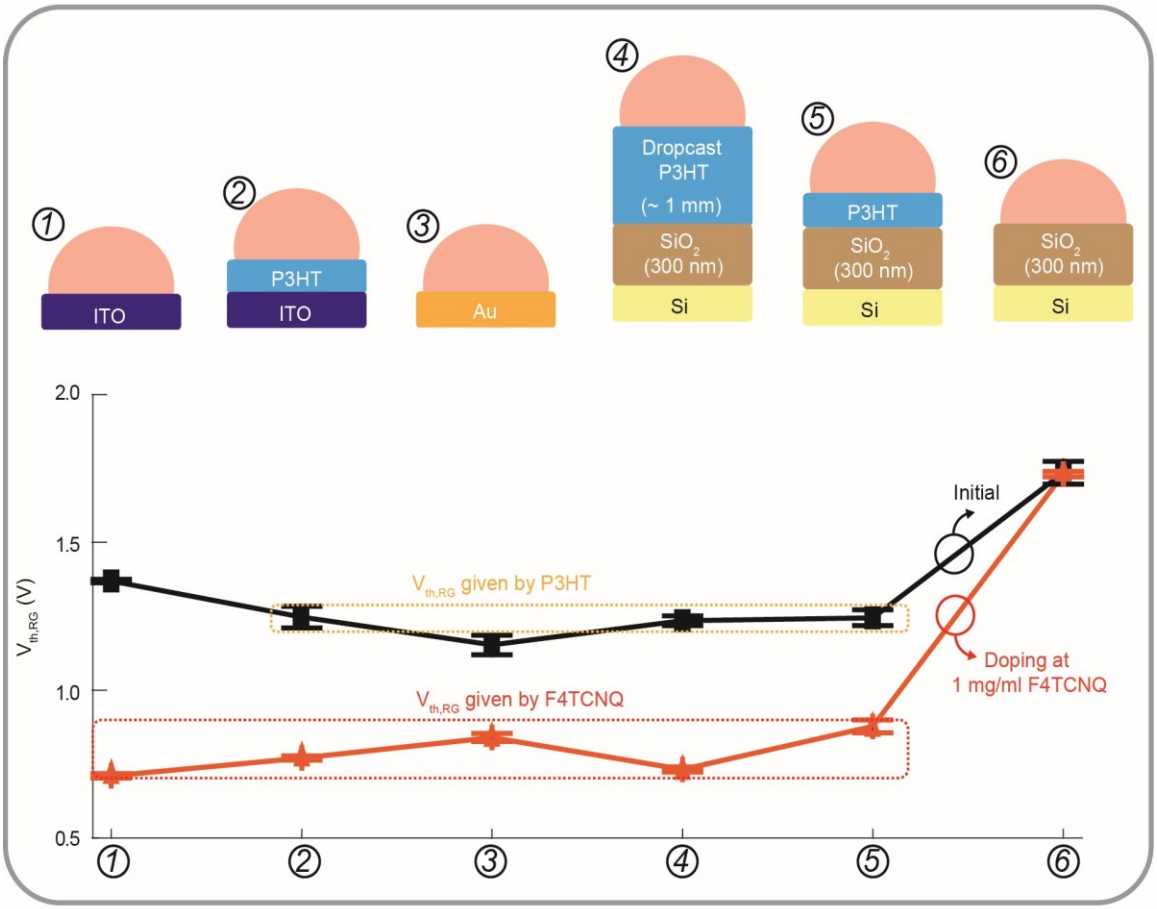

Figure 2.32. $V_{th,RG}$ distributions over at least eight samples versus type of RG substrate under the same solution condition of neat ACN and 1 mg/mL F4TCNQ. Different RG structures are prepared: 1. ITO/PET; 2. Spin-coated P3HT/ITO; 3. Au/PET; 4. Drop-casted P3HT/SiO_2; 5. Spin-coated P3HT//SiO_2; 6. Pure SiO_2.

To be specific, any RG incorporating P3HT surfaces shows a similar V_{th0} level (i.e. ~1.2 V) although the P3HT layer is deposited on different substrates such as SiO_2 and ITO. Likewise, F4TCNQ shows propensity that imposes specific $V_{th,RG}$ by interacting with each different RG (i.e., ~0.8 V at 1 mg/mL F4TCNQ). This behavior could be interpreted as a similar number density of F4TCNQ occupying and oxidizing the sites on each donor surface and the majority of F4TCNQ molecules undergoing integer charge transfer with the electron donors. It also indicates constraints in oxidizing sites by F4TCNQ with any electron donor surface which leads to a saturated $V_{th,RG}$ shift at high concentration of F4TCNQ. Changes in ϕ_{RG} given by F4TCNQ are a critical factor in making $V_{th,RG}$ shifts. However, $V_{th,RG}$ at 1 mg/mL of F4TNCQ is slightly varied depending on the types of RG surface possibly because of different numbers of oxidizing sites of each RG. It is noted that $V_{th,RG}$ at 1 mg/mL of F4TNCQ from very thick drop-cast P3HT is lower than that of spin-coated P3HT.

2.3.5. Diffusion monitoring system by RGFET

We now turn our attention to additional applications of the RGFET to monitor the diffusion of small molecules in a passive polymer such as PS. Briefly, ITO sensitive to F4TCNQ is used as sensing membrane for F4TCNQ that penetrated through a passive polymer on the ITO as shown in Figure 2.3. F4TCNQ responses are compared using four different RGs of PS/SiO_2, ITO, PS/ITO, and XLPS/ITO as shown in Figure 2.33.

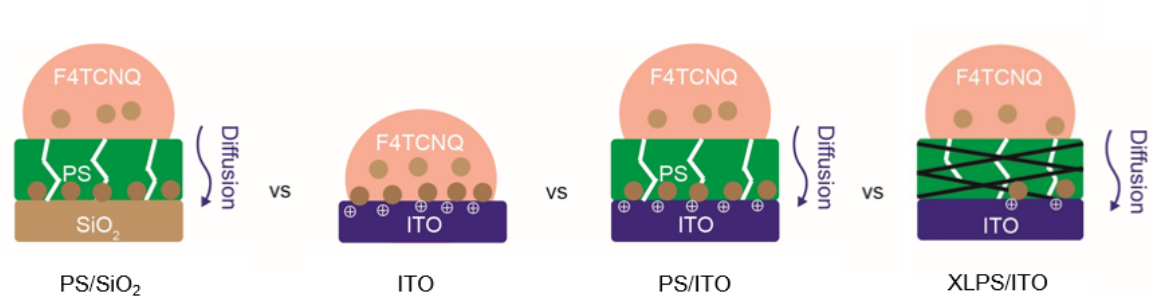

Figure 2.33. Schematic image of RG setups for diffusion monitoring system.

Response of transfer curves from PS/ITO RG for F4TCNQ solution concentrations are shown in Figure 2.34. Transfer curve starts to respond the concentrations of F4TCNQ at least higher than 10 μg/ml F4TCNQ. $V_{th,RG}$ of PS/ITO at 1 mg/ml F4TCNQ is exactly overlapped with that of ITO at 1 mg/ml F4TCNQ. It is noted that the pure ITO without the PS layer revealed $V_{th,RG}$ changes for the concentration of F4TCNQ even below 1 μg/ml (Figure 2.31).

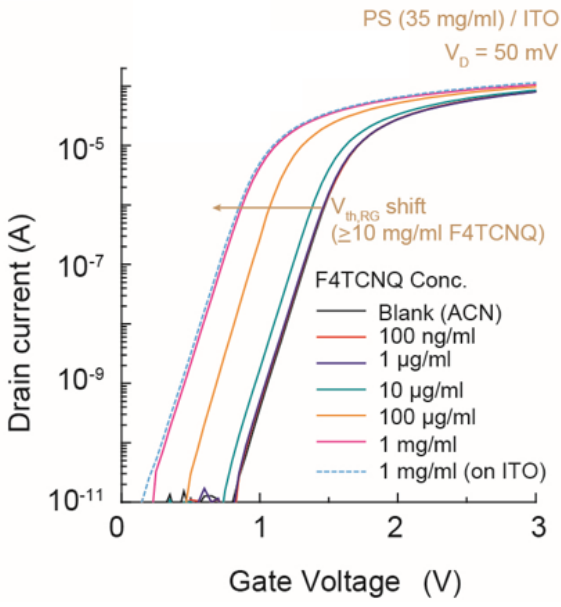

Figure 2.34. Representative response of transfer curves from PS/ITO RG for F4TCNQ solution concentrations

Furthermore, there is even no change in transfer curves from PS/SiO_2 as shown in Figure 2.11c because there are no interacting materials with F4TCNQ molecule over the PS/SiO_2 RG.

Figure 2.34 shows representative $V_{th,RG}$ response from the neat ITO, PS/SiO_2, and PS/ITO RG over time, clearly showing the tendency mentioned above. This result indicates the diffusion of a portion of F4TCNQ is limited by a PS layer.

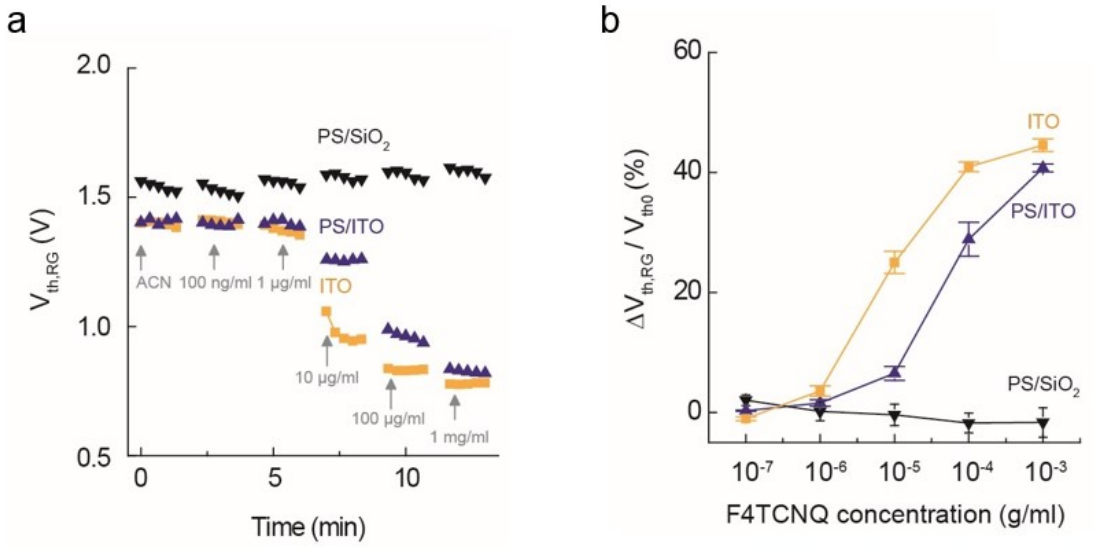

Figure 2.34. (a) Representative $V_{th,RG}$ response from the neat ITO, PS/SiO_2, and PS/ITO RG for F4TCNQ solution concentrations over time. (b) Distributions of $V_{th,RG}$ variation with respect to V_{th0} from neat ITO, PS/SiO_2, and PS/ITO RGs over at least eight samples.

Diffusion of F4TCNQ in XLPS is measured. Cross-linking of PS polymer chains is done by using polystyrene-co-4-vinylbenzocyclobutane under high temperature of 180 °C (Figure 2.35a). Cross-linked polymer chains provide more rigid structures in the polymer layer opposing solution diffusion than normal PS.

Representative transfer curves from thick XLPS RG are shown in Figure 2.35b. $V_{th,RG}$ response is mostly shown under high concentration of F4TCNQ solution of 1 mg/mL, indicating higher tolerance against the diffusion of F4TCNQ molecules.

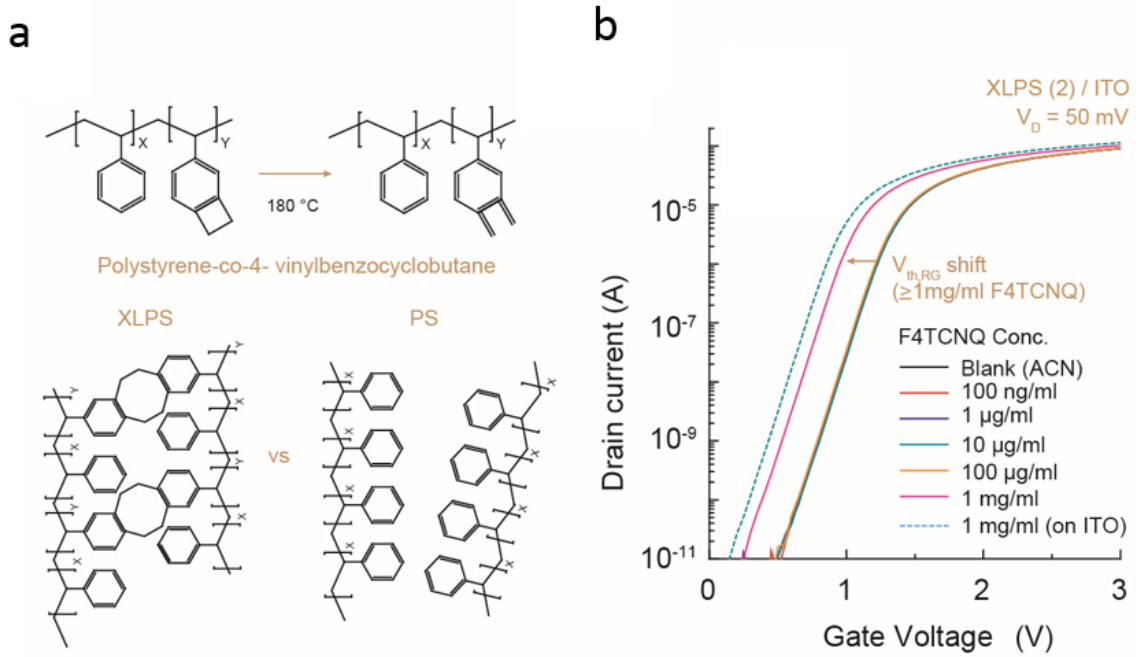

Figure 2.35. (a) Chemical polymer structure of PS and XLPS. (b) Representative response of transfer curves from XLPS/ITO RG for F4TCNQ solution concentrations.

The thin XLPS, however, show larger $V_{th,RG}$ response that is comparable to that of normal PS as shown in Figure 2.36a. This diffusion monitoring system is different from any conventional methods based on UV−vis−NIR and PL spectroscopy that required interactions between host materials and diffused molecules.

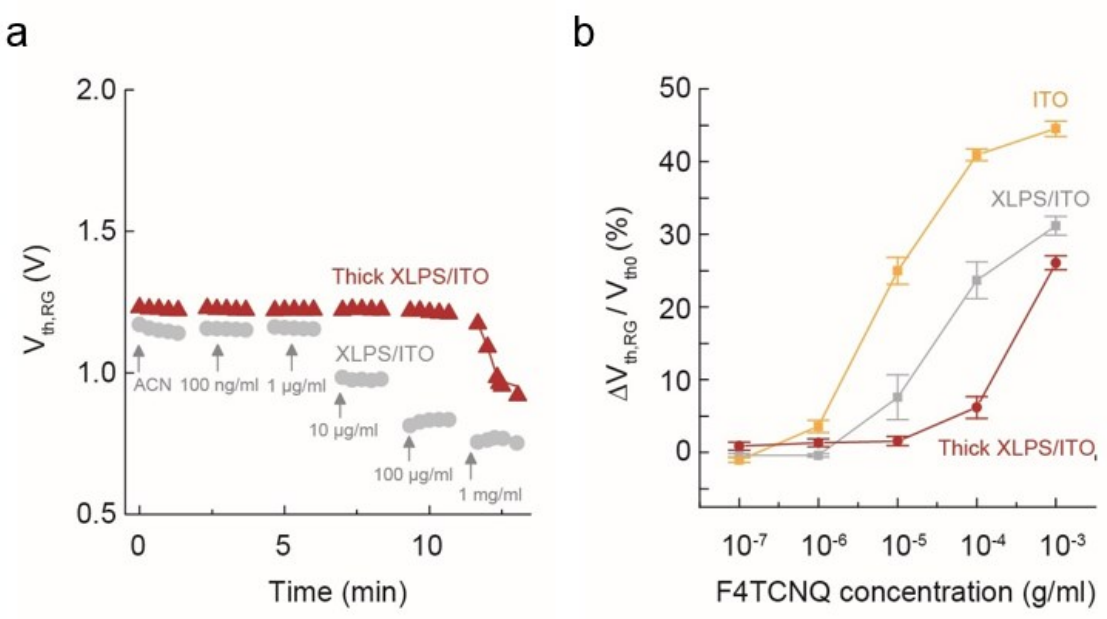

Figure 2.36. Representative $V_{th,RG}$ response from thin and thick XLPS RGs for F4TCNQ solution concentrations over time. (b) Distributions of $V_{th,RG}$ variation with respect to V_{th0} from thin and thick XLPS RGs over at least eight samples.

2.4. Conclusion

The RGFET system is newly used for characterization of molecular doping effects between P3HT and F4TCNQ. Hole concentrations of P3HT doped via sequential doping

methods are quantified by relating them to $V_{th,RG}$ shifts and work function changes in P3HT. In the detection mechanism, F4TCNQ occupies sites on electron donor surfaces by creating surface dipoles and the associated hole carriers impose positive charges in P3HT, which is detected by an FET transducer. As F4TCNQ fully covers the surfaces on electron donors, electronic potentials of electron donors are fully determined by F4TCNQ irrespective of types of materials. Almost all the bound F4TCNQ undergoes integer charge transfer with those electron donors. Hole mobility of doped P3HT is derived from hole concentrations calculated from $V_{th,RG}$ shifts.

We monitor physical diffusion of F4TCNQ in PS driven by concentration gradients using an FET setup. Conventional diffusion monitoring system based on UV−vis−NIR and PL spectroscopy requires interactions between host materials and diffused molecules. In this work, this FET analysis tool offers a means of monitoring the physical diffusion of small molecules, exemplified by F4TCNQ, in the passive polymer polystyrene, driven by concentration gradients. My FET detection system offers quantification of the diffused small chemical molecules between specific polymer layers under electric fields. Inter-diffusions of molecules between permeated, soft organic materials under electric fields is particularly one of the most profound issues in organic electronics, provoking degradations of electric performance and instability. This is because diffused molecules change intrinsic electrical properties of organic materials by acting as impurity in pure organic materials. While highly limited technique has shown to characterize this diffusion effects so far, my FET detection technique would offer a way to monitor kinetics of inter-diffusions between polymer and small chemical molecules. Also, better understanding in critical factors in diffusions and sequentially proper designing of materials lead to a way to improve stability

and reliability of organic-based electronics over diverse fields of display, energy device, biosensors, and organic FET technique.

2.5. References

(14) Shirakawa, H.; Louis, E. J.; Macdiarmid, A. G.; Chiang, C. K.; Heeger, A. J. *J Chem Soc Chem Comm* **1977**, 578.

(15) Gould, C. M.; Bates, D. M.; Bozler, H. M.; Heeger, A. J.; Druy, M. A.; Macdiarmid, A. G. *Phys Rev B* **1981**, *23*, 6820.

(16) Druy, M. A. *Synthetic Met* **1986**, *15*, 243.

(17) Zhang, Y.; de Boer, B.; Blom, P. W. M. *Adv Funct Mater* **2009**, *19*, 1901.

(18) Duong, D. T.; Wang, C. C.; Antono, E.; Toney, M. F.; Salleo, A. *Org Electron* **2013**, *14*, 1330.

(19) Jacobs, I. E.; Aasen, E. W.; Oliveira, J. L.; Fonseca, T. N.; Roehling, J. D.; Li, J.; Zhang, G. W.; Augustine, M. P.; Mascal, M.; Moule, A. J. *J Mater Chem C* **2016**, *4*, 3454.

(20) Kang, S. D.; Snyder, G. J. *Nat Mater* **2017**, *16*, 252.

(21) Jacobs, I. E.; Aasen, E. W.; Oliveira, J. L.; Fonseca, T. N.; Roehling, J. D.; Li, J.; Zhang, G. W.; Augustine, M. P.; Mascal, M.; Moule, A. J., J. Mater. Chem. C 2016, 4, 3454−3466.

(22) Scholes, D. T.; Yee, P. Y.; Lindemuth, J. R.; Kang, H.; Onorato, J.; Ghosh, R.; Luscombe, C. K.; Spano, F. C.; Tolbert, S. H.; Schwartz, B. J. *Adv Funct Mater* **2017**, *27*.

(23) Chew, A. R.; Ghosh, R.; Shang, Z. R.; Spano, F. C.; Salleo, A. *J Phys Chem Lett* **2017**, *8*, 4974.

(24) Jones, M. L.; Huang, D. M.; Chakrabarti, B.; Groves, C. *J Phys Chem C* **2017**, *121*, 12504.

(25) Sirringhaus, H.; Brown, P. J.; Friend, R. H.; Nielsen, M. M.; Bechgaard, K.; Langeveld-Voss, B. M. W.; Spiering, A. J. H.; Janssen, R. A. J.; Meijer, E. W.; Herwig, P.; de Leeuw, D. M. *Nature* **1999**, *401*, 685.

(26) Kline, R. J.; McGehee, M. D. *Polym Rev* **2006**, *46*, 27.

(27) Pingel, P.; Schwarzl, R.; Neher, D. *Appl Phys Lett* **2012**, *100*.

(28) Tietze, M. L.; Burtone, L.; Riede, M.; Lussem, B.; Leo, K. *Phys Rev B* **2012**, *86*.

(29) Muller, L.; Rhim, S. Y.; Sivanesan, V.; Wang, D. X.; Hietzschold, S.; Reiser, P.; Mankel, E.; Beck, S.; Barlow, S.; Marder, S. R.; Pucci, A.; Kowalsky, W.; Lovrincic, R. *Adv Mater* **2017**, *29*.

(30) Li, J.; Rochester, C. W.; Jacobs, I. E.; Friedrich, S.; Stroeve, P.; Riede, M.; Moule, A. J. *Acs Appl Mater Inter* **2015**, *7*, 28420.

(31) Li, J.; Rochester, C. W.; Jacobs, I. E.; Aasen, E. W.; Friedrich, S.; Stroeve, P.; Moule, A. J. *Org Electron* **2016**, *33*, 23.

(32) Chang, W. B.; Fang, H. Y.; Liu, J.; Evans, C. M.; Russ, B.; Popere, B. C.; Patel, S. N.; Chabinyc, M. L.; Segalman, R. A. *Acs Macro Lett* **2016**, *5*, 455.

(33) Tyagi, P.; Tuli, S.; Srivastava, R. *J Chem Phys* **2015**, *142*.

(34) Chang, J. F.; Sun, B. Q.; Breiby, D. W.; Nielsen, M. M.; Solling, T. I.; Giles, M.; McCulloch, I.; Sirringhaus, H. *Chem Mater* **2004**, *16*, 4772.

(35) Wang, C. C.; Duong, D. T.; Vandewal, K.; Rivnay, J.; Salleo, A. *Phys Rev B* **2015**, *92*.

(36) Pingel, P.; Neher, D. *Phys Rev B* **2013**, *87*.

Chapter 3

Characterization of polymer-solution interface by RGFET

3.1. Introduction

FET biosensors inevitably contain a solution interface contact on the sensing material where receptors for dissolved biomarkers are placed. A solution interface under the influence of an electric field is a source of electrochemical instability such as electric drift and hysteresis. While mechanistic factors behind drift have been an enigma, drift alone has been one of the most challenging issues for real-time diagnosis, affecting device sensitivity, specificity, and LOD.[37-39]

Organic materials have shown larger electrochemical instability compared to inorganic surfaces[40-42] despite their promising advantages such as low-cost production, transparency, flexibility, and wearabiliy.[43,44] Nonetheless, the chemical, electrical, and physical properties of these organic materials have consistently been enhanced by fine-tuning the structures via molecular synthesis. Recently, conjugated semiconducting polymers based on polyaniline, polypyrrole, and polythiophene have received considerable attention as active sensing layers for organic electrochemical transistors (OECTs) due to their enhanced stability, long lifetime, and fast response for voltage cycles in ionic liquids.[45] At the same time, dopable π-conjugated polymers exhibit vaguely understood interactions such as ionic doping by counter-ions[46] and non-covalent interactions with small charged chemical molecules.[47] Meanwhile, classic amphiphilic co-polymers such as poly(styrene-co-acrylic acid) (PSAA) were proposed to specifically improve the physical stability of a bio-interfacial layer in aqueous solution.[12,48] The polystyrene in PSAA sterically hinders the full functionality of the acid groups on the substrates under aqueous

media exposure. With a variety of options in tailoring specific properties of organic materials, progress in bioelectronics requires better understating of the origin and detailed mechanism of the conundrum associated with the electrochemical instability that stems from the sensing surface properties and the solution behaviors in the applied electric fields.

Drift in FET-biosensors is typically manifested as a relatively slow, monotonic, temporal change in V_{th} under repeating voltage cycles that is not caused by variations in the electrolyte composition and concentrations of biomarkers in solutions as shown in Figure 3.1a. Hysteresis is defined in the V_{th} of transfer curves by measurement through a double sweeping mode as shown in Figure 3.1b. With less dependence on sensing material types, repeating voltage cycles have often resulted in directional increase in V_{th} of n-FET transducers with a specific saturation in drift.[49] This infers that the solution interface above the gate insulator delays the response of charge carriers in the semiconductor of the gate voltage and requires a certain amount of time in order to reach quasi-equilibrium subjected to repetitive external electric fields. This hypothesis leads to several plausible drift factors in classic models, such as the formation of negative space charges either inside or near a gate sensing layer caused by the accumulation and migration of ions,[50,51] injection of electrons,[52] diffusion of OH^- ions,[49,53] and slow response of buried surface sites.[54,55] Another theory described irreversible decreases in dielectric permittivity (ε_r) of the hydrated surface which decrease the total capacitance in the FET system resulting in increased V_{th}.[39] Such similar drift behaviors observed over a diverse range of sensing materials infers that a similar influence of the electrolyte on the sensing surface can also depend on electric fields but less attention has been paid to this effect in conventional models above.

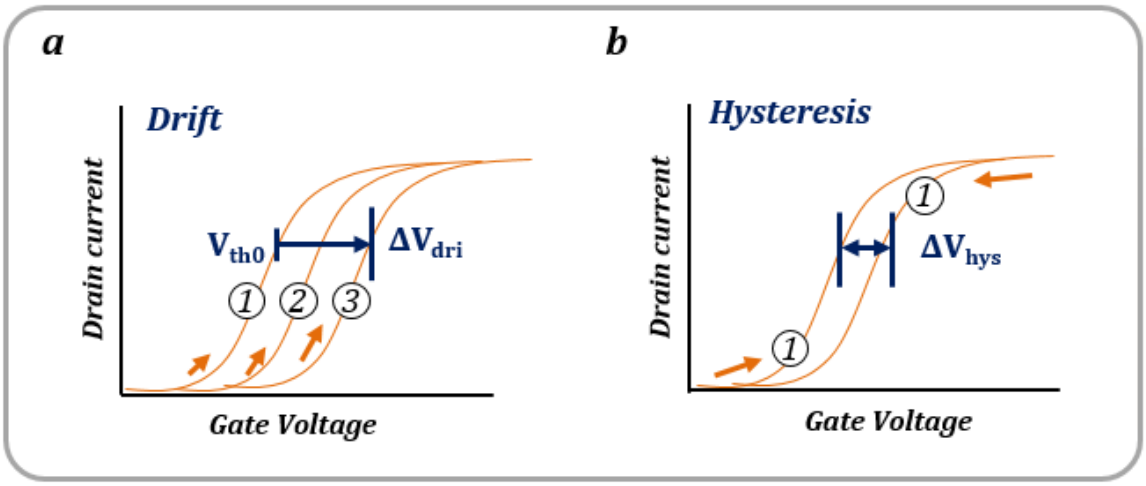

Figure 3.1. Definitions of (a) electrical drift and (b) hysteresis in transfer curve.

The inconsistent ε_r value of solutions associated with the application of electrical fields has been reported in many molecular dynamic (MD) simulations.[56-60] Dipoles are aligned on the material surfaces to minimize the dipole-field interaction energy along an applied electric fields.[61] The development of orientational ordering of dipoles near the interface (saturation effect)[60] as shown in Figure 3.2 gives rise to a charge screening[58] and steep reductions of ε_r of the solutions compared to bulk with decreasing polarizability.[59-62] As a matter of fact, intrinsic surface charge itself affects the density, arrangement, configuration, dynamics, and orientation of ions and polarized molecules at the interface apart from the effects of electric fields. Nonetheless, high enough gate electrical fields make orientational ordering of dipoles onto the interface independent from surface charges, even for hydrophobic surfaces that possess strong repulsive forces with the polarized molecules[63,64]. The saturation effect arisen from external electrical field leads to significant reductions of C_{EDL} [20-21, 28] which is typically a series capacitance leading to the gate electrode of an FET. The MD studies above; however, mostly remained theoretical

simulations combined with a fundamental measurement of the parameter, providing only limited explanation of relevant experimental data.

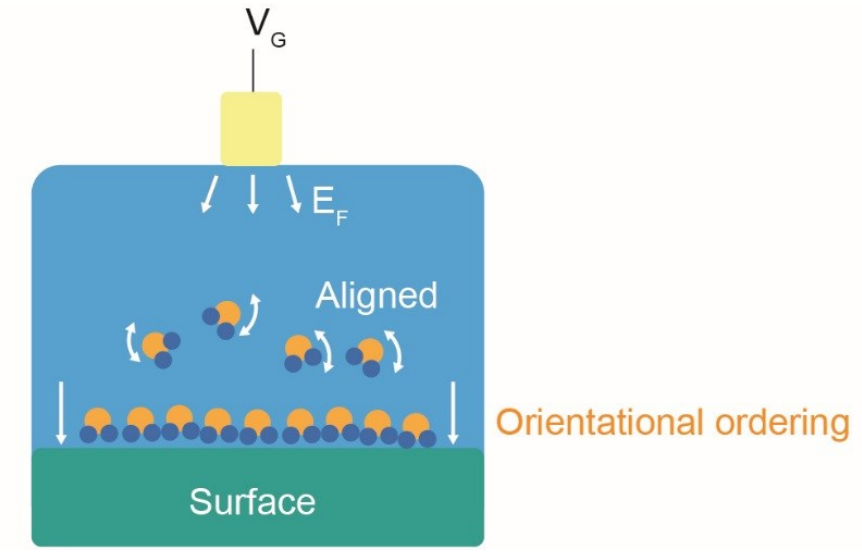

Figure 3.2. Schematic image of orientational ordering of water dioples at the interface due to the applied electric field.

It is difficult to discriminate such a saturation effect on a conjugated polymer in particular by using an OECT structure which has a direct solution contact on the conjugated polymer (no insulator). The drain current of OECTs is determined by multiple species such as hole carriers, mobile ions in solutions, ions that diffuse into conjugated polymers, and interface traps between material interfaces. Also, current flow through a conjugated polymer causes changes in its electrical properties associated with redox reactions. At this point, the RGFET structure, isolating a sensing surface from the FET transducer, is highly desirable to investigate properties of electrochemical interfaces. There is no current flow

in the sensing surface as shown in chapter 1.2.1 and the Si-FET only translates the properties of the electrochemical interface between sensing surface and solution.

In this chapter, I connect drift and hysteresis to slow dipole rearrangement at the interface by observing change in $V_{th,RG}$ $(\Delta V_{th,RG})$ and transconductance (ΔG_m) in the RGFET system. V_{th} of Si-FET transducer (1.5 V) is consistent as shown in Figure 1.9. Therefore, any change in $V_{th,RG}$ is related to change in electrochemical potential of the interface. An additional parameter, G_m, is used for further analysis on the interface. When the G_m of the RGFET varies in a system, this reflects a gate voltage dependence of either the interfacial potential or the impedance of the RG, since the solution and sensing layers are spatially separated from the FET itself. G_m in the typical FET decreases with increasing interface trap densities between the gate dielectric and semiconducting layer

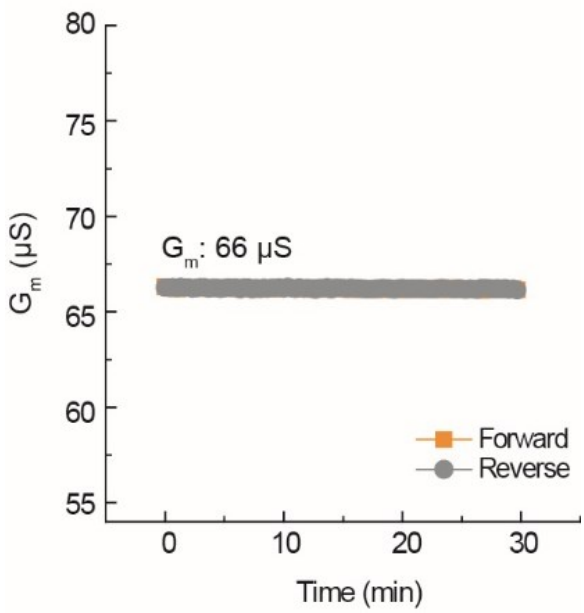

Figure 3.3. G_m of the Si-FET measured by forward/reverse sweeping mode.

In our RGFET system, the interfaces of the Si-FET remain stable over all electrical measurements by showing high G_m of 66 μS (Figure 3.3) before introducing a solution interface on the RG. G_m is calculated to be its maximum value. G_m levels of a Si-FET measured by both forward and reverse sweeping modes are exactly overlapped. This infers that G_m has no voltage dependency in case of a stable Si-FET.

Both the polarized molecules and ions in solutions change their configurations at the interface along with the external gate electric fields, causing gate voltage dependent changes in electronic parameters observed as changes in G_m of the RGFET system as described in Figure 3.4. That is, if there is a change in G_m in the RGFET, effective G_m is attributed to properties of solution interface. That is, high G_m of the RGFET that is close to that of FET indicates a good solution interface, and vice versa. G_m of each RGFET was calculated to be its maximum value.

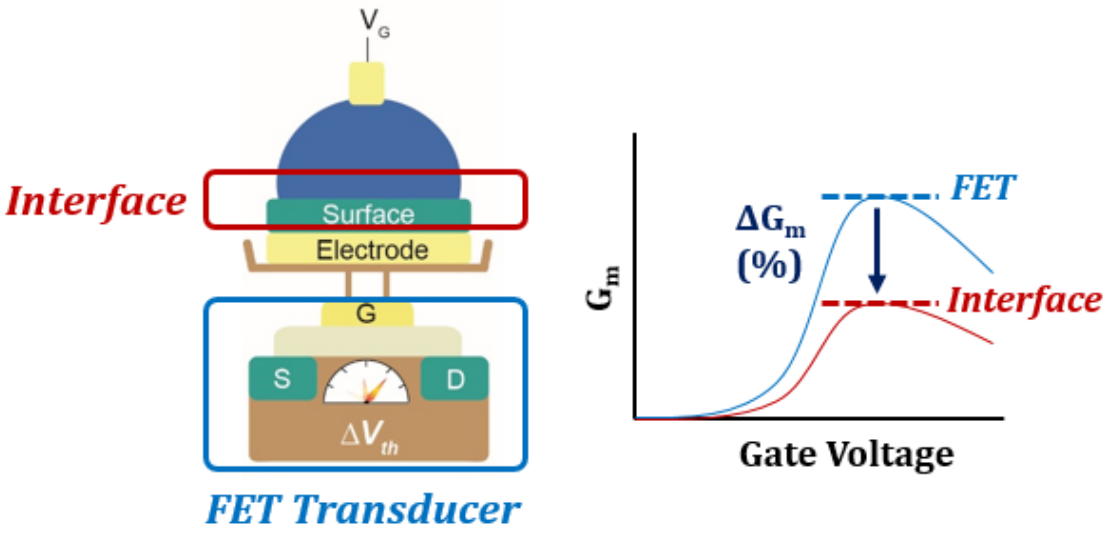

Figure 3.4. Schematic image of ΔG_m by having an additional interface on RG surface.

Systematic studies in drift and hysteresis were performed by alternating magnitudes of surface charges and dipole moments of solutions in solution/RG systems. Electrical properties of RG surfaces are varied by having ITO, SiO_2, HMDS, PS, and PSAA copolymer (60% PS) surfaces. Different dipole moments were applied on each RG surface through the incorporation of varying solutions such as an aqueous media at pH7 and organic solvent such as ACN, respectively.

We discovered that a slow process of dipole rearrangement on the interface plays a major role to provoke the electronic drift. Hysteresis stems from the slow, unsaturated, dipole arrangement. Hydrophobic components interacting with dipoles produce severe drift, hysteresis, and reduction of G_m. In PSAA, undesirable hydration on the hydrophobic PS backbone screens the carboxylic acids units for proton conduction as evidenced by a limited pH response of 5.4 mV/pH in a range from pH7 to pH11. This result led us to consider doped, charged backbones. Conductive, charged components on the surface were found to allow fast quasi-equilibrium under EF which leads to insignificant drift/hysteresis in aqueous solutions.

Accordingly, we investigated the electrochemical interface of conjugated polymers that meet the aforementioned criterion such as P3HT by using P3HT as a sensing surface on an RG module. The positively charged P3HT surface shows much less drift and hysteresis in aqueous solution. Based on this observation, we propose carboxylic acid-functionalized P3HT (poly [3-(3-carboxypropyl) thiophene-2,5-diyl] (PT-COOH)) as a high quality sensing layer with even stronger stability and reliability. The drift of PT-COOH is almost comparable with that of an inorganic counterpart such as ITO. Our RG system evaluates pH sensitivity of P3HT (17 mV/pH, ranging from pH3 to pH11) which is

intrinsically provoked by proton doping into P3HT. PT-COOH, with more stable electrochemical interfaces from the polar COOH groups in an already charged environment, produces even higher pH response (30 mV/pH, ranging from pH3 to pH7) compared to that of the more hydrophobic PSAA.

3.2. Experimental section

3.2.1. Sample preparation

The same sized SiO_2/Si substrates with 300 nm thickness of oxide are created and pretreated before deposition of varying surface material to be analyzed. A standard RCA cleaning process is applied in order to remove any contamination on the SiO_2 surface. HMDS is deposited on the SiO_2 substrate via vacuum baking at 120 °C for 2 hours and then the samples are sonicated for 15 min in hexane and followed by IPA. A solution of 35 mg/ml of PS is prepared by dissolving the polymer in chloroform. PS is spin-coated on the SiO_2 substrate at 1500 RPM for 1 min. PS/SiO_2 RG is baked at 120 °C for 2 hours for solvent outgassing. PSAA solution is prepared at concentration of 10 mg/ml in tetrahydrofuran and is spin coated on the SiO_2 substrate at 1500 RPM for 1 min. PSAA/SiO_2 RG is baked at 80 °C for 2 hours. A concentration of 10 mg/ml of P3HT (Solaris, SOL4106) and PT-COOH are prepared by dissolving each polymer in chlorobenzene and dimethylformamide, respectively. The prepared solutions are then sonicated for 1 hour and heated at 60 °C overnight for polymer to be fully dissolved while the PT-COOH requires the temperature to be raised to 115°C for 20 minutes. P3HT and PT-COOH are then spin coated on SiO_2/Si under 1600 RPM for 1 min and 1600 RPM for 5 min, respectively. PSAA/SiO_2 RG is baked at 80 °C for 2 hours. All concentrated

solutions are filtered using a hydrophobic PTFE or hydrophilic PTFE syringe filter before spin-coating method. ITO/PET (Sigma Aldrich, 639303) was sliced (1× 2 cm) for the RG and is cleaned with isopropanol for 20 min under ultrasonication, and rinsed with distilled water for 20 min.

The prepared RG Si substrate was electrically connected to the gate of a commercial Si-FET. Aqueous solution at defined pH or ACN was placed on each RG surface. An Ag/AgCl reference electrode was placed in the solution in order to apply the gate bias for all measurements. All transfer curves were measured by using a Keithley semiconductor analyzer with a drain voltage set at 50 mV and the gate voltage left at double sweep mode. pH sensitivity of each RG surface was evaluated by using standard pH buffer solution. Vth is calculated as the gate voltage corresponding to drain current of 1 μA in each transfer curve.

3.2.2. Definitions

We classify the electrical potential shifts of the solution/RG system with reference to V_{th} of the intrinsic Si-FET (1.5 V). That is, when V_{th} of the RGFET becomes higher than that of the original Si-FET, we state that the solution/RG system imposes the negative electrical potentials on the gate of the Si-FET (which is n-type, making it more difficult to turn on) and vice versa. The drift voltage (ΔV_{dri}) is calculated as the difference between the V_{th0} and the saturated $V_{th,RG}$ (V_{sat}) of the experimental condition. V_{th0} of the RGFET before drifting behavior is an indication of the initial surface potential of each RG material in each solution. Hysteresis voltage (ΔV_{hys}) is calculated as a difference in $V_{th,RG}$ between forward and reverse scanning during a double sweeping mode.

3.3. Results and Discussion

3.3.1. Conductive inorganic surface ITO

ITO is a material well known to show relatively ideal behavior in aqueous solution.[65] Drift and hysteresis of the ITO surface are evaluated in both ACN and pH7 aqueous solution. Figure 3.5 shows representative transfer curves of the RGFET with ITO RG measured in (a) ACN and (b) pH7. The measurements of transfer curves are repeated for 30 cycles in ACN and 100 cycles in pH7 solution by using a double sweep mode at the gate voltage ranging from 0 to 5 V. Each G_m level is calculated from all transfer curves. Repeating transfer curves and G_m curves show no significant or observable changes in the curves in Figure 3.5a and 3.5b.

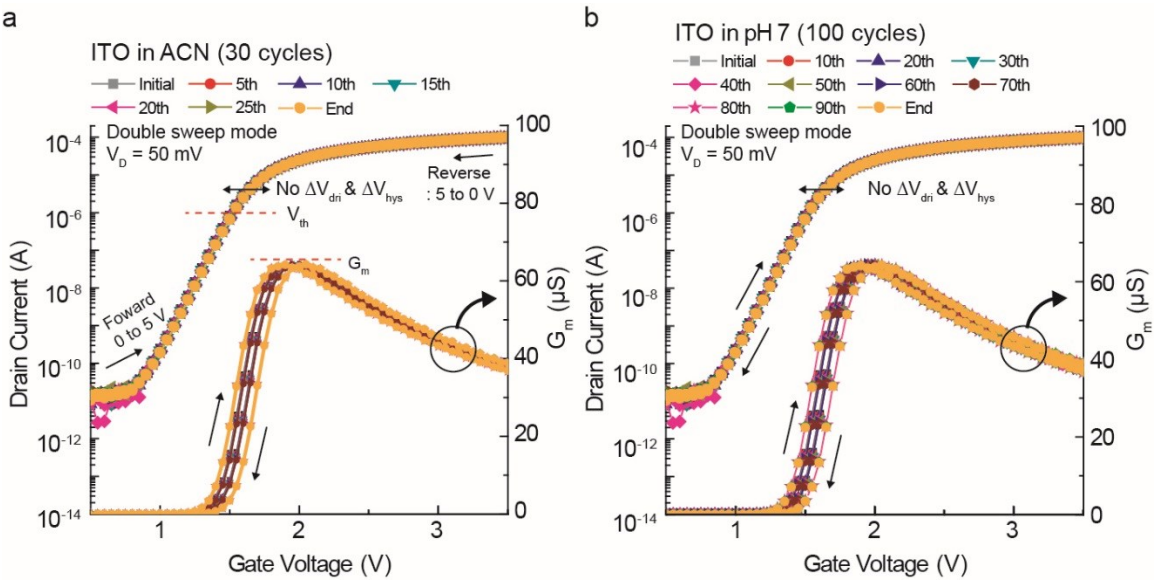

Figure 3.5. Zoomed-in representative transfer curves of ITO RGFET with a double sweep mode at the V_G ranges from 0 to 5 V measured in (a) ACN and (b) pH7.

Figure 3.6 presents $V_{th,RG}$ and G_m distributions of ITO RG in ACN and pH7 over the time of repeated cycling. $V_{th,RG}$ and G_m are measured by forward and reverse sweeping mode. ITO RG shows no observable changes in each $V_{th,RG}$ and G_m for ACN and pH7 water. Also, $V_{th,RG}$ and G_m have no gate voltage dependency as was a case of Si-FET. As the isoelectric point (pI) of ITO is 6, the ITO surface becomes only slightly negative charged with exposure to pH7 which is shown in the increased V_{th0} in pH7 (1.54 V) compared to V_{th} of Si-FET (1.5 V).

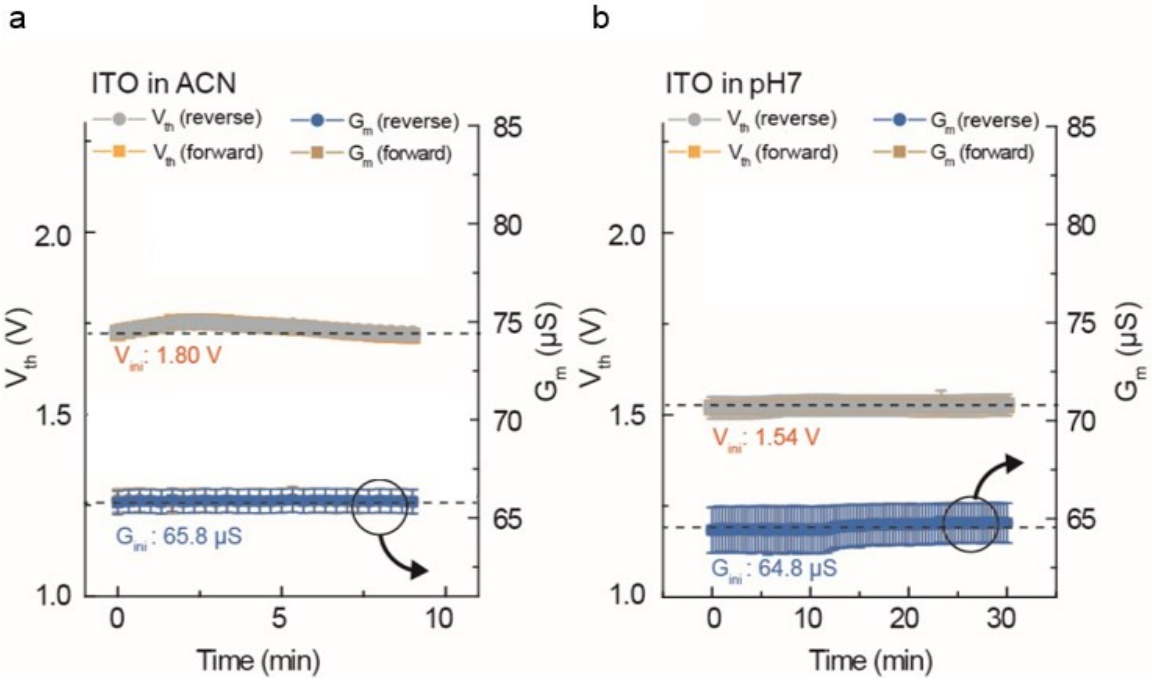

Figure 3.6. $V_{th,RG}$ and G_m distributions measured by forward/reverse sweeps over 10 and 6 samples from the ITO RG in (a) ACN and (b) pH7, respectively.

Initial G_m (G_{m0}) levels of 65.8 μS in ACN and 64.8 μS in pH7 are almost comparable to that of the original Si-FET (66 μS). That is, G_{m0} of ITO RG decreases only by 0.3% in ACN and 1.8% in pH7 with respect to G_m of the Si-FET. This means that ITO surfaces in both ACN and pH7 achieve highly stable interface states.

The ITO surface reversibly interacts with aqueous media by responding to proton concentrations in pH solutions in a way that has been descibed as a site-binding model.[66] Figure 3.7 shows response of representative transfer curves for proton cocentrations from ITO surfaces.

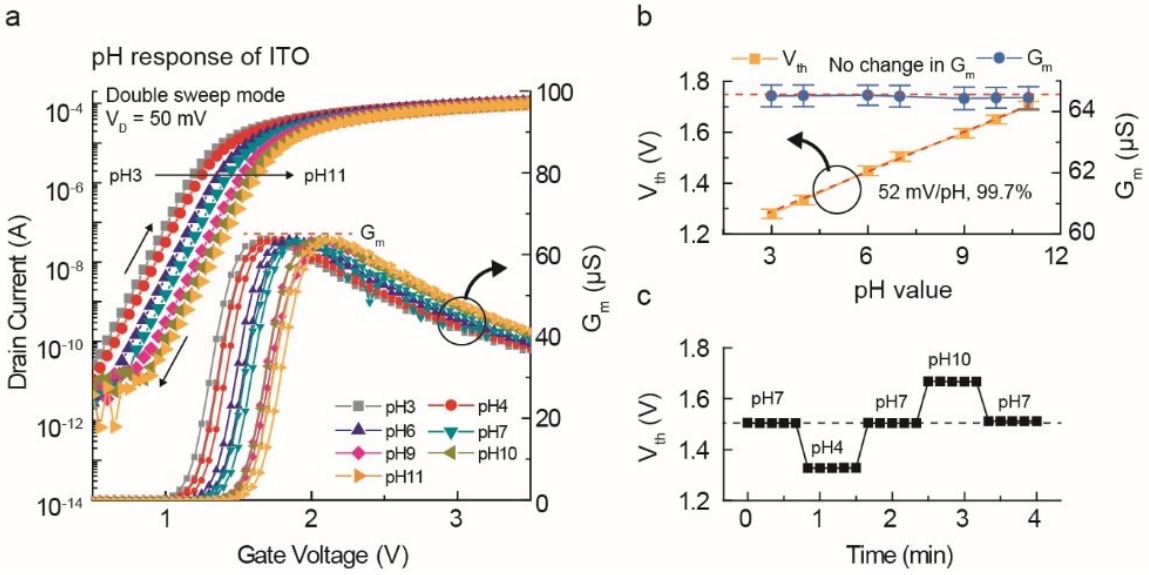

Figure 3.7. (a) Zoomed-in representative pH response of transfer curves from the ITO RG measured with the double sweep mode at the V_G range from 0 to 5 V. (b) $V_{th,RG}$ and G_m distributions of ITO RG over 6 samples in terms of pH value. (c) $V_{th,RG}$ response via a pH loop of pH7-pH4-pH7-pH10-pH7 showing high reversibility of pH sensing response.

Transfer curves reveal a linear $V_{th,RG}$ shifting as a function of pH values without changing the shape of the transfer curves or G_m in a double sweeping mode. High proton concentrations increases surface potential (φ_s), which leads to reduction of $V_{th,RG}$. The pH sensitivity is estimated to be 52 mV/pH with the linearity of 99.7% as shown in Figure 3.7b. At the same time, there is no change in G_m levels while $V_{th,RG}$ levels are changed by changing pH values. Also, a specific $V_{th,RG}$ level is determined for each pH value by the ITO surface showing high reversibility of pH response of ITO as shown in Figure 3.7c.

3.3.2 Conventional non-conductive surfaces in water

In order to understand the general properties of drift and hysteresis, conventional non-conductive surfaces of SiO_2, HMDS, PS, and PSAA are investigated first as shown in Figure 3.8.

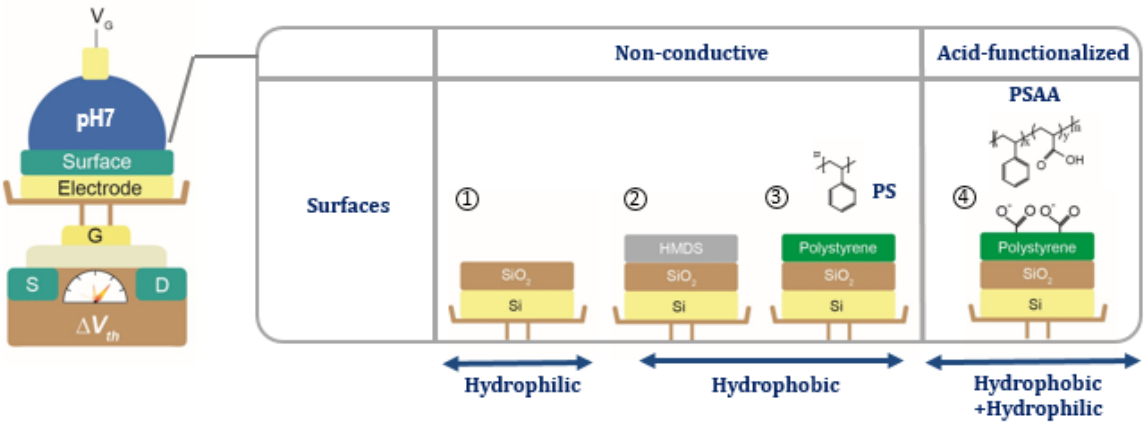

Figure 3.8. Schematic image of the RGFET system for characterization of the solution interface. Different types of non-conductive RG surfaces are prepared: 1. Pure SiO_2; 2. HMDS/SiO_2; 3. PS/SiO_2; 4. PSAA/SiO_2.

The SiO_2 surface specifically contains a mechanistic contributor to drift from slow hydration of buried hydroxyl sites underneath SiO_2 surfaces.[39,55] The negatively charged surface (pI: 2) of SiO_2 made favorable contact with water. The hydrophobic surfaces of HMDS of PS should have zero ionic charge. PSAA (60% PS) incorporates a hydrophobic backbone of PS and ionizable carboxylic acid groups.

Figure 3.9 presents representative transfer curves from non-conductive RG surfaces of SiO_2, HMDS/SiO_2, PS/SiO_2, and PSAA/SiO_2 in a pH 7 solution measured for 100 cycles under double sweeping mode. The transfer curves in Figure 3.9 are selected at measurements every ten times during 100 cycles. All RG surfaces shift transfer curves of the n-type FET transducer to the rightward direction during drift without changes in the shape of transfer curves. This indicates that drift provokes mostly changes in electrochemical potentials on the RG system. Also, each transfer curve measured by the forward sweeping mode is further moved to the right during the measurements at the reverse sweeping mode, designating the difference as hysteresis in transfer curves. This hysteresis is associated with interactions between solution and electrical properties of the surface.

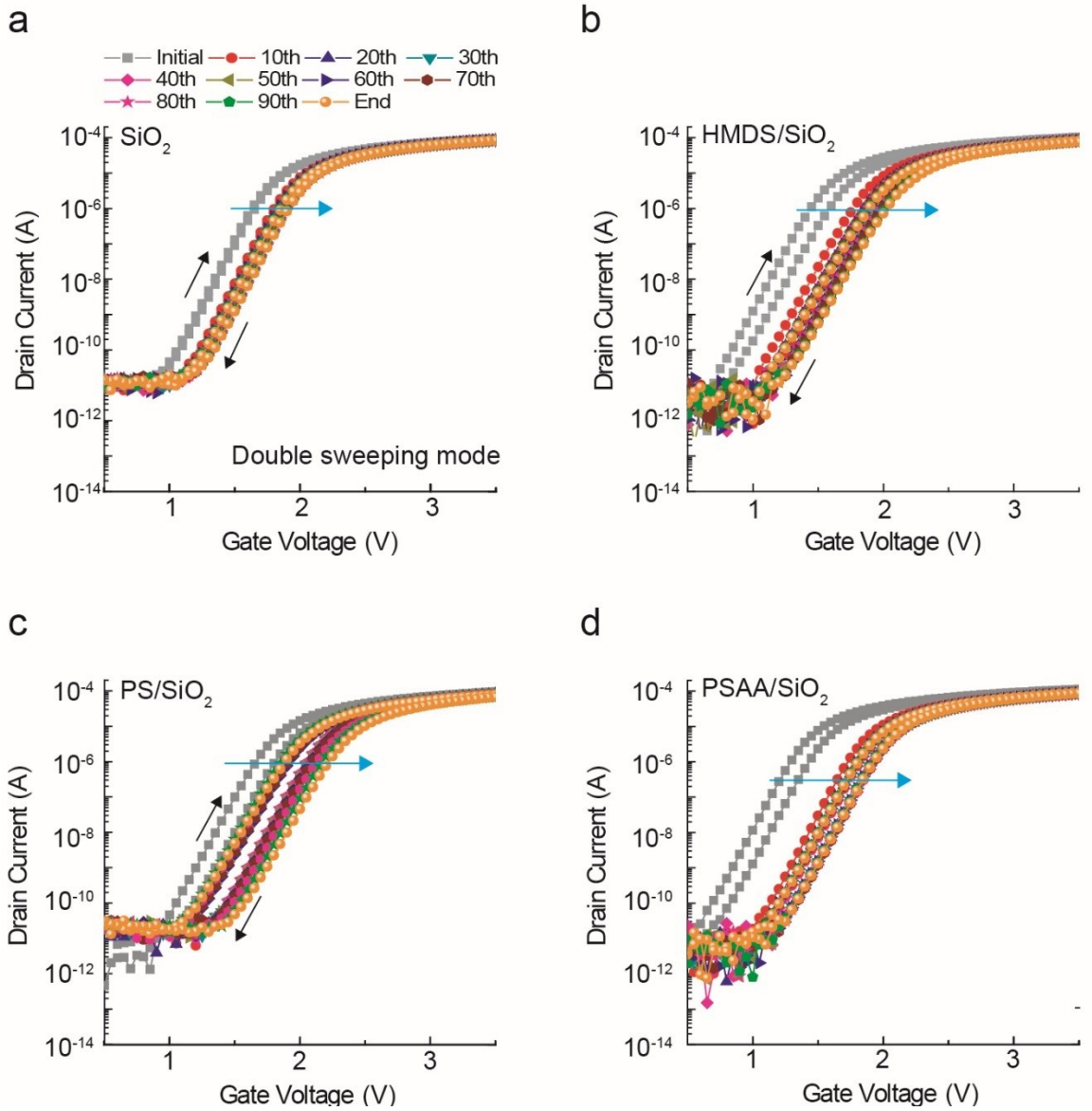

Figure 3.9. (a) Zoomed-in representative transfer curves of (a) SiO_2, (b) $HMDS/SiO_2$, (c) PS/SiO_2, and (d) $PSAA/SiO_2$ in a pH 7 solution at the V_G ranges from 0 to 5 V measured for 100 cycles under double sweeping mode.

Figure 3.10 shows drift curves in $V_{th,RG}$ from (a) SiO_2, (b) HMDS, (c) PS, and (d) PSAA that only consider $V_{th,RG}$ measured by the forward sweeping mode from transfer

curves in Figure 3.9. $V_{th,RG}$ is calculated as the gate voltage in transfer curves that corresponds to drain current of 1 μA. At the first cycle of drift measurements, transfer curves are repeated for 100 cycles at forward sweeping mode. After a 30-second break, the same measurements are further repeated during 30 cycles at following second cycle of drift. One distinguishable common feature is the increased $V_{th,RG}$ during the drift, regardless of electrical properties of RG surfaces. This means that all solution interfaces at RG surfaces impose positive electrochemical potentials on the gate of the n-type FET transducer during drift.

Also, the drifted $V_{th,RG}$ is saturated at a similar level of $V_{th,RG}$ after repeated measurement cycles of transfer curves at the V_G range from 0 V to 5 V for at least 4 min except for the PS layer. This certain amount of saturation time indicates that dipoles are slowly accumulated by the gate voltage on each surface, which is applied constantly but at varying magnitudes during the four minutes (and afterwards). $V_{th,RG}$ at saturation is defined as V_{sat} which is 1.86 V for SiO_2, 1.83 V for HMDS, 1.84 V for PS, 1.8 V for PSAA. This indicates a similar net interfacial potential from combined contributions of the material boundaries and dipole orientations. Each saturated $V_{th,RG}$, however, goes back to their V_{th0} when gate voltage cycles are concluded even for 30 sec, as shown on the right sides of each drift curve in Figure 3.10. This indicates that dipoles are temporarily anchored at the interface only as a result of applied electric fields.

Such behavior in turns brings into questions why water dipoles are not fully released at a zero voltage which is applied at the start of each gate voltage sweep, but instead remain oriented to continue contributing to continuous drift over many cycles. It should therefore be pointed out that at the start of each sweep, the near-zero voltage

application only lasts for ca. 0.75 sec out of the 7.5 seconds taken per sweep. The response of dipoles to gate voltage would be slower than that of this 0.75 seconds near-zero V interval time.

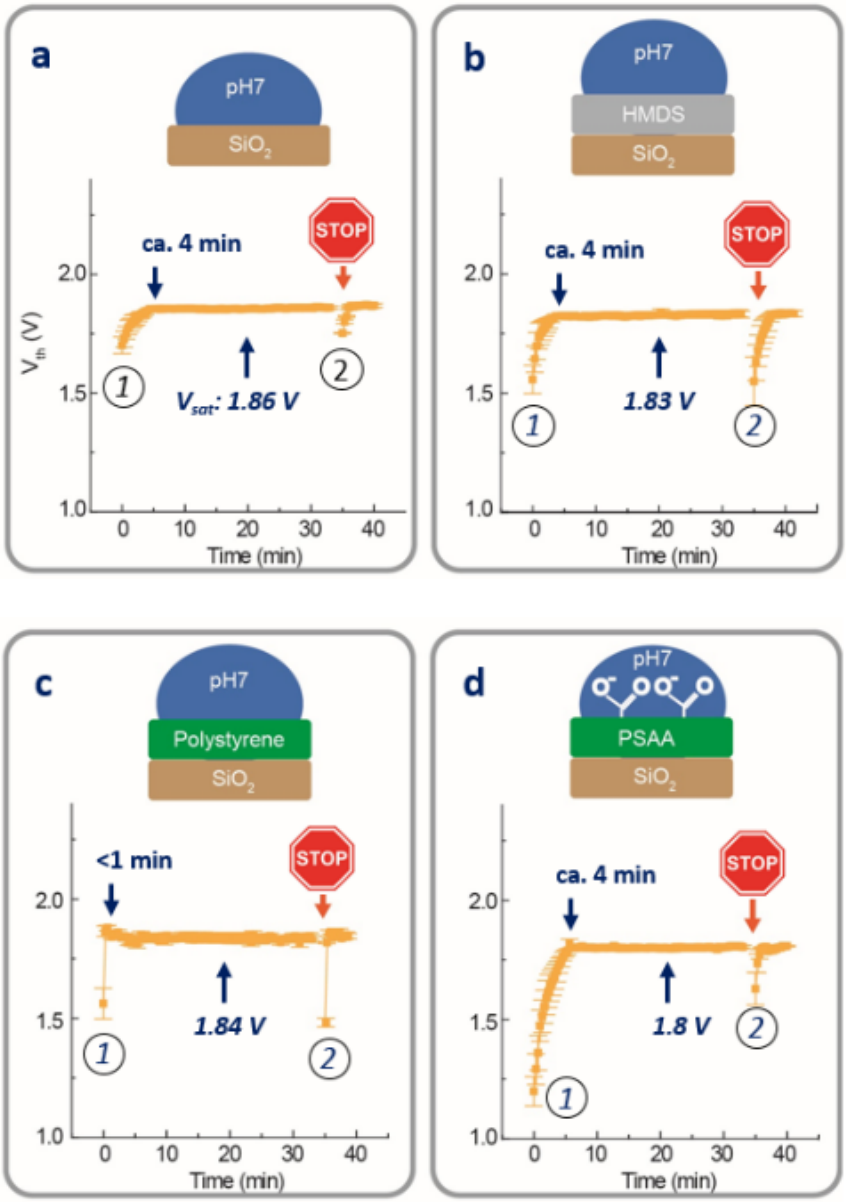

Figure 3.10. $V_{th,RG}$ distributions over 6 samples in pH7 with the RG of (a) SiO_2, (b) $HMDS/SiO_2$, (c) PS/SiO_2, and (d) $PSAA/SiO_2$ over time.

Detailed interactions of water dipoles on hydrophobic surfaces remain an enigma, while it has often been controversial which interactions are dominant between hydrophobic surface and polarized dipoles of water. One expectation is that hydrophobic surfaces should not promote the orientational ordering of dipoles. However, a large drift of 280 mV for both PS and HMDS interfaces shown here possibly reflects enforcements of orientational ordering on hydrophobic surfaces assisted by the applied electric fields[63,64].

Interestingly, PS shows a unique drift curve with quickest saturation time (< 1 min). Such an unexpected result could be related to an MD simulation recently reported to describe water dipoles on hydrophobic surface[63]. The electrostatic attraction in water is strengthened near the hydrophobic surface. This is because hydrophobic surfaces disturb hydrogen bond networks of water molecules and reduce near-surface dipole correlations, which results in faster orientations of dipoles on hydrophobic surfaces compared to that of hydrophilic surfaces. However, HMDS shows slow saturation. It is noted that the electrochemical properties of very thin HMDS layer can be affected by those of SiO_2 underneath HMDS because of penetration of solutions or ions through the thin HMDS layer (< 5 nm). More experimental evidence will be required to varify our hypothesis in our future work.

Figure 3.11 presents V_{th0} of SiO_2, HMDS, PS, and PSAA before drift. In the previous chapter 1.2.1, we demonstrated that V_{th0} is a parameter that only reflects initial interfacial potential of the surface without the influence of electrochemical drift. On the other hand, the V_{sat} of each RG surface is final interfacial potential after drift affected by dipole orientations at quasi-equilibrium, respectively. A high V_{th0} of 1.7 V from SiO_2 is attributed to the initial negative charge of the existing SiO_2 surface in pH7. V_{th0} of PS (1.55

V) and HMDS (1.56 V) with theoretically zero ionic charge is close to V_{th} of the Si-FET (1.5 V). Despite a difference in thicknesses of films (Me_3Si from HMDS: < 5 nm, PS: ca. 100 nm), V_{th0} presents insignificant differences between two RGs, indicating that the RGFET mostly indicates the interface potentials. For PSAA surface, V_{th0} first includes the initial stabilization and equilibrium process of carboxylic acids to the pH of the solution. V_{th0} of 1.62 V of PSAA at the second cycle, regarded as the representative value for PSAA, showed a more negatively charged surface compared to that of PS (1.55 V), due to the contribution of the negative charge of COO- groups.

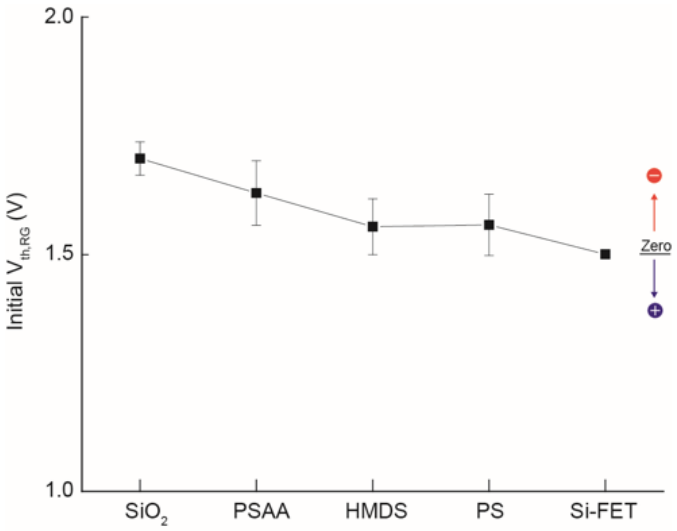

Figure 3.11. V_{th0} distributions of SiO_2, HMDS/SiO_2, PS/SiO_2, and PSAA/SiO_2 before drift over at lesat 6 samples in pH7.

ΔV_{dri} levels calculated as a difference between each V_{sat} and V_{th0} are normalized with respect to each V_{th0} in Figure 3.12. Slowly hydrating sites on SiO_2 surface provokes

a large ΔV_{dri} of 160 mV, which is about 8% change with respect to V_{th0} of SiO_2. Both hydrophobic surfaces of HMDS and PS reveal even larger ΔV_{dri} of 280 mV that is about 17% increase with respect to each V_{th0}. There should be a hydrophobic effect that excludes water molecules at the hydrophobic surfaces. However, external applications of electric fields to the RG system would enforce orientational ordering as the electric property of the hydrophobic surface plays a secondary role. This possibly leads to the large amount of ΔV_{dri} in hydrophobic surfaces in Figure 3.12.

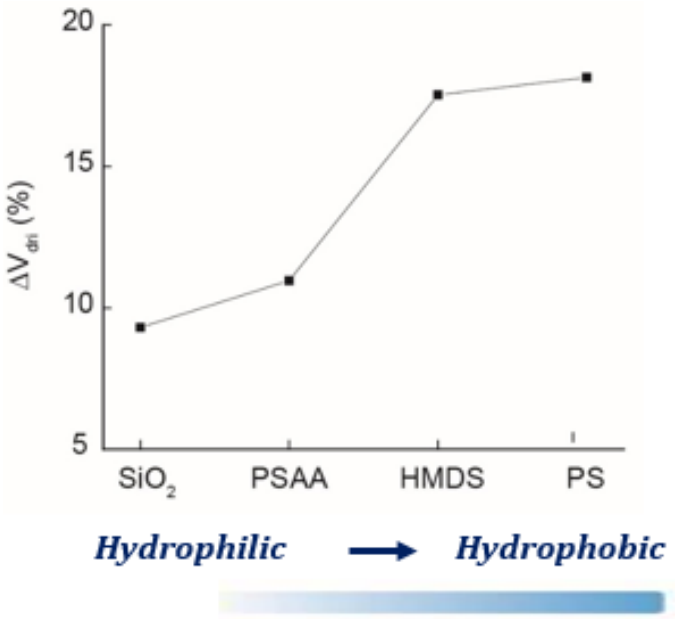

Figure 3.12. Average ΔV_{dri} normalized to each V_{th0} over at lesat 6 samples of RGs with SiO_2, HMDS/SiO_2, PS/SiO_2, and PSAA/SiO_2 in pH7.

For PSAA surface, ΔV_{dri} of 600 mV in Figure 3.10d shown at the first cycle of drift in turn reduces to 180 mV at the second cycle of drift. The first drift behavior possibly

included the initial stabilization and equilibrium process of carboxylic acids to the pH of the solution. The second cycle of drift is regarded as a representative drift property of PSAA which is about 11% increase with respective to V_{th0} of PSAA. As a result, the surfaces including hydrophilic components suppress the electrical drift.

Figure 3.13 presents repesentative G_m curves from non-conductive RG surfaces of SiO_2, HMDS/SiO_2, PS/SiO_2, and PSAA/SiO_2 in a pH 7 solution for 100 cycles under double sweeping mode. The G_m curves in Figure 3.13 are selected at measurements every ten times during 100 cycles. All RG surfaces shifts G_m curves to the right over which corresponds to shifts in $V_{th,RG}$ in Figure 3.10. Also, for some of RG surface, each G_m measured by the forward sweeping mode is further moved to the right during the measurements at the reverse sweeping mode. This indicate there is hysteresis in G_m (G_{hys}) along with V_{hys}.

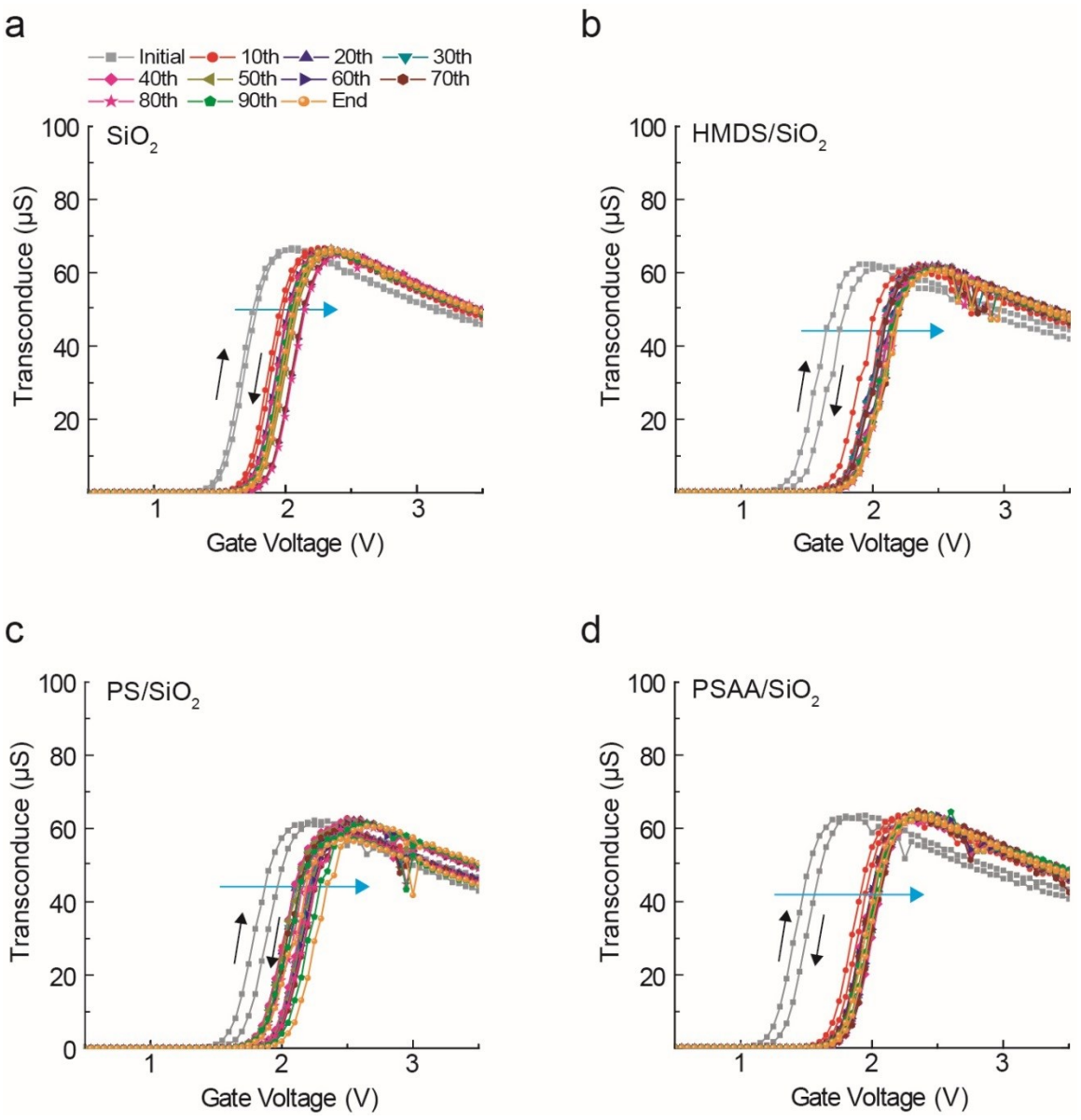

Figure 3.13. (a) Zoomed-in representative transfer curves of (a) SiO_2, (b) $HMDS/SiO_2$, (c) PS/SiO_2, and (d) $PSAA/SiO_2$ in the pH 7 solution at the V_G ranges from 0 to 5 V measured for 100 cycles under the double sweeping mode.

Figure 3.14 shows the comparision of G_{m0} levels from (a) SiO_2, (b) $HMDS/SiO_2$, (c) PS/SiO_2, and (d) $PSAA/SiO_2$ in the pH 7 solution. G_{m0} of SiO_2, $HMDS/SiO_2$, PS/SiO_2, and $PSAA/SiO_2$ is 64.5 µS, 61.3 µS, 56.3 µS, and 61.1 µS, respectively. There is a clear propensity that hydrophobic surfaces decreases G_{m0} possibly because of hydrophobic effect. This is, the solution interface between hydrophobic surfaces and water at the gate delays the response of the gate for the applied gate voltages.

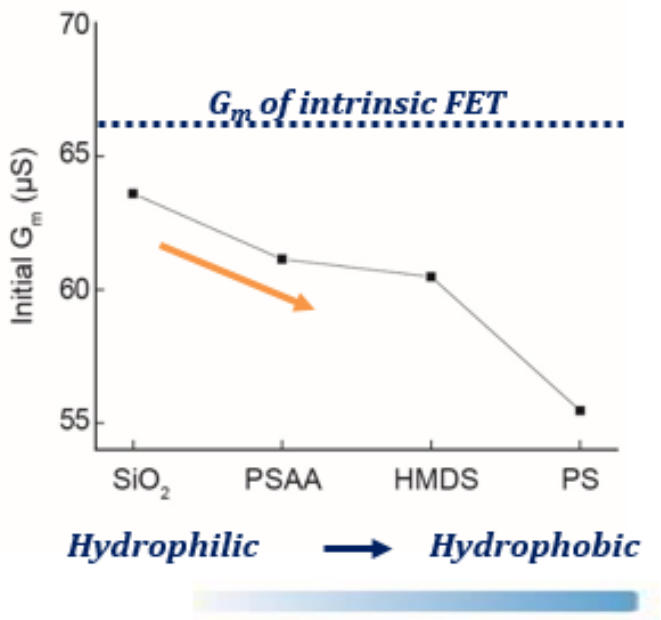

Figure 3.14. Average G_{m0} levels over at lesat 6 samples of RGs with SiO_2, $HMDS/SiO_2$, PS/SiO_2, and $PSAA/SiO_2$ in pH7.

Figure 3.15 presents drift in G_m levels of (a) SiO_2, (b) HMDS, (c) PS, and (d) PSAA. At the first cycle of drift in G_m, transfer curves are repeated for 100 cycles at forward sweeping mode.

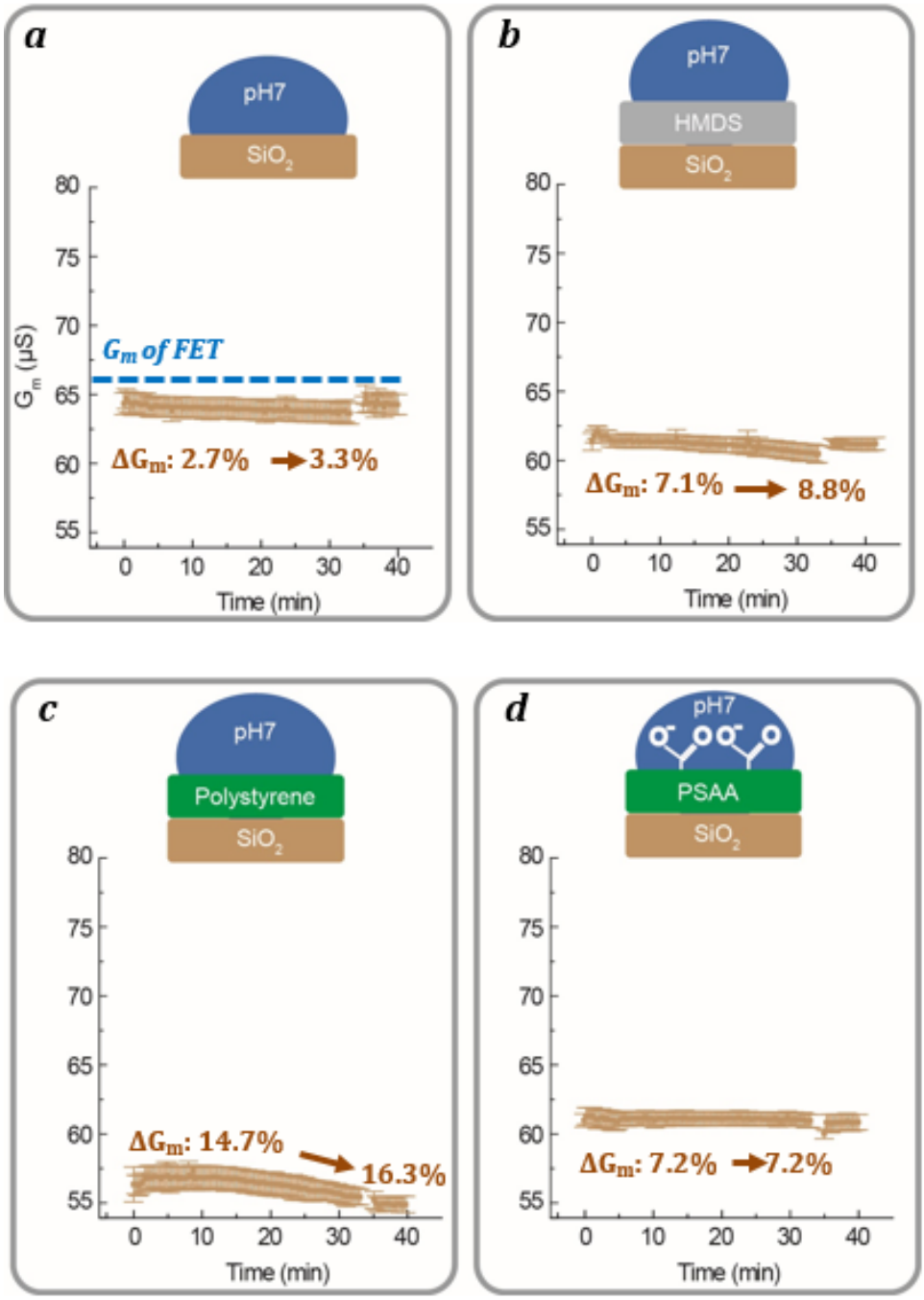

Figure 3.15. G_m distributions over at least 6 samples of RGs with (a) SiO_2, (b) $HMDS/SiO_2$, (c) PS/SiO_2, and (d) $PSAA/SiO_2$ over time.

After a 30-second break, the same measurements are further repeated during 30 cycles at following second cycle. G_{m0} of SiO_2 surface (64.5 μS) before drift is reduced by only 2.7%, compared to G_m of the Si-FET (Figure 3.15a). After drift, G_{m0} of SiO_2 further decreases to 3.3%. Obviously, hydrophobic surfaces enable a significant reduction of G_{m0} by 7.1% for HMDS and 14.7% for PS compared to G_m of the Si-FET (Figure 3.15b and 3.15c). Each G_{m0} of HMDS and PS further decreases to 8.8% for and 16.3% after drift, respectively. On the other hand, PSAA shows the increased G_{m0} of 61.1 μS compared to that of the PS (56.3 μS) but a smaller value than that of SiO_2 (64.5 μS) (Figure 3.15d). This is possibly because the hydrophobic effect on PSAA is alleviated by hydrophilic components of the carboxylic acid in PSAA. Furthermore, there is insignificant ΔG_{dri} in PSAA due to the advantages of the hydrophilic component.

Figure 3.16 shows a summary of the total reduction of G_m of SiO_2, HMDS, PS, and PSAA after drift. Likewise to the propensity in ΔV_{dri} shown in Figure 3.12, surfaces including hydrophobic components delay a response of the solution interface for the gate voltage bias. A 100-nm-thick PS layer would more represent general properties of hydrophobic surfaces than the very thin HMDS. As a result, hydrophobic surfaces impede orientational ordering of dipoles that is enforced by the applied electric fields because of hydrophobic effects, which results in large drift components in $V_{th,RG}$ and G_m.

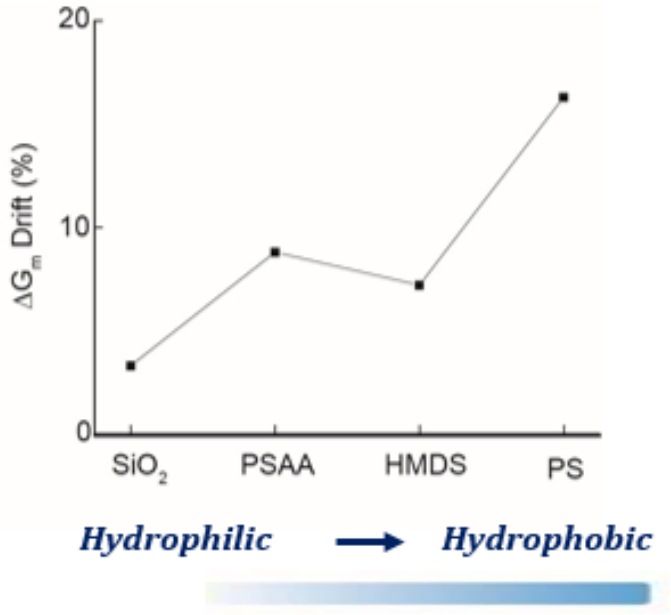

Figure 3.16. Average ΔG_{dri} levels over at lesat 6 samples of RGs with SiO_2, HMDS/SiO_2, PS/SiO_2, and PSAA/SiO_2 in pH7.

3.3.3. Hysteresis of conventional non-conductive surfaces in water

In the next section, we investigate the mechanism of hysteresis occurring during the double sweeping mode. In the previous section, we demonstrated a property of solution interfaces showing slow and delayed responses for the gate electric fields in case of hydrophobic surfaces. A hydrophobic surface delays orientations of dipoles at the interface by competing electric properties of hydrophobic surface and alignments induced by electric fields.

Slow orientations in turn could lead to voltage dependency of interface properties. Therefore, the initial state of the solution interface should be different between forward and reverse sweeping mode, affected by different initial electric fields from the gate. The reverse sweeps immediately start after the end of forward sweeps. That is, the initial state

for reverse sweeps include effects of orientational ordering that is achieved already during forward sweeping mode. The initial state of the interface at reverse sweeps results from a longer exposure time to positive electric fields compared to the forward sweeps.

Figure 3.17 shows the model for hysteresis related to slow response of dipoles at the interface. Possibly, additional dipoles would be accumulated at the process between step 3 and 4 as shown in snapshot 3 and 4 or there could be dipole-dipole interactions caused by dipoles already oriented by the forward sweeping mode. This makes different interface states in the same gate voltage as shown in in snapshot 2 and 4 in Figure 3.17, which leads to different $V_{th,RG}$ levels during double sweeping mode.

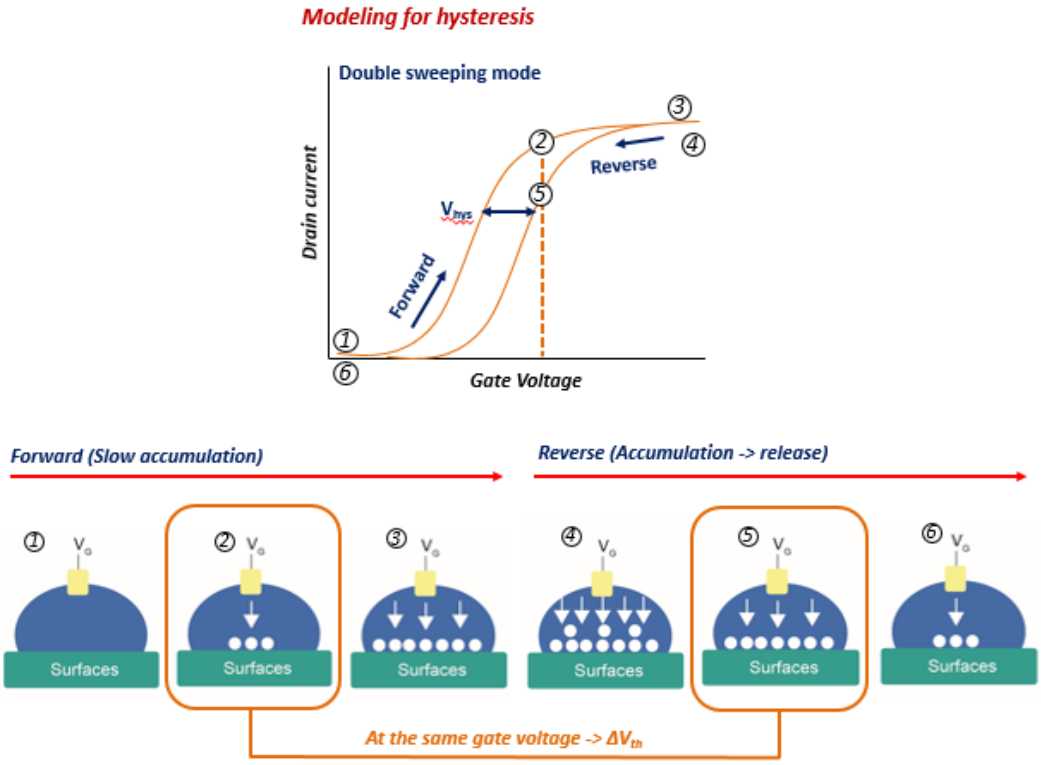

Figure 3.17. Modeling of hysteresis in a transfer curve of the RGFET resulting from solution-interfaces changed by the sweeping mode.

Figure 3.18 shows drift curves in $V_{th,RG}$ of (a) SiO_2, (b) HMDS, (c) PS, and (d) PSAA measured by both forward and reverse sweeping modes. $V_{th,RG}$ levels at reverse sweeps (gray-colored data over Figure 3.18) are always higher than those of forward sweeps by an amount we designate as ΔV_{hys}. Hydrophobic surfaces show higher ΔV_{hys} of HMDS (120 mV) and PS (450 mV) than those with the charged surfaces of SiO_2 (40 mV) and PSAA (100 mV). Also, there is reversibility of hysteresis showing high dependence on the gate voltage. That is, each amount of hysteresis at the first cycle of measurement is repeated at the second cycle.

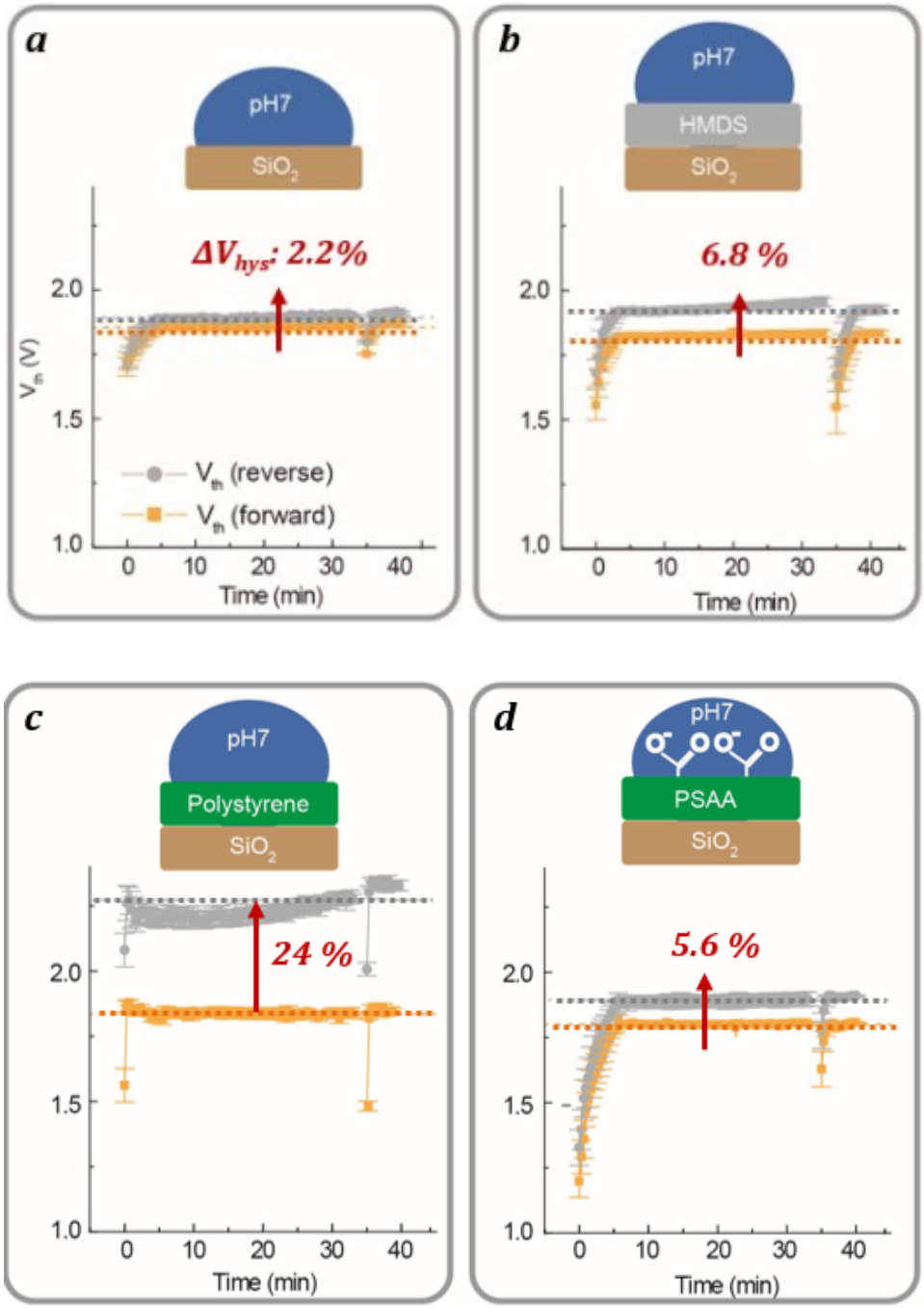

Figure 3.18. $V_{th,RG}$ distributions over at least 6 samples of RGs with (a) SiO_2, (b) HMDS, (c) PS, and (d) PSAA. $V_{th,RG}$ is measured by both forward and reverse sweeping modes.

$V_{th,RG}$ of SiO_2, HMDS, PS, and PSAA increases at the reverse sweeping mode by 2.2%, 6.8%, 24%, and 5.6 %, respectively, as shown in Figure 3.19. The most hydrophobic surface is associated with higher ΔV_{hys}. It is noted that 40% carboxylic acids in PSAA significantly reduces ΔV_{hys} compared to that of PS.

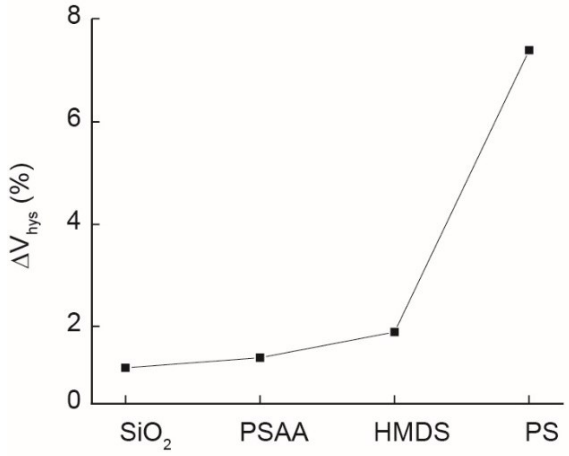

Figure 3.19. Average ΔV_{hys} levels over at least 6 samples of RGs with SiO_2, HMDS/SiO_2, PS/ SiO_2, and PSAA/ SiO_2 normalized to each $V_{th,RG}$ measured by the forward sweeping mode.

Figure 3.20 shows drift curves in G_m of SiO_2, HMDS, PS, and PSAA measured by both forward and reverse sweeping modes. Interestingly, G_m increases by 1.2%, 1.9%, 7.4%, 1.4% for SiO_2, for HMDS, PS, and PSAA at reverse sweeps, respectively, compared to each G_m at forward sweeps, probably due to more confinement of additional dipoles at the interface by longer exposure of interface to the positive potential during reverse sweeps. Therefore, the increase of G_m during reverse sweeping mode also infers slow response of solution interfaces.

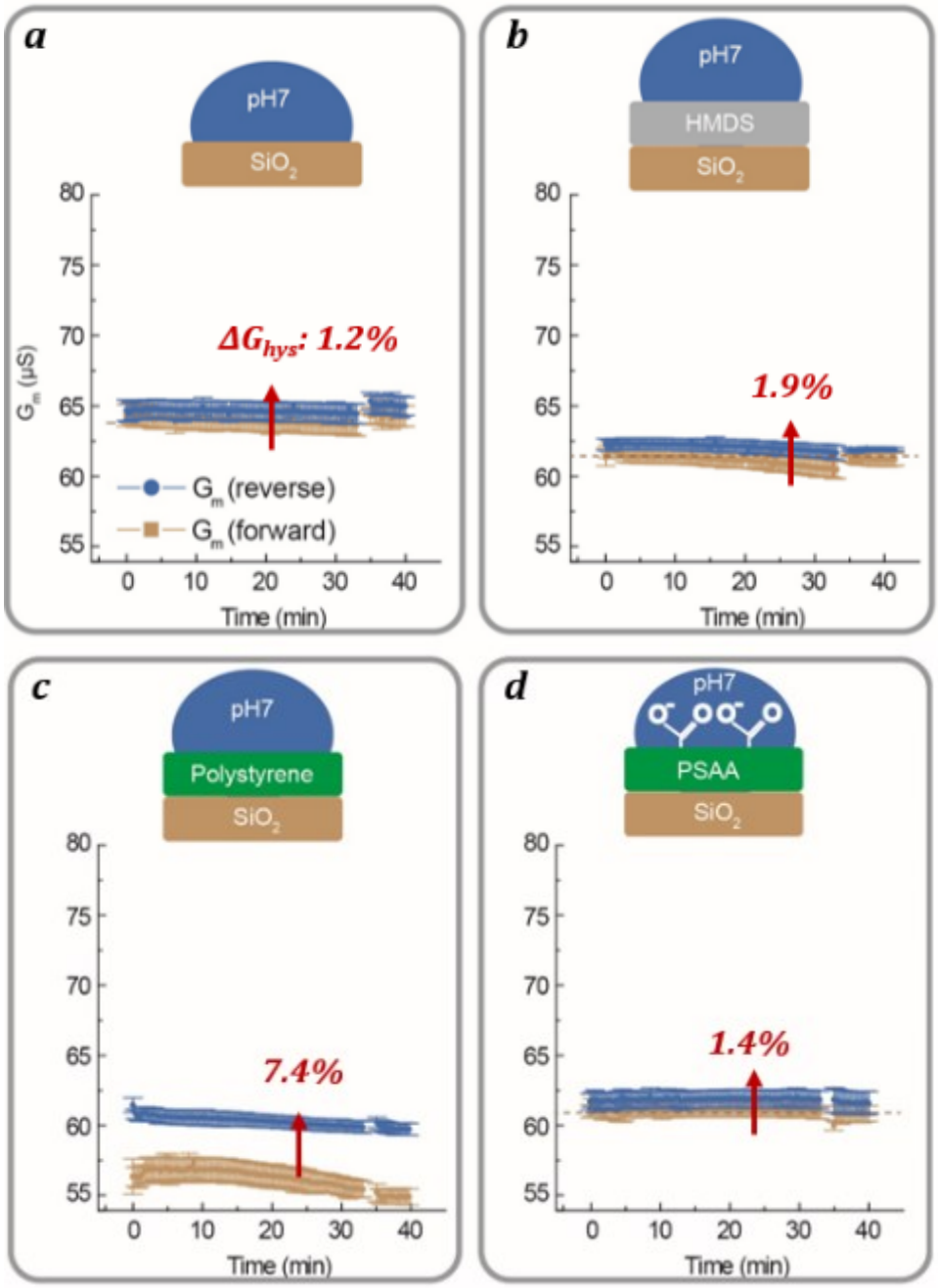

Figure 3.20. G_m distributions over at least 6 samples of RGs with (a) SiO_2, (b) $HMDS/SiO_2$, (c) PS/SiO_2, and (d) $PSAA/SiO_2$ over time. G_m is measured by both forward and reverse sweeping modes.

Figure 3.21 shows a summary of ΔG_{hys} of SiO_2, HMDS, PS, and PSAA. Interestingly, there is clear dependency between ΔG_{hys} in Figure 3.21 and ΔV_{hys} in Figure 3.19. That is, ΔV_{hys} and ΔG_{hys} which are developed at the same time are highly correlated.

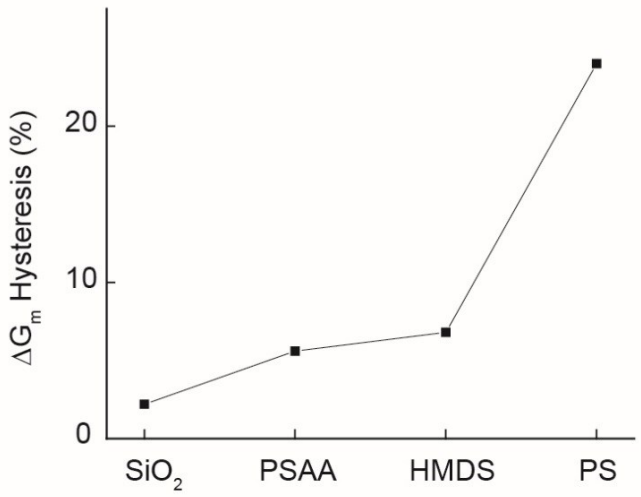

Figure 3.21. Average ΔG_{hys} over at least 6 samples of RGs with SiO_2, HMDS/ SiO_2, PS/ SiO_2, and PSAA/SiO_2 normalized to each G_m measured by the forward sweeping mode.

3.3.4. Conventional non-conductive surfaces in acetonitrile

To further elucidate the dependency between dipole moment and drift and hysteresis, the same measurements are applied for each surface RG above but switching to ACN including only 0.001% water as an impurity. The lower dipole moment of ACN infers less polarization, less orientation ordering, and less influence on surface electrical properties. Thus, the lower dipole moment of ACN infers less influence of ACN dipoles at the interface than pH7 aqueous solution. G_{m0} levels are always higher in ACN than in

water as shown in Figure 3.22, supporting our assumption regarding properties of ACN dipoles in the applied electric fields. Average G_{m0} levels of SiO_2, PSAA, HMDS, and PS are 65.6 µS, 62.7 µS, 63.7 µS, and 64.6 µS, respectively.

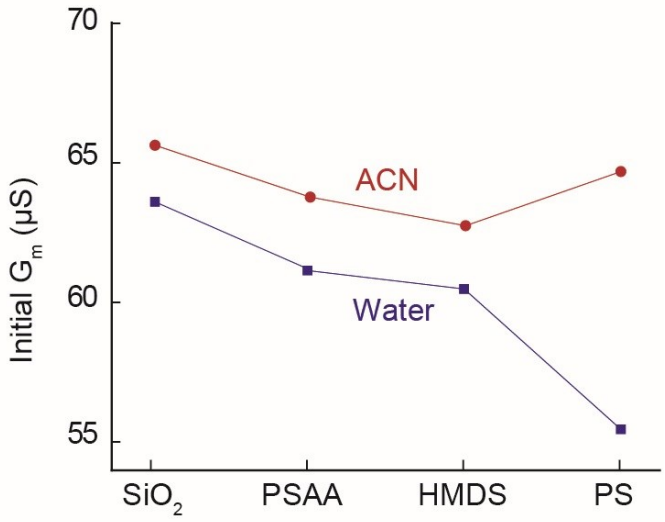

Figure 3.22. Comparison of average G_{m0} over at least 6 samples of RGs of SiO_2, HMDS/ SiO_2, PS/ SiO_2, and PSAA/SiO_2 in pH7 water and ACN.

Figure 3.23 shows drift and hysteresis in $V_{th,RG}$ curves from SiO_2 in (a) ACN and (b) pH7 solution. $V_{th,RG}$ is measured by both reverse and forward sweeps. The nature of the negative charged surface of SiO_2 in ACN in the literature[67] is characterized as a high V_{th0} of 1.78 V in our RGFET system. Interestingly, drift and hysteresis of SiO_2 shown in pH7 (ΔV_{dri}: 160 mV, ΔV_{hys}: 40 mV) became insignificant in ACN (ΔV_{dri}: 70 mV, ΔV_{hys}: 10 mV). This shows a critical role of dipole moments of solutions in electrochemical instability.

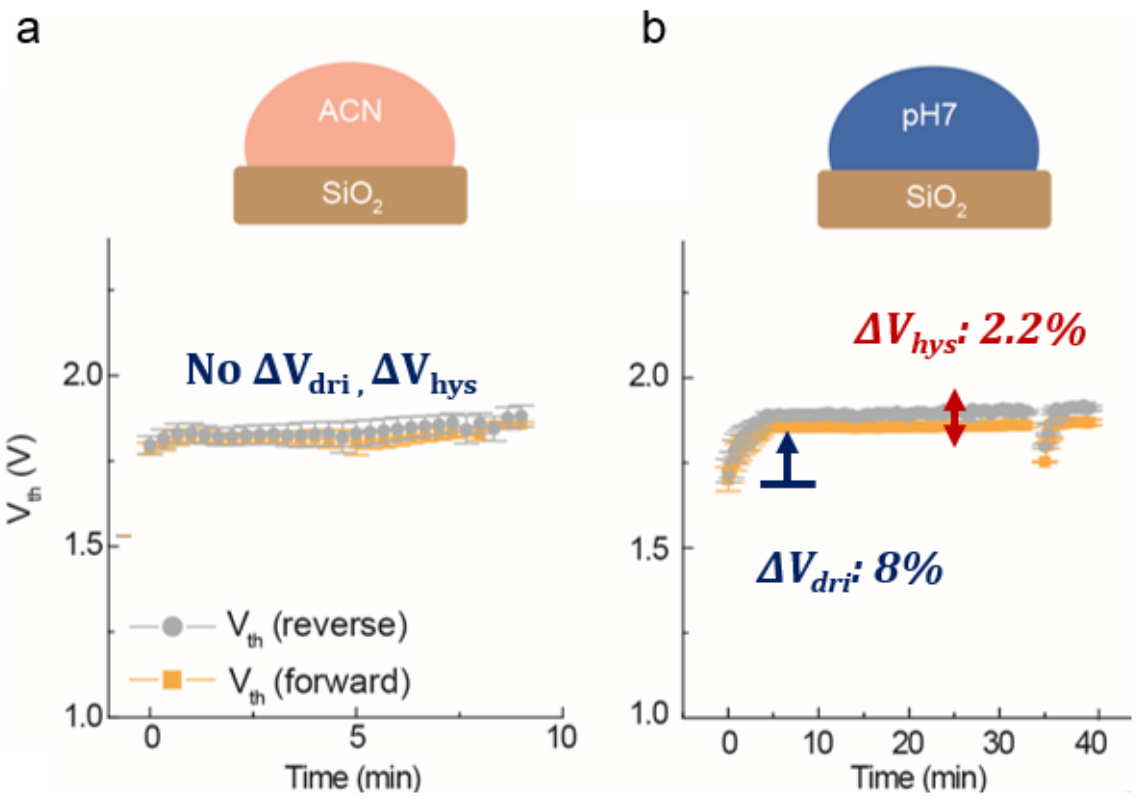

Figure 3.23. $V_{th,RG}$ distributions over at least 6 samples of RG with SiO_2 in (a) ACN and (b) pH7 water. $V_{th,RG}$ is measured by both forward and reverse sweeping modes.

Figure 3.24 presents drift and hysteresis in $V_{th,RG}$ curves of PSAA in (a) ACN and (b) pH7 solution. $V_{th,RG}$ is measured by both reverse and forward sweeps. The same propensity shown in the case of SiO_2 is observed in PSAA. Despite the previous severe instability of PSAA in pH7 (ΔV_{dri}: 180 mV, ΔV_{hys}: 100 mV), drift and hysteresis are highly reduced in ACN (ΔV_{dri}: 10 mV, ΔV_{hys}: 7 mV). Also, a large amount of $V_{th,RG}$ caused by initial stabilization of carboxylic acid in pH7 solution is not shown in ACN. 40%

carboxylic acids in PSAA offers enough charged surface to achieve spontaneous, favorable, fast arrangements of ACN dipoles on PSAA interfaces.

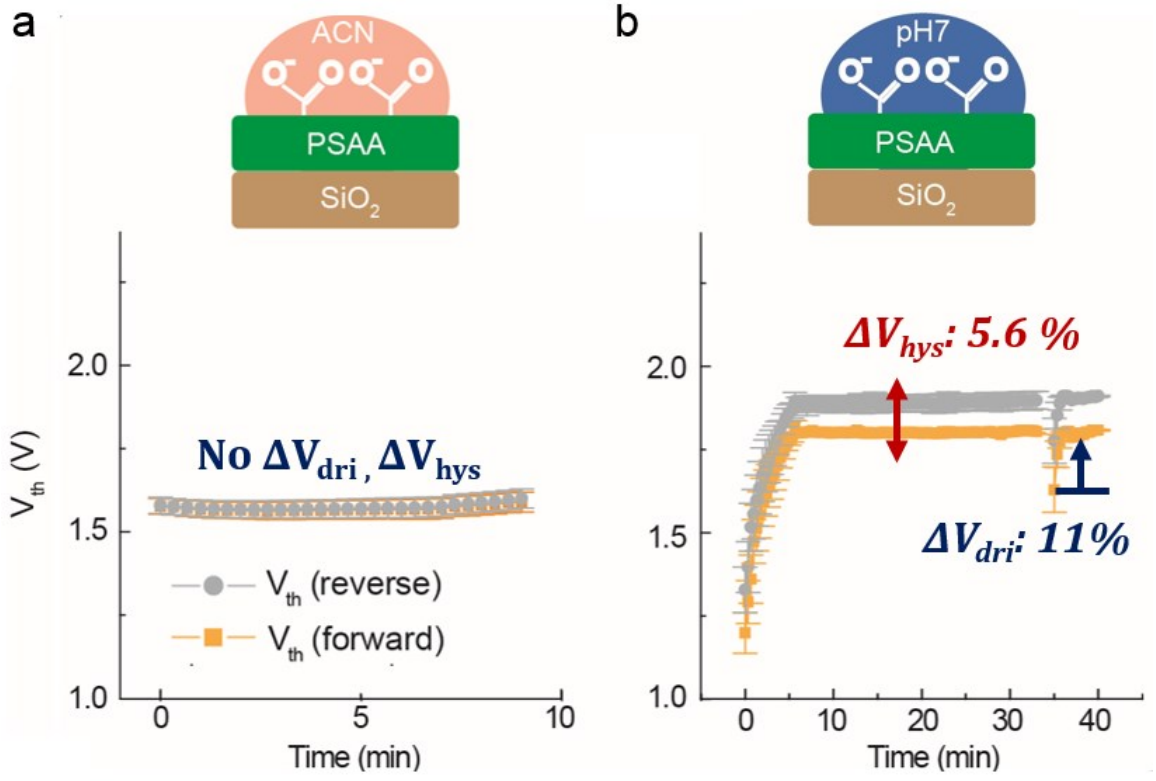

Figure 3.24. $V_{th,RG}$ distributions over at least 6 samples of RG with PSAA/SiO_2 in (a) ACN and (b) pH7 water. $V_{th,RG}$ is measured by both forward and reverse sweeping modes.

Figure 3.25 presents drift in $V_{th,RG}$ curves of PS in (a) ACN and (b) pH7 solution. $V_{th,RG}$ is measured by forward sweeps. Transfer curves are repeated for 30 cycles under the ACN solution two times by having a 30-seconds break in the middle. Unlike the cases of hydrophilic surfaces of SiO_2 and PSAA above, the hydrophobic PS surface shows severe

drift even in ACN. Also, drift curves in ACN have a tendency of reversibility (Figure 2.25a). More interestingly, V_{sat} of PS in ACN is similar to that in pH7 aqueous solution. Undesirable orientational ordering of both ACN and water dipoles makes a similar net interfacial potential on PS layer.

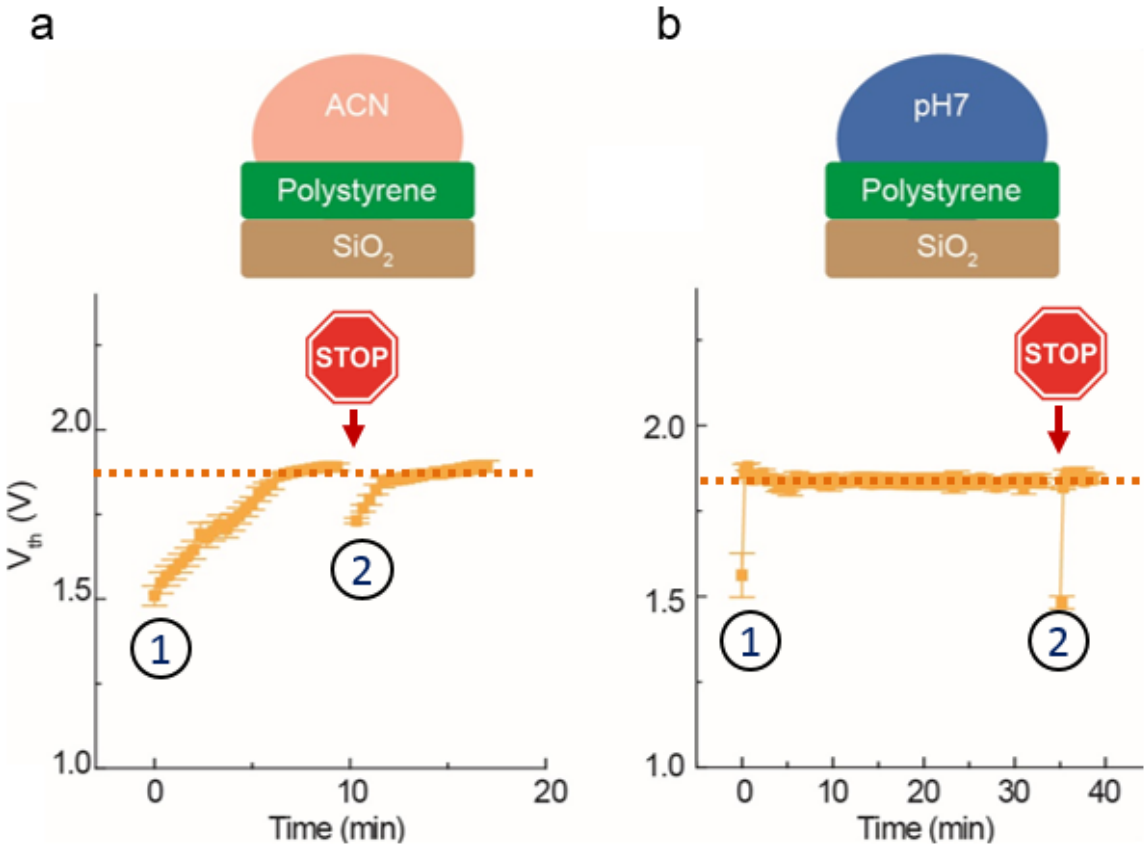

Figure 3.25. $V_{th,RG}$ distributions over at least 6 samples of RG with PS/SiO_2 in (a) ACN and (b) pH7 water.

Figure 3.25 presents drift in $V_{th,RG}$ curves of HMDS in (a) ACN and (b) pH7 solution. $V_{th,RG}$ is measured by forward sweeps. Transfer curves are repeated for 30 cycles

under the ACN solution two times by having 30 seconds break in the middle. The repeated two drift curves show high reversibility. V_{sat} of HMDS in ACN is similar to that in pH7. An interesting feature in the drift curve in ACN is that insignificant V_{dri} at initial and is enlarged up to V_{sat} (Figure 3.26a) under continuously repeating gate voltage. A similar net interfacial potential is observed after drift as a similar range in V_{sat} from all surfaces incorporating drift components in both ACN and pH7.

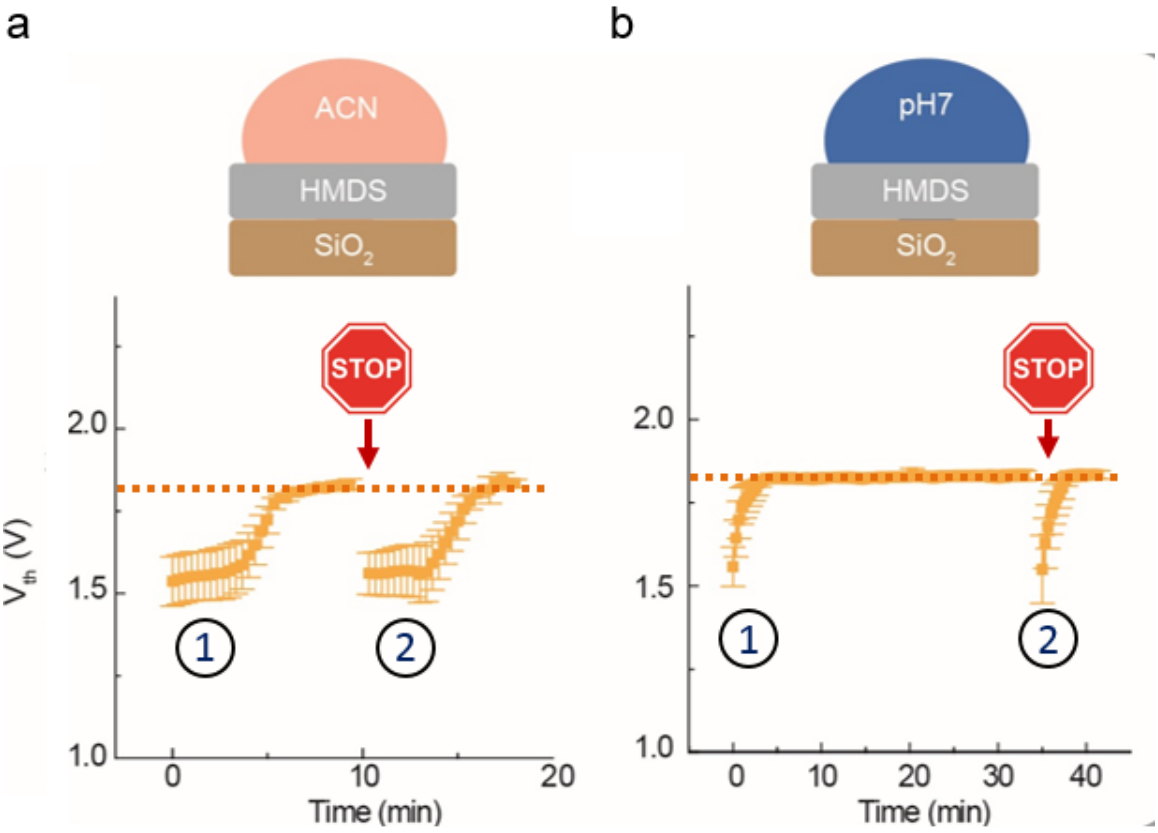

Figure 3.26. $V_{th,RG}$ distributions over at least 6 samples of RG with HMDS/SiO_2 in (a) ACN and (b) pH7 water.

Figure 3.27 presents $V_{th,RG}$ of HMDS measured by both forward and reverse sweeping mode in (a) ACN and (b) pH7 solution. An interesting feature in drift curves of PS is insignificant initial ΔV_{hys} but up to 60 mV for PS during drift (Figure 3.27a). Such a trend is more clearly shown for HMDS (Figure 3.27b) surface by showing a larger ΔV_{hys} of 200 mV after saturation. This showed again that ΔV_{hys} components possibly stem from the interactions between slow dipoles and an already oriented dipole layer at the interface.

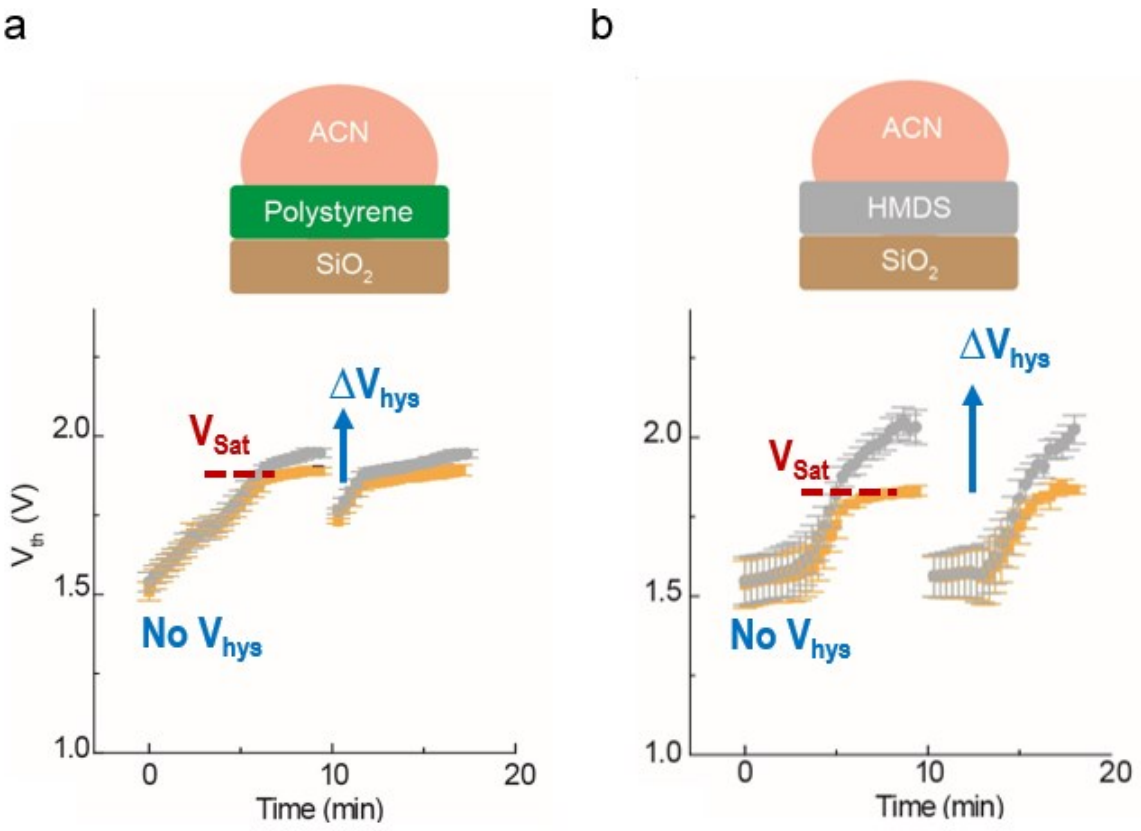

Figure 3.27. $V_{th,RG}$ distributions over at least 6 samples of RG with (a) PS/SiO_2 and (b) HMDS/SiO_2 in ACN. $V_{th,RG}$ is measured by both forward and reverse sweeping modes.

Figure 3.28 shows drift curves in $V_{th,RG}$ measured by forward sweeps from (a) SiO_2, (b) PSAA, (c) HMDS, and (d) PS in ACN. High G_{m0} levels of SiO_2 (65.6 μS) are only decreased by 0.6 % compared to G_m of Si-FET.

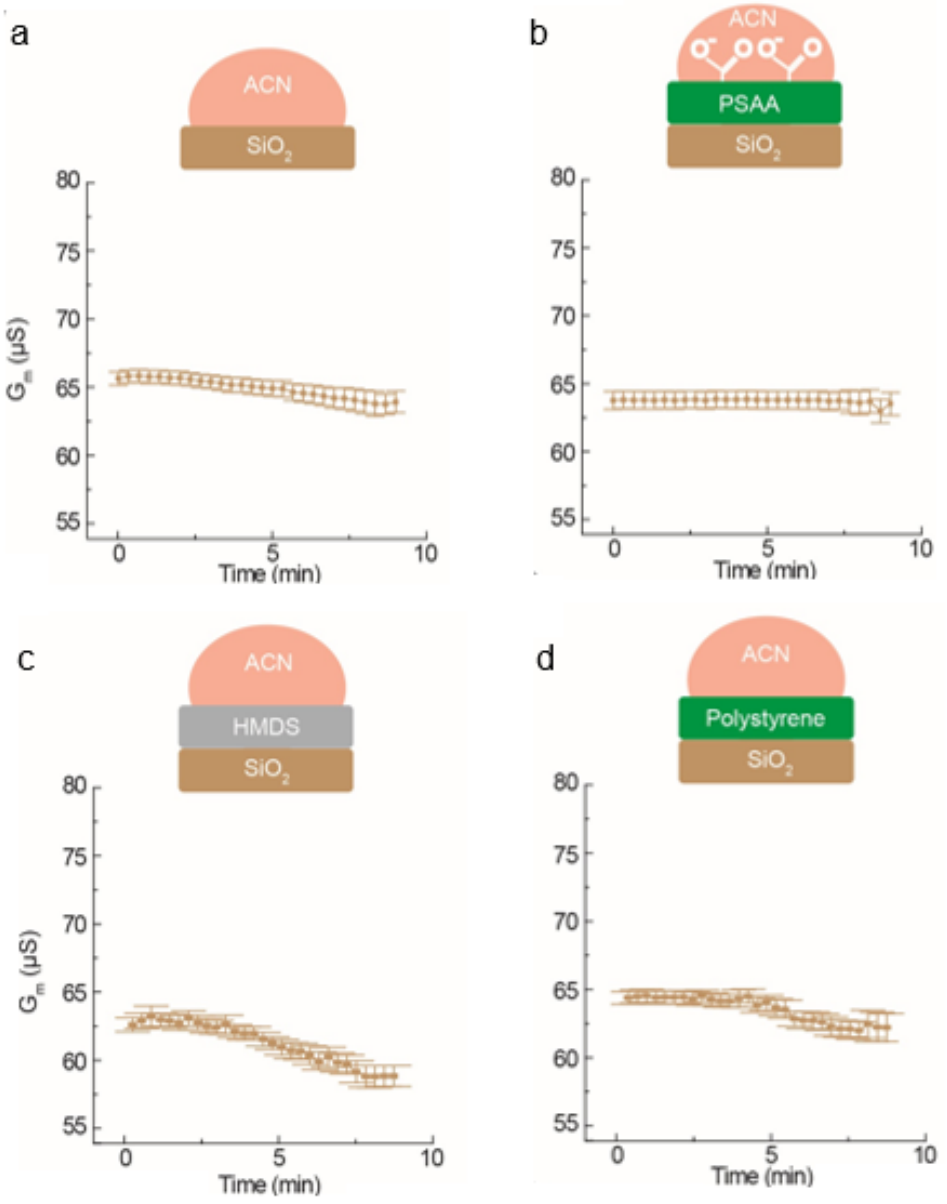

Figure 3.28. G_m distributions over at least 6 samples of RGs of (a) SiO_2, (b) PSAA/SiO_2, (c) HMDS/SiO_2, and (d) PS/ SiO_2 in ACN.

Total 1.6% reduction of G_m occurs after drift. Initial G_{m0} levels of PSAA (63.7 μS) are maintained without drift. On the other hand, there are huge reductions of high G_{m0} of PS (64.6 μS) and HMDS (62.7 μS) at initial stages by 6.1% and 4% after drift, respectively. This infers a slow orientation of dipole moment of ACN under repeated gate voltage. Therefore, the influence of dipole moment at the interface is more slowly reflected in drifts in $V_{th,RG}$ and G_m than the previous cases in water. That is, repeating gate voltage cycles slowly develops orientational ordering of ACN dipoles causing drift which in turn triggered hysteresis.

V_{th0} and V_{sat} for each RG in ACN are summarized in Figure 3.29. V_{th0} of non-polar surfaces of PS and HMDS with theoretically zero ionic charge is close to V_{th} of Si-FET which was observed in the case of PS and HMDS in pH7 water. V_{th0} of PSAA (1.58 V) increases compared to that of PS (1.5 V) due to the contribution of the negative charge of carboxylic acid groups. A similar V_{th0} between forward and reverse sweeping is observed over RG surfaces, indicating insignificant ΔV_{hys} at the initial state. Trivial $V_{th,RG}$ shifting without ΔV_{hys} is shown in the charged surfaces. V_{sat} of PS and HMDS measured forward sweeps converge to a specific range (PS: 1.89 V, HMDS: 1.82 V) by having as a large amount of ΔV_{dri} as was the case in pH7 water. V_{sat} levels of PS and HMSD are almost comparable with those in pH7 water. This indicates that a similar amount of net interfacial potential is achieved regardless of types of solution. Overall, higher dipole moments on uncharged hydrophobic surfaces were associated with larger ΔV_{dri}, ΔV_{hys}, even drift, and hysteresis in G_m.

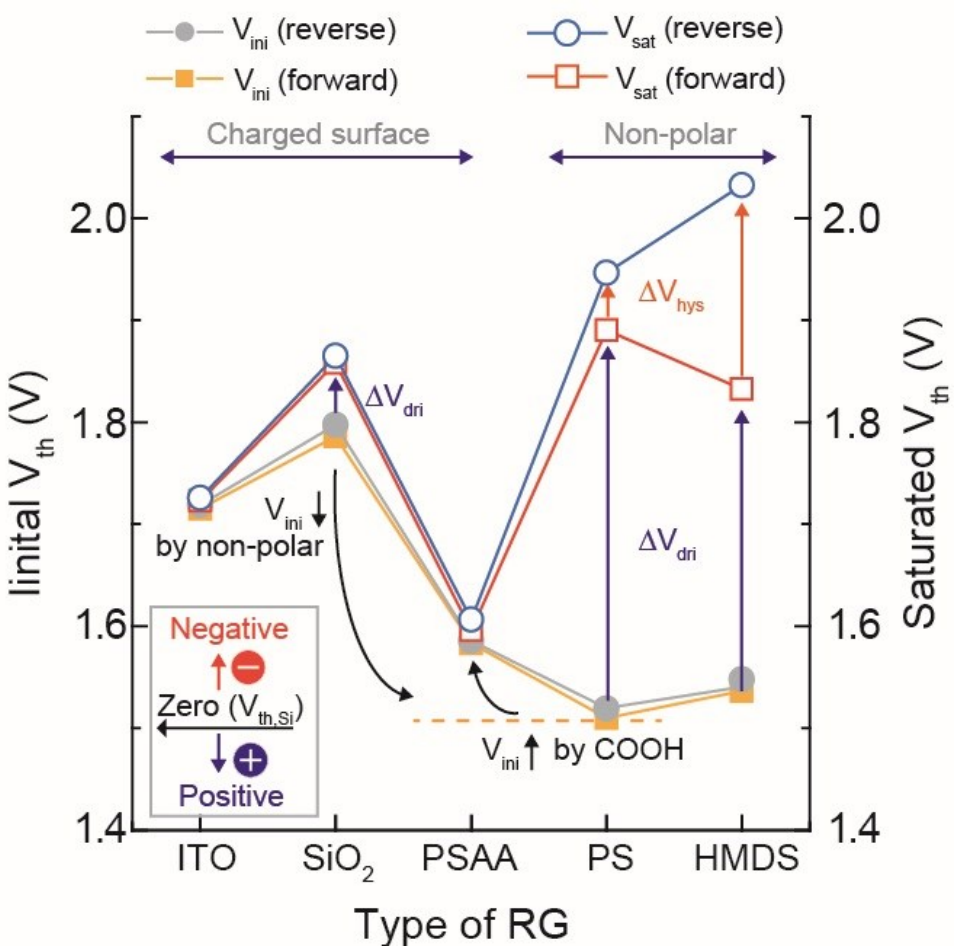

Figure 3.29. Average $V_{th,RG}$ at initial and saturation regime over at least 6 samples of RGs with ITO, SiO_2, PSAA/SiO_2, HMDS/SiO_2, and PS/ SiO_2 in ACN.

3.3.5. Conjugated polymers in water

Our observations so far, particularly those on ITO compared to the other RG materials and the reduced hysteresis of PSAA compared to PS, give rise to a clear criterion in designing a polymer sensing layer using charged and conductive components for greater electrochemical stability. Charged surfaces seem to achieve fast, stable equilibration of dipoles at the interfaces. At the same time, the designed polymer sensing layer needs to

have physical stability in aqueous solution. Now, we switch our attention to chargeable, conductive polymers such as P3HT for a sensing material.

Figure 3.30 presents representative transfer curves and G_m from P3HT RG surfaces in a pH 7 solution measured for 100 cycles under double sweeping mode. The transfer curves in Figure 3.30 are selected at measurements every ten times during 100 cycles. Repeating transfer curves and G_m curves show no significant or observable changes in the curves.

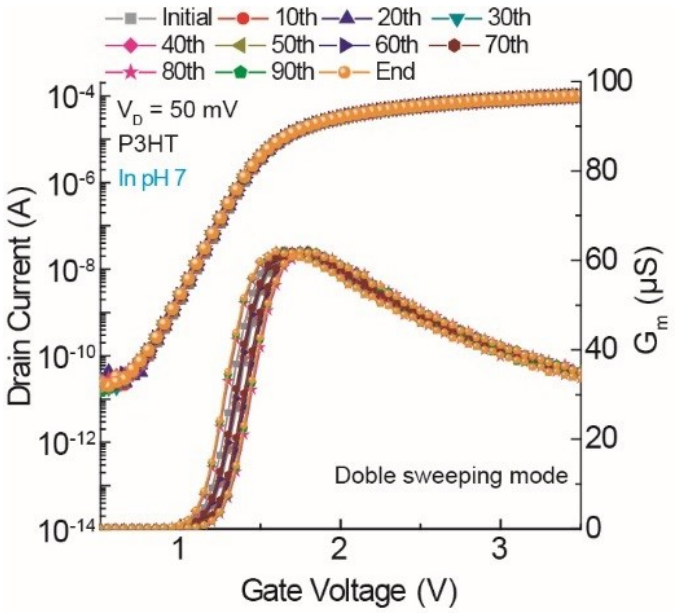

Figure 3.30. Zoomed-in representative transfer curves and G_m from P3HT RG in a pH 7 solution at the gate voltage ranges from 0 to 5 V measured for 100 cycles under double sweeping mode.

Figure 3.31 demonstrates drift curves in (a) $V_{th,RG}$ (b) G_m measured by both forward and reverse sweeps from P3HT RG in pH7 solution. $V_{th,RG}$levels measured by forward and reverse sweeps are exactly overlapped which results in an insignificant ΔV_{hys} of 0.5 mV.

.

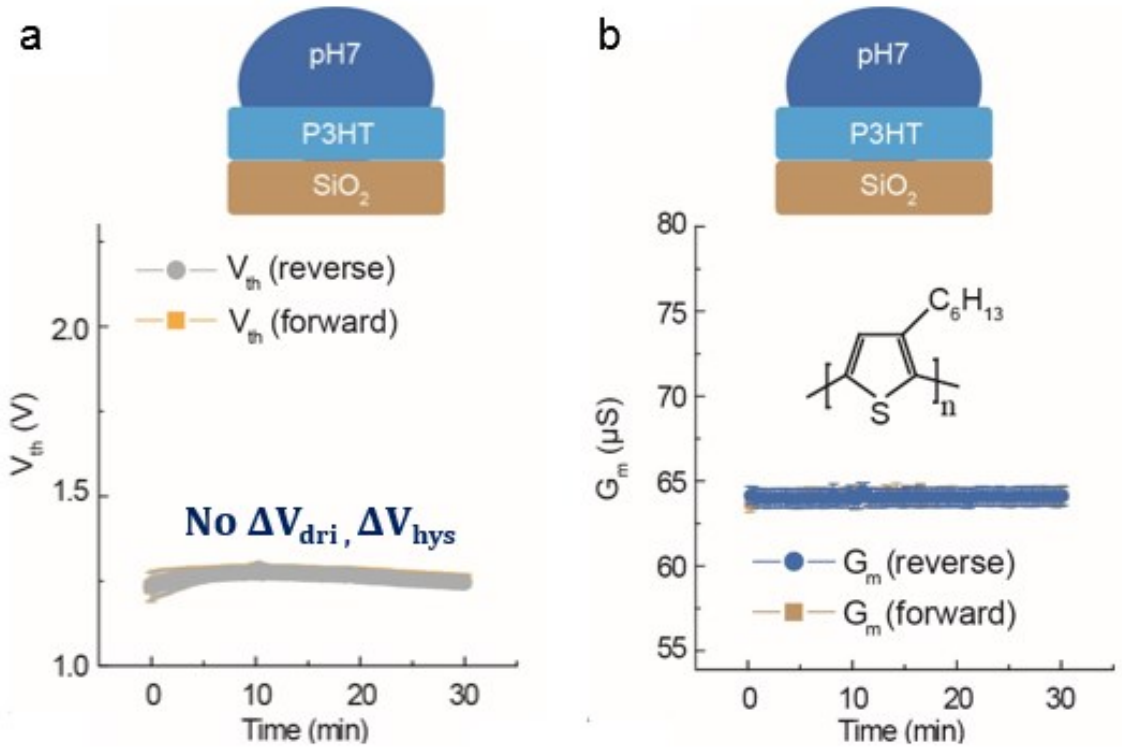

Figure 3.31. Distributions of (a) $V_{th,RG}$ and (b) G_m over at least 6 samples of RG with P3HT/SiO_2 in pH7 water. $V_{th,RG}$ and G_m are measured by both forward and reverse sweeping modes

There is the initial slight fluctuation in $V_{th,RG}$, leading to ΔV_{dri} of 18 mV. The positively charged surface of P3HT is characterized as a low V_{th0} of 1.23 V in pH7. High

G_{m0} of 64.3 μS remains stable over drift testing with no ΔG_{dri} and ΔG_{hys}. The strong positive charge of P3HT creates high stability in water.

In order to add bio-functionality into the P3HT, an acid-functionalized polythiophene, PT-COOH, is proposed. Figure 3.32 presents representative transfer curves and G_m from PT-COOH RG surfaces in a pH 7 solution measured for 100 cycles under double sweeping mode.

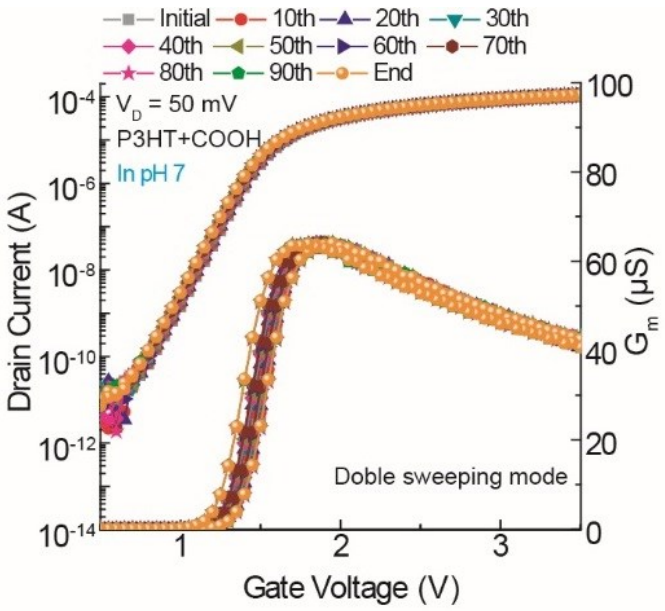

Figure 3.32. Zoomed-in representative transfer curves and G_m from PT-COOH RG in a pH 7 solution at the gate voltage ranges from 0 to 5 V measured for 100 cycles under double sweeping mode.

The transfer curves in Figure 3.32 are selected at measurements every ten times during 100 cycles. Repeating transfer curves and G_m curves show no significant or observable changes in the curves.

Figure 3.33 demonstrates drift curves in (a) $V_{th,RG}$ (b) G_m measured by both forward and reverse sweeps from PT-COOH RG in pH7 solution. PT-COOH even reveals the enhanced stability in drift (ΔV_{dri} of 17 mV) by having no fluctuation in the drift curve with ΔV_{hys} of 0.7 mV (Figure 3.33a).

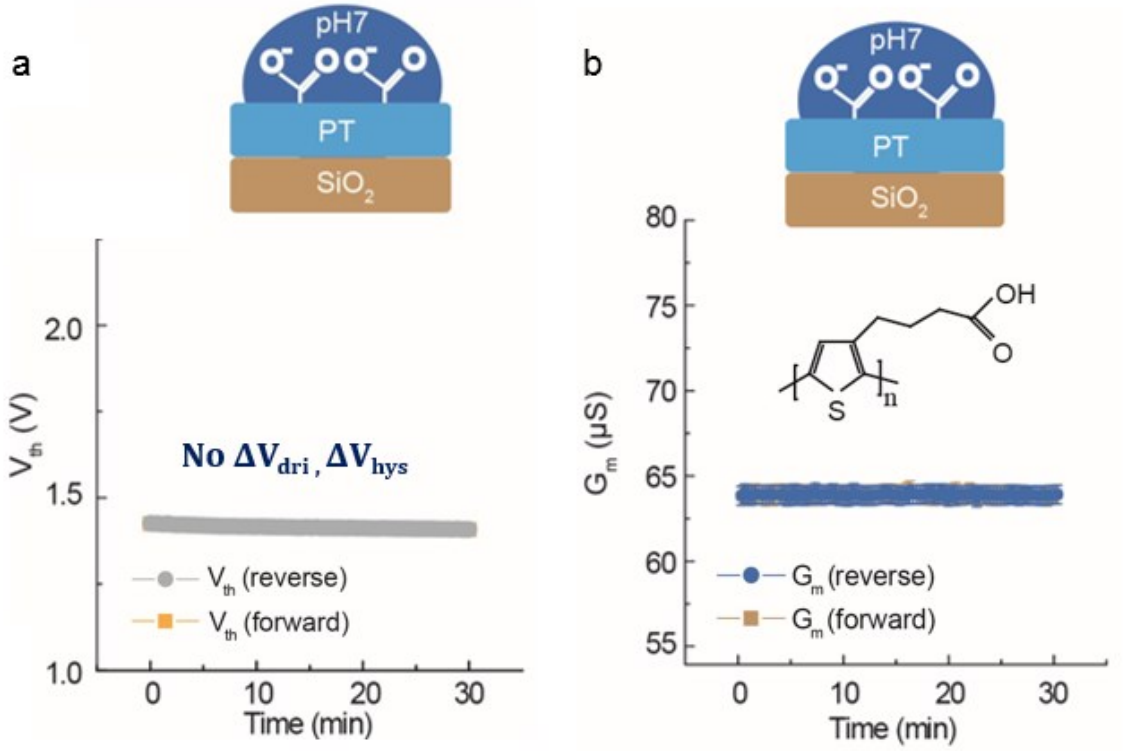

Figure 3.33. Distributions of (a) $V_{th,RG}$ and (b) G_m over at least 6 samples of RG with (a) PT-COOH/SiO_2 in pH7 water. $V_{th,RG}$ and G_m are measured by both forward and reverse sweeping modes.

The electrochemical stability of PT-COOH was almost comparable with that of ITO (Figure 4.6b). High G_{m0} of PT-COOH (64 μS) supports the presence of stable solution interface states between PT-COOH and aqueous media. $V_{th,RG}$ of 1.39 V increases compared to that on P3HT due to the negative charge contribution of ionized carboxylic acid groups in PT-COOH.

3.3.6. pH sensitivity of conjugated polymers

Current flow over sensing materials typically changes intrinsic properties of sensing materials by means of redox reactions. The RGFET system, however, avoids any current flow over a sensing material. With this advantage of the RGFET system, we demonstrate the intrinsic proton sensitivity of P3HT. Figure 3.34 shows representative transfer curves of a P3HT RG measured by double sweeping mode with increasing pH value that is in a range from pH3 to 11. After all pH measurements, the P3HT RG is measured at pH 3 again to confirm reversibility of pH sensitivity of P3HT. Transfer curves reveal V_{th} shifting as a function of pH values without changing the shape of the transfer curves.

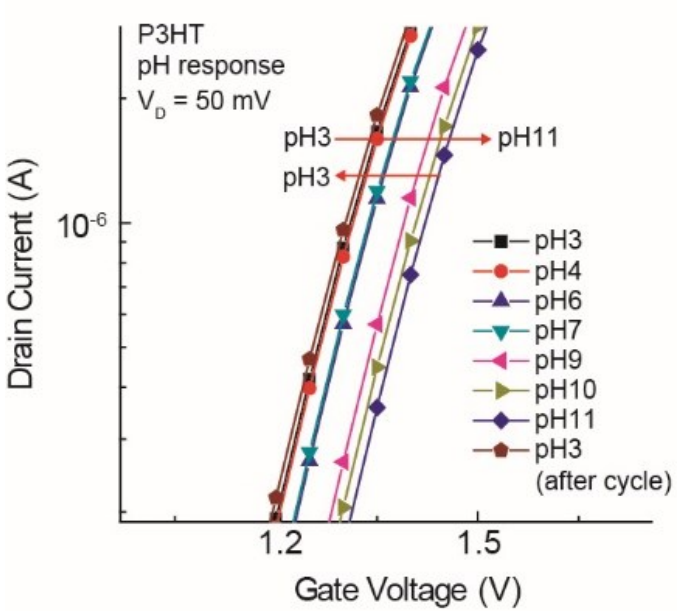

Figure 3.34. Zoomed-in representative transfer curves of P3HT/SiO_2 RG in terms of changes in pH value.

Figure 3.35 shows $V_{th,RG}$ and G_m distributions over of P3HT/SiO_2 as a function of pH values on time scale, respectively. Transfer curves are repeated for 20 times cycles for each pH solution. Reversible pH sensitivity is observed in Figure 3.35. There is no change in G_m over measurements while $V_{th,RG}$ is changed by different pH solutions.

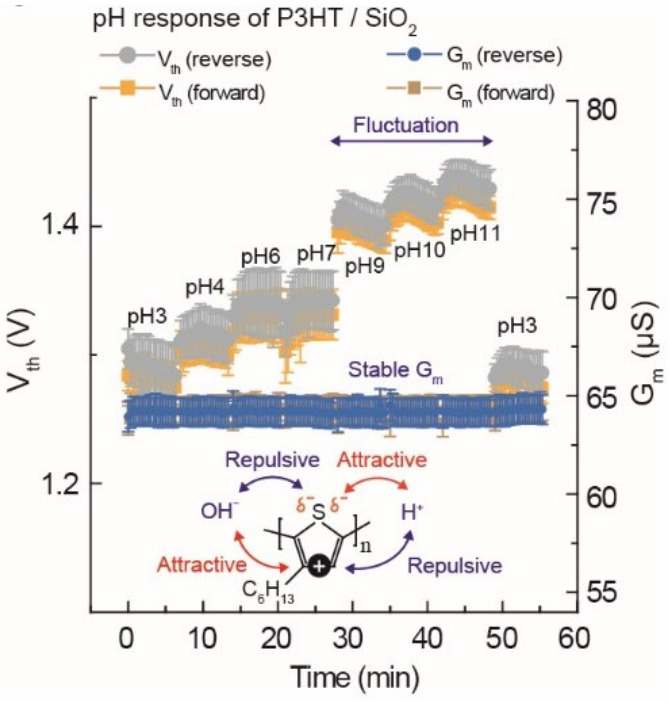

Figure 3.35. $V_{th,RG}$ and G_m distributions over 8 samples of P3HT in terms of changes in pH values along a time axis.

We also checked pH sensitivity of SiO_2 in case that pH sensitivity of P3HT could be affected by that of SiO_2. However, the pH response of SiO_2 seemed to be screened by hydration of water molecules, showing very limited pH sensitivity of 2 mV/pH (Figure 3.36). Also, G_m varies depending on pH values of solutions on SiO_2 between forward and reverse sweeps, indicating instable solution interfaces. Figure 3.36 supports intrinsic pH sensitivity of P3HT film. pH sensing behavior of P3HT, however, could not be explained by a site-binding model because there are no dissociable protons in P3HT. Rather, π-conjugated polymers become doped by protons and incorporate counterions.

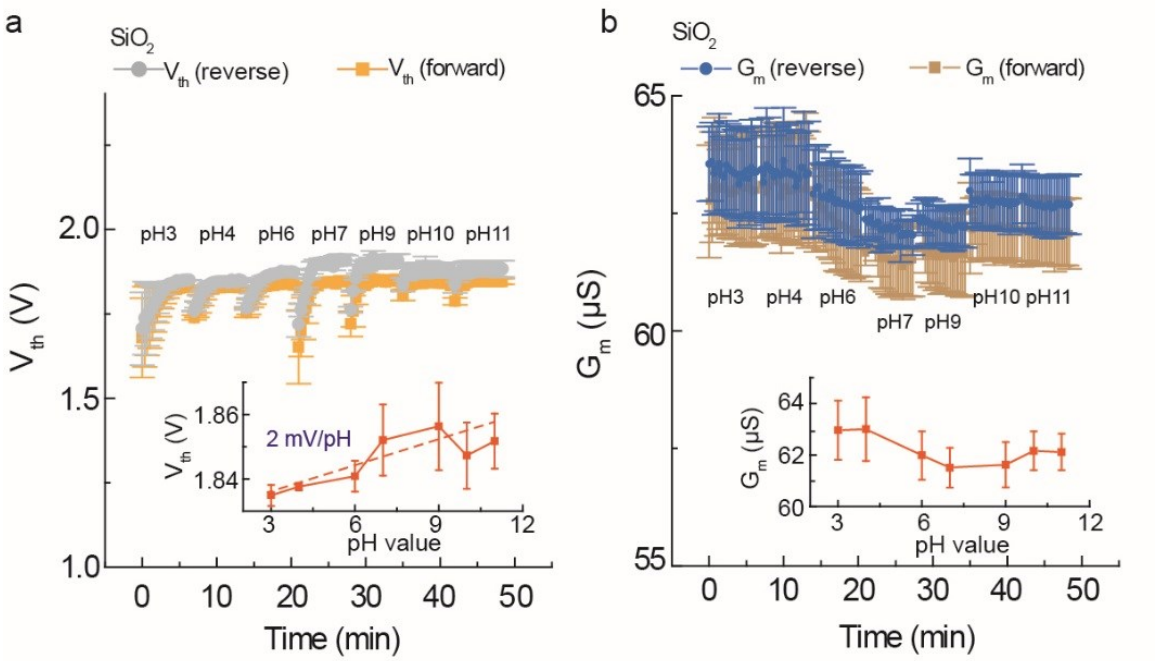

Figure 3.36. (a) $V_{th,RG}$ and (b) G_m distributions over 6 samples of SiO_2 in terms of changes in pH values along a time axis.

Figure 3.37 presents representative transfer curves of PT-COOH RG measured by double sweeping mode with increasing pH value that is in a range from pH3 to 11. The response of $V_{th,RG}$ for pH value is even larger than that in P3HT.

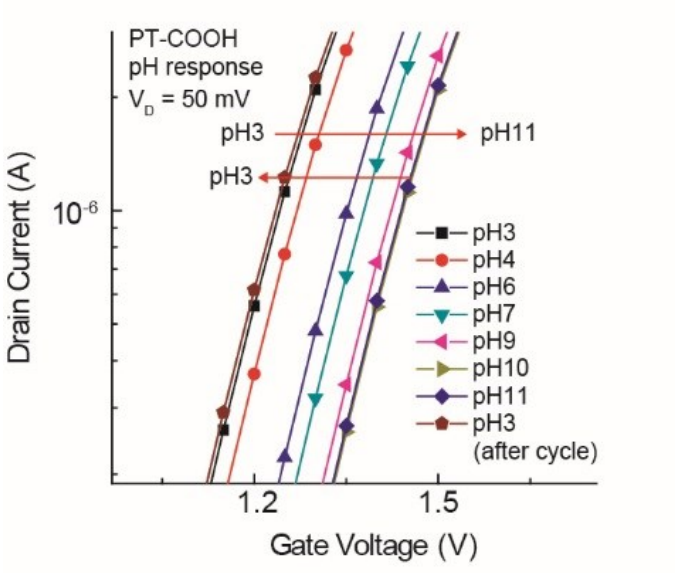

Figure 3.37. Zoomed-in representative transfer curves of PT-COOH/SiO_2 RG in terms of changes in pH value.

Figure 3.38 shows $V_{th,RG}$ and G_m distributions over of PT-COOH/SiO_2 as a function of pH values on time scale, respectively. Side chains of carboxylic acid in PT-COOH could increase proton interactions and mobility leading to an increase in pH response in acidic solutions. Relatively severe drift was shown in basic solutions ranging from pH9 to 11. This implied that some slow equilibration followed an initial penetration of OH^- ions. However, no change was seen in the high G_m levels for PT-COOH over all pH solutions, indicating a very stable solution interface.

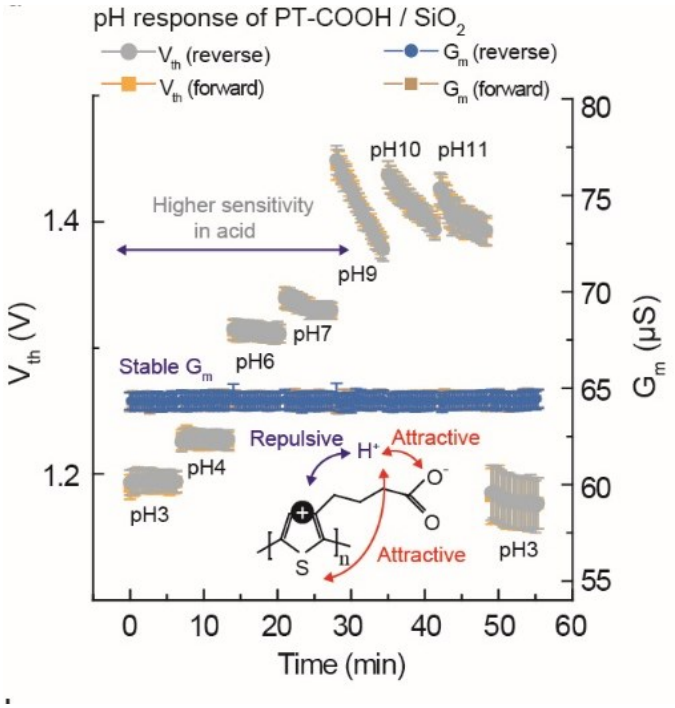

Figure 3.38. $V_{th,RG}$ and G_m distributions over 14 samples of PT-COOH RG in terms of changes in pH values along a time axis.

It would be interesting to compare pH sensitivity from PT-COOH with that of PSAA having hydrophobic components. Figure 3.39 shows (a) $V_{th,RG}$ and (b) G_m distributions over of PSAA/SiO_2 as a function of pH values on time scale, respectively. Drift in $V_{th,RG}$ caused by hydrations is observed for all pH solutions, which results in limited pH sensitivity of 5.4 mV/pH as shown in inset of Figure 3.39a. Also, G_m varies depending on pH values on PSAA between forward and reverse sweeps as was seen in SiO_2. Despite incorporation of carboxylic acids in PSAA, the activity or pH sensitivity from carboxylic acids is limited by undesirable hydration.

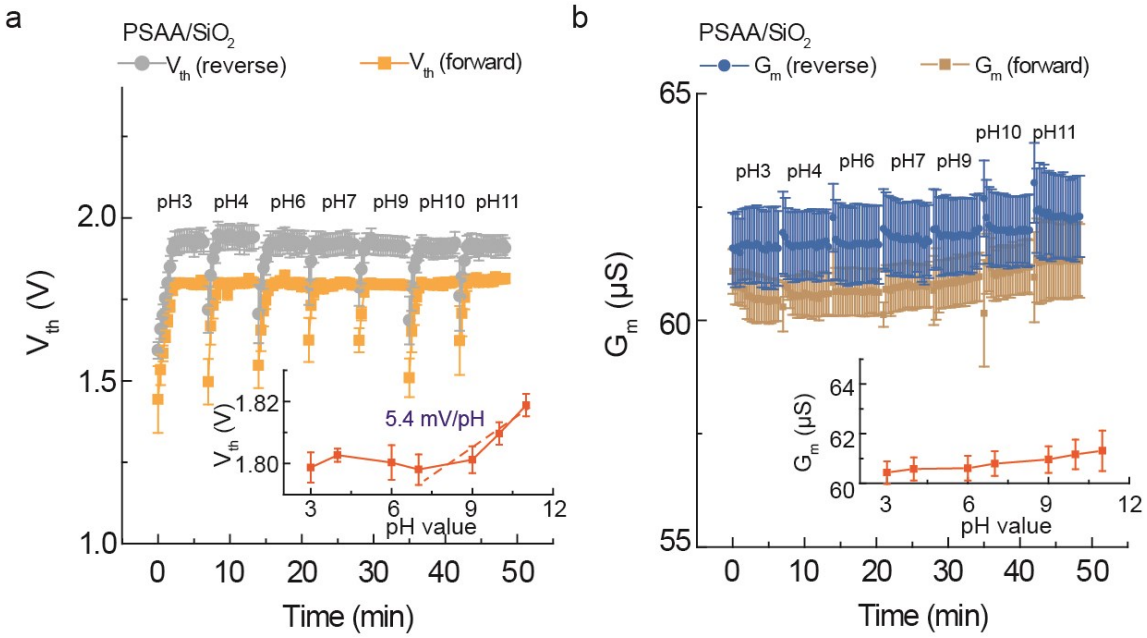

Figure 3.39. Distributions in (a) $V_{th,RG}$ and (b) G_m over 6 samples of PSAA RG in terms of changes in pH values on time scale.

Figure 3.40 shows comparison of $V_{th,RG}$ levels as a function of pH values from P3HT and PT-COOH surface. pH sensitivity of P3HT is estimated to be 17 mV/pH ranging pH3 to 10. On the other hand, PT-COOH reveals a larger pH sensitivity of 30 mV/pH ranging pH3 to 10 due to contribution of carboxylic acid groups in PT-COOH. pH sensitivity of PT-COOH is indicative of the surface accessibility and participation of a significant number density of COOH groups. Such sites could be electronically sensitive anchor points for bioreceptors such as antibodies.

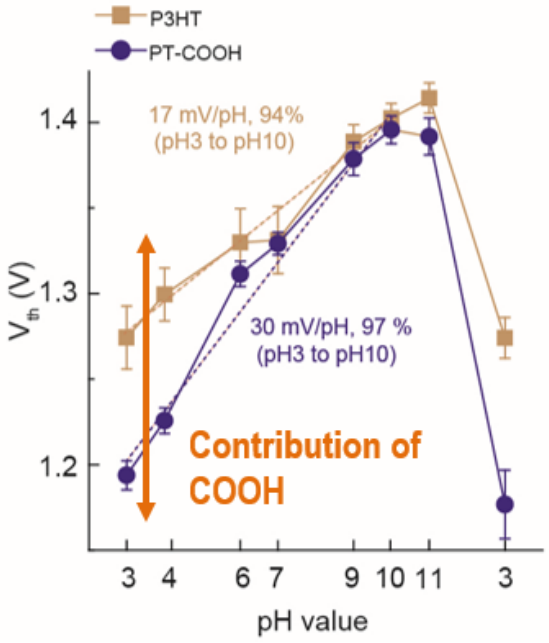

Figure 3.40. Comparison of average $V_{th,RG}$ over at least 6 samples of RGs with P3HT/SiO_2 and PT-COOH/SiO_2 as a function of pH values.

3.3.7. Summary

Our findings are summarized by plotting the V_{th0} and V_{sat} of each RG surface in pH7 water as shown in Figure 3.41a and 3.41b, respectively. High V_{th0} of SiO_2 (1.7 V) and low V_{th0} of P3HT (1.23 V) reflect the negatively and positively charged surface in pH7 water, respectively. Despite different thicknesses of films (HMDS: < 5 nm, PS: ca. 100 nm), V_{th0} of PS (1.55 V) and HMDS (1.56 V) are close to V_{th} of Si-FET as was also observed in ACN, indicating that the RGFET mostly translated the interface potentials. Negatively charged COO- in PSAA and PT-COOH increase each V_{th0} compared to their counterparts. Similar V_{sat} values for non-conductive surfaces indicated similar interface

potentials after drift once initially unfavorable solvent dipole orientations were equilibrated. Conductive surfaces show insignificant differences between V_{th0} and V_{sat}.

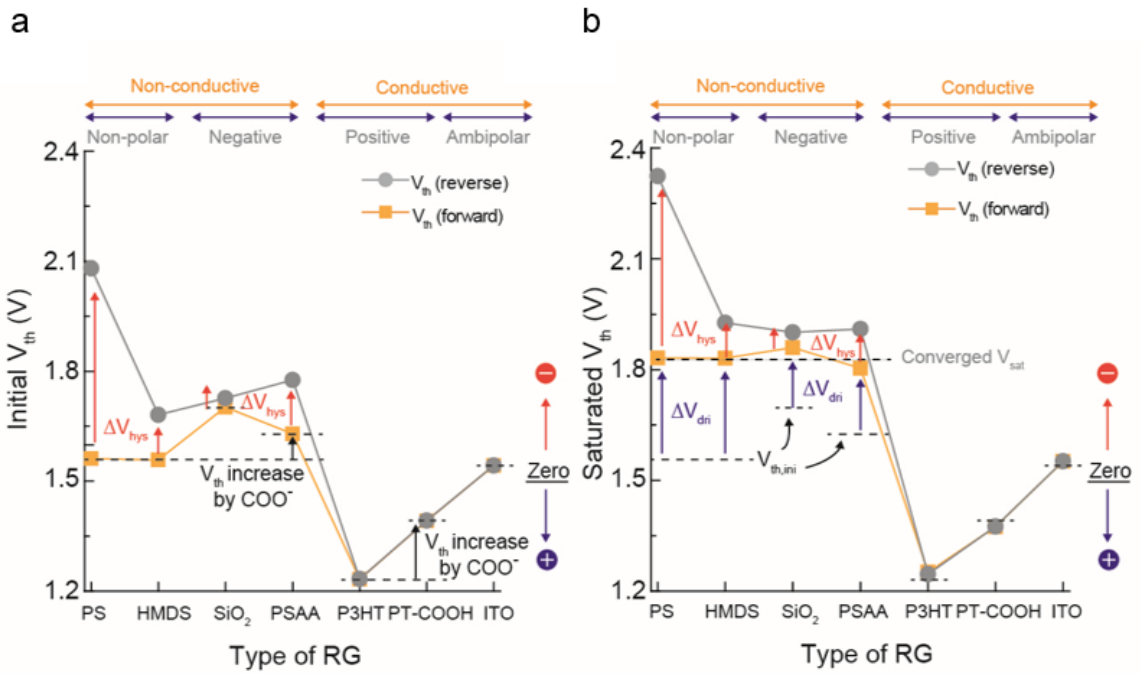

Figure 3.41. Average (a) V_{th0} and (b) V_{sat} over at least 6 samples of RGs with PS/SiO_2, HMDS/SiO_2, SiO_2, PSAA/SiO_2, P3HT/SiO_2, PT-COOH/SiO_2, and ITO.

We summarize average ΔV_{dri} and ΔV_{hys} in pH7 water in Figure 3.42. P3HT and PT-COOH shows high stability in aqueous solution almost comparable to that of ITO. Also, the trend of ΔV_{dri} and ΔV_{hys} (Figure 3.42) corresponds to that of ΔG_{dri} and ΔG_{hys} (Figure 3.43) as was true in ACN. Therefore, $\Delta V_{th,RG}$ is highly associated with ΔG_m in our RGFET system.

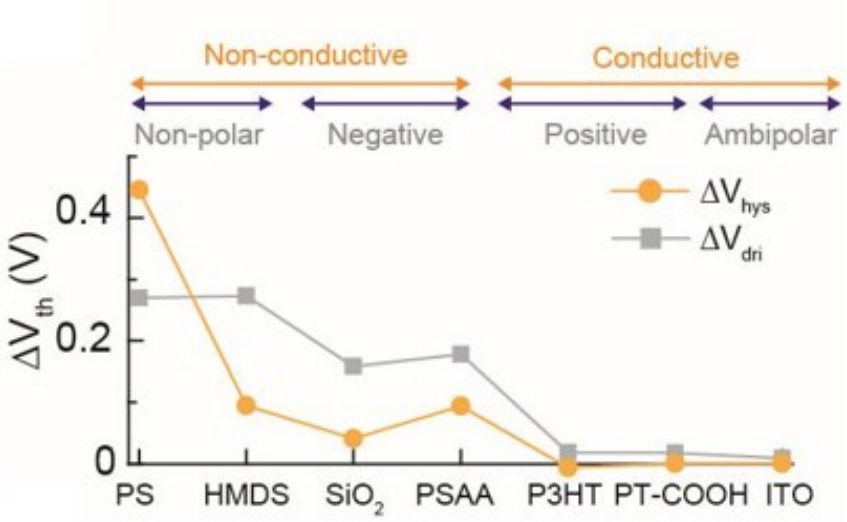

Figure 3.42. Average (a) ΔV_{hys} and (b) ΔV_{dri} over at least 6 samples of RGs with PS/SiO_2, HMDS/SiO_2, SiO_2, PSAA/SiO_2, P3HT/SiO_2, PT-COOH/SiO_2, and ITO.

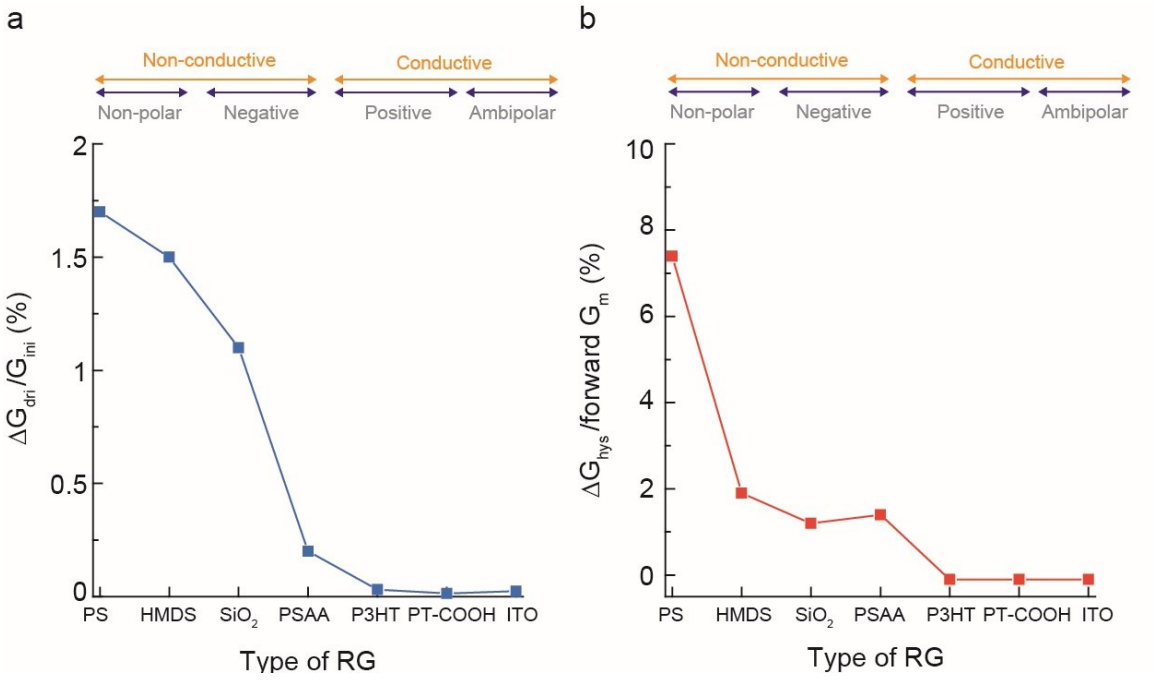

Figure 3.43. Average (a) ΔG_{dri} and (b) ΔG_{hys} over at least 6 samples of RGs with PS/SiO_2, HMDS/SiO_2, SiO_2, PSAA/SiO_2, P3HT/SiO_2, PT-COOH/SiO_2, and ITO.

3.4. Conclusion

We investigated how drift and hysteresis varies in terms of different electrostatic properties of surfaces and dipole moments in each solution. Fast, stable orientiational ordering of dipoles is achieved by charged surfaces. Hysteresis stems from the slower response of dipoles for already oriented dipoles at the interface. Non-polar components produce severe drift and hysteresis. Due to this fact, conjugated polymers with strong charges and physical stability in aqueous solution are highly recommended for incorporation as an active biosensing layer. We demonstrate that P3HT and PT-COOH have superior electrochemical instability, almost comparable to that of ITO. Also, by using the RGFET configuration, we present the intrinsic pH sensitivity of P3HT (17 mV/pH ranging from pH3 to 10) presumably occurring by ionic doping. The pH sensitivity of PT-COOH (30 mV/pH ranging from pH3 to 10) was greatly improved due to the further incorporation of proton-conducting functionalities. Our results suggest a criterion in designing new polymers for biosensing interfaces requiring receptor attachment combining conjugation and charged components in the material in order to stabilize dipole moments induced by EF. This criterion is in fact the one met by PEDOT-PSS and related polymers now used in organic electrochemical transistors, and is now suggested even for sensing layers that interact with analytes purely by polarization mechanisms.

3.5 References

(37) Bousse, L.; Bergveld, P. *Journal of Electroanalytical Chemistry* **1983**, *152*, 25.

(38) Abe, H.; Esashi, M.; Matsuo, T. *Ieee Transactions on Electron Devices* **1979**, *26*, 1939.

(39) Jamasb, S.; Collins, S. D.; Smith, R. L. *Ieee Transactions on Electron Devices* **1998**, *45*, 1239.

(40) Kergoat, L.; Piro, B.; Berggren, M.; Horowitz, G.; Pham, M. C. *Analytical and Bioanalytical Chemistry* **2012**, *402*, 1813.

(41) Lee, B.; Wan, A.; Mastrogiovanni, D.; Anthony, J. E.; Garfunkel, E.; Podzorov, V. *Physical Review B* **2010**, *82*.

(42) Lai, S.; Demelas, M.; Casula, G.; Cosseddu, P.; Barbaro, M.; Bonfiglio, A. *Adv Mater* **2013**, *25*, 103.

(43) Parlak, O.; Keene, S. T.; Marais, A.; Curto, V. F.; Salleo, A. *Science Advances* **2018**, *4*.

(44) Magliulo, M.; Mallardi, A.; Mulla, M. Y.; Cotrone, S.; Pistillo, B. R.; Favia, P.; Vikholm-Lundin, I.; Palazzo, G.; Torsi, L. *Advanced Materials* **2013**, *25*, 2090.

(45) Lu, W.; Fadeev, A. G.; Qi, B. H.; Smela, E.; Mattes, B. R.; Ding, J.; Spinks, G. M.; Mazurkiewicz, J.; Zhou, D. Z.; Wallace, G. G.; MacFarlane, D. R.; Forsyth, S. A.; Forsyth, M. *Science* **2002**, *297*, 983.

(46) Savva, A.; Cendra, C.; Giugni, A.; Torre, B.; Surgailis, J.; Ohayon, D.; Giovannitti, A.; McCulloch, I.; Di Fabrizio, E.; Salleo, A.; Rivnay, J.; Inal, S. *Chemistry of Materials* **2019**, *31*, 927.

(47) Li, H.; Shi, W.; Song, J.; Jang, H. J.; Dailey, J.; Yu, J. S.; Katz, H. E. *Chemical Reviews* **2019**, *119*, 3.

(48) Xu, S. Y.; Han, X. Z. *Biosensors & Bioelectronics* **2004**, *19*, 1117.

(49) Bousse, L.; Mostarshed, S.; Vandershoot, B.; Derooij, N. F.; Gimmel, P.; Gopel, W. *Journal of Colloid and Interface Science* **1991**, *147*, 22.

(50) Welch, D.; Shah, S.; Ozev, S.; Christen, J. B. *Ieee Electron Device Letters* **2013**, *34*, 456.

(51) Guardado, J. O.; Salleo, A. *Advanced Functional Materials* **2017**, *27*.

(52) Bousse, L.; Derooij, N. F.; Bergveld, P. *Ieee Transactions on Electron Devices* **1983**, *30*, 1263.

(53) Jamasb, S.; Collins, S. D.; Smith, R. L. *Transducers 97 - 1997 International Conference on Solid-State Sensors and Actuators, Digest of Technical Papers, Vols 1 and 2* **1997**, 1379.

(54) Martinoia, S.; Grattarola, M.; Massobrio, G. *Sensors and Actuators B-Chemical* **1992**, *7*, 561.

(55) Bousse, L.; Bergveld, P. *Sensors and Actuators* **1984**, *6*, 65.

(56) Wang, H. N.; Pilon, L. *Journal of Physical Chemistry C* **2011**, *115*, 16711.

(57) Ma, M. M.; Zhao, S. L.; Xu, Z. L. *Communications in Computational Physics* **2016**, *20*, 441.

(58) Dreier, L. B.; Nagata, Y.; Lutz, H.; Gonella, G.; Hunger, J.; Backus, E. H. G.; Bonn, M. *Science Advances* **2018**, *4*.

(59) Gongadze, E.; Iglic, A. *Bioelectrochemistry* **2012**, *87*, 199.

(60) Booth, F. *Journal of Chemical Physics* **1951**, *19*, 391.

(61) Aguilella-Arzo, M.; Andrio, A.; Aguilella, V. M.; Alcaraz, A. *Physical Chemistry Chemical Physics* **2009**, *11*, 358.

(62) Lamm, G.; Pack, G. R. *Journal of Physical Chemistry B* **1997**, *101*, 959.

(63) Sato, T.; Sasaki, T.; Ohnuki, J.; Umezawa, K.; Takano, M. *Physical Review Letters* **2018**, *121*.

(64) Despa, F.; Fernandez, A.; Berry, R. S. *Physical Review Letters* **2004**, *93*.

(65) Lue, C. E.; Wang, I. S.; Huang, C. H.; Shiao, Y. T.; Wang, H. C.; Yang, C. M.; Hsu, S. H.; Chang, C. Y.; Wang, W.; Lai, C. S. *Microelectron Reliab* **2012**, *52*, 1651.

(66) David E . Yates, S. L., Thomas W. Healy *J. Chem. Soc., Faraday Trans. 1,* **1973**, *70*, 1807.

Chapter 4

Antibody-embedded sensing membrane

4.1. Introduction

One of the most reliable and common immunoassay platforms for screening for various diseases so far has been the enzyme-linked immunosorbent assay (ELISA), which is based on the optical reading of complexes between targeting biomarkers and enzyme-conjugated antibody by measuring the absorbance of light of a product colored by enzyme reactions. However, this detection mechanism is highly limited in the efficiency of diagnostics of wide-reaching, contagious diseases, inevitably requiring laboratory facilities and bulky analyzers such as spectrometers and colorimeters.

It remains desirable to develop a point-of-care (PoC) testing tool that is simple, sensitive, selective, low-cost, and usable anywhere. Electronic sensors based on FETs have shown potential to meet the aforementioned criteria.[68-70] The multiple laboratory processes are scaled down to a chip format, while retaining the following qualities.[71-73] Indeed, significant progress has been made in the field of transistor sensors. Despite these scientific advancements, transistor sensors are still subject to several hurdles in terms of their practicality.

For the detection mechanism, semiconductor-dependent resistance of transducers varies when analyte binds to receptors functionalized on the sensing surface. That is, signal comes from variations of pI on the surface resulting from interactions between receptor and analyte. At this point, a main challenge for the transistor sensors is posed by the Debye screening length (λ_D), arising from the interaction between the sensing surface and electrolyte.[74-76] λ_D can be expressed as:

$$\lambda_D = \frac{1}{\sqrt{4\pi l_B \sum_i \rho_i z_i^2}}$$

where l_B is the Bjerrum length (0.7 nm), $\sum_i$ is the sum over all ion species, and ρ_i and z_i are density and valence of ion species *i,* respectively. Calculated λ_D depending on ion strength of the PBS solution is shown in Figure 4.1. When physical lengths of antibody-antigen complexes are longer than λ_D associated with physiological media, transistor sensors are no longer effective in physiological samples, theoretically. To be specific, FET biosensors fail to recognize the binding events in high ionic strength solution higher than 100 mM.[77] Thus, for optimal sensing, the λ_D must be carefully selected for FET biosensors because molecules binding to the devices are removed from the sensor surface above λ_D.

A common approach to address λ_D issues is for the analyte in body fluid to be mixed with diluted phosphate buffered saline (PBS) solution, increasing λ_D .[78] Alternatively, capture-release methods can be applied. In this method, a body fluid is placed on a sensor surface first, resulting in the analyte binding to a surface receptor, after which the original solution is replaced with diluted PBS to read the binding signal,[79] complicating the procedure in clinical setups. Another way to overcome λ_D is reducing the physical size of receptors by using aptamers (3-5 nm),[80] peptides (7 to 14 amino acids long),[81] and antibody fragments (<10 nm).[82] However, it is difficult for existing receptors to be scaled down below the λ_D of physiological samples as shown in Figure 4.1.

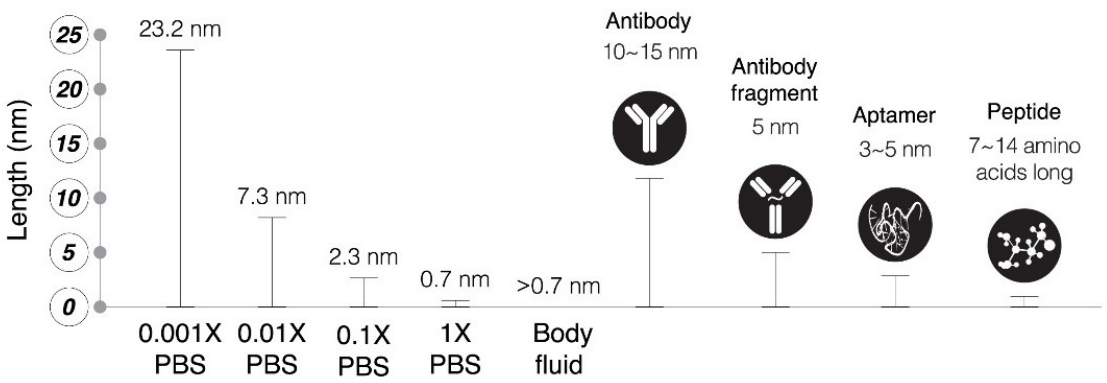

Figure 4.1. Debye lengths varied by ionic strengths and physical size of receptors such as antibody, antibody fragment, aptamer, and peptide.

In this chapter, an antibody-embedded polymer membrane as an alternative to the conventional bio-conjugating method of surface-functionalization is discussed. A presumed schematic image of antibody-embedded geometric in PSMA polymer matrix is depicted in Figure 4.2.

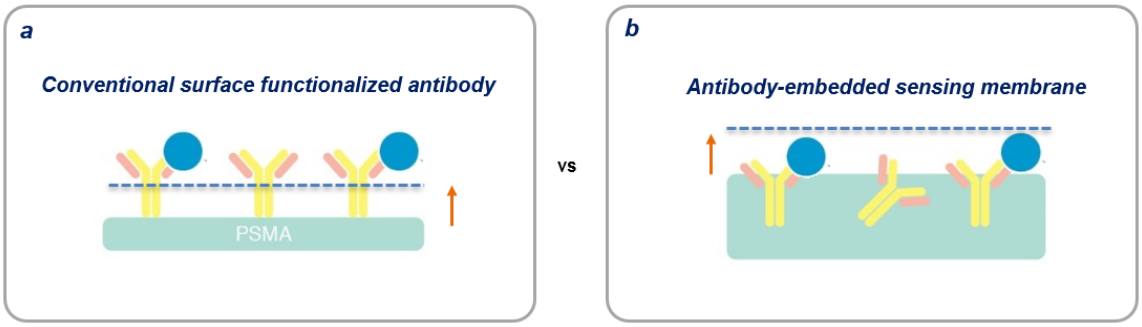

Figure 4.2. Schematic images of (a) conventional surface-functionalized antibody and (b) newly proposed antibody-embedded sensing membrane.

One of the main goals of using an antibody-embedded sensing membrane is to overcome the Debye length issue by making bio-signals near sensing surfaces or within a short Debye length from highly concentrated media.

As proof-of-concept, we designed a system to detect cortisol in lightly buffered artificial sweat with LOD of 1 ng/ml by using antibody-embedded polymer sensing membrane. Cortisol is a stress biomarker found in sweat, saliva, blood, urine and interstitial fluid.[83-85] Typical cortisol quantification methods include chromatographic techniques, ELISA, surface plasmon resonance, and electrochemical impedance spectroscopy, all requiring bulky equipment and several steps in determining cortisol levels.[86,87] Physiological cortisol levels in human perspiration reported ranges from 8.16 to 141.7 ng/ml.[88,89]

The embedded structure of receptor in the polymer, polystyrene-*co*-methacrylic acid (PSMA), allows cortisol molecules to bind near the membrane-substrate interface, which ameliorates the λ_D issues. The developed sensing membrane is coupled to a commercial FET as the RG module. In RGFET setup, sensitivity for cortisol is obtained in a range from 10 fg/ml to 10 ng/ml with the guaranteed LOD of 1 pg/ml in 1× PBS where λ_D is 0.7 nm. This sensing performance from antibody-embedded PSMA is compared with the conventional way that functionalize antibody on the surface, PSMA. We refer antibody-embedded PSMA and antibody-surface-functionalized PSMA as anti-em PSMA and anti-suf PSMA, respectively. Sandwich ELISA was performed to confirm activity of anti-em PSMA. To the best of our knowledge, this is the first demonstration of an FET-based cortisol sensor yet reported.

4.2. Experimental section

4.2.1. Sample preparation for antibody functionalization

ITO/PET substrates purchased from Sigma Aldrich were used. The substrates are sliced into 1.5 × 2 cm for the remote electrode. The substrates are cleaned with isopropanol for 20 min under ultrasonication, then rinses with distilled water for 20 min, and dried under nitrogen gas. 10 mg/ml PSMA (678240, Sigma Aldrich) is added in a mixed solvent composed of 0.5 ml dichloromethane (DCM), 0.5 ml N,N-dimethylformamide (DMF), and 40 mg/ml of 1-Ethyl-3-(3-dimethylaminopropyl)carbodiimide (EDC). DMF is chosen among the organic solvents because high antibody activity was observed over an extended period in this solvent[90]. After an hour, 15 mg/ml N-hydroxysuccinimide (NHS) is added to the mixture. EDC/NHS is added to activate the carboxylic acid groups of PSMA. After spin-coating PSMA on ITO/PET substrate, 100 µl of 1 mg/ml antibody (CORT-2, abcam) is immobilized on the surface by drop-coating for 6 hours at room temperature.

For anti-em PSMA, 100 µl of 1 mg/ml anti-cortisol is added 20 min after addition of NHS and stirred for 4 hours. The mixture is constantly stirred at room temperature during the functionalization procedure from the beginning at 180 rpm with a stir bar. The resulting mixture is spin-coated on the freshly cleaned ITO/PET substrate, first at 500 rpm for 10 seconds, then at 3000 rpm for 120 seconds. The thickness of anti-em PSMA is about 300 nm measured by LASER microscopy. O-ring with diameter of 4.5 mm and height of 1.78 mm was attached by epoxy glue to form a chamber.

4.2.2. Electrical measurement

Sensing membranes completed by following procedures above are connected to the gate of commercial FETs. An Ag/AgCl reference electrode is used to apply the gate bias for all measurements. All transfer curves are measured using a Keithley semiconductor analyzer, at a drain voltage of 50 mV with the gate voltage double sweep mode. For cortisol tests in both anti-em and -suf PSMA membranes, cortisol (C-106, Cerilliant) dissolved in methanol at concentration 1 mg/ml is diluted in 1× and 0.05× PBS to concentrations of 1 fg/ml to 10 ng/ml. For the specificity test, 17-α-HPG (H5752, Sigma Aldrich) dissolved in methanol at concentration 1 mg/ml is diluted in 1× and 0.05× PBS to the same concentrations as cortisol samples. For sweat tests, two types of artificial perspiration with different pH are purchased from Pickering Laboratories (Catalog number: 1700-0521 for pH 7.4 and 1700-0024 for pH4.5). 10% of 1× PBS is added in the artificial perspiration as a buffer against non-ideal factors such as shifting background pH values. This mixture between artificial sweat and 1× PBS is used to dilute 1 mg/ml cortisol. Before evaluating drift or quantifying cortisol, all PSMA membranes are stabilized for 30 - 40 minutes in PBS solution after three times washing by PBS. Transfer curves for each cortisol concentration are measured after 5 min of incubation with the cortisol solution, following initial stabilization of the membrane, using 20 μl of sample solution.

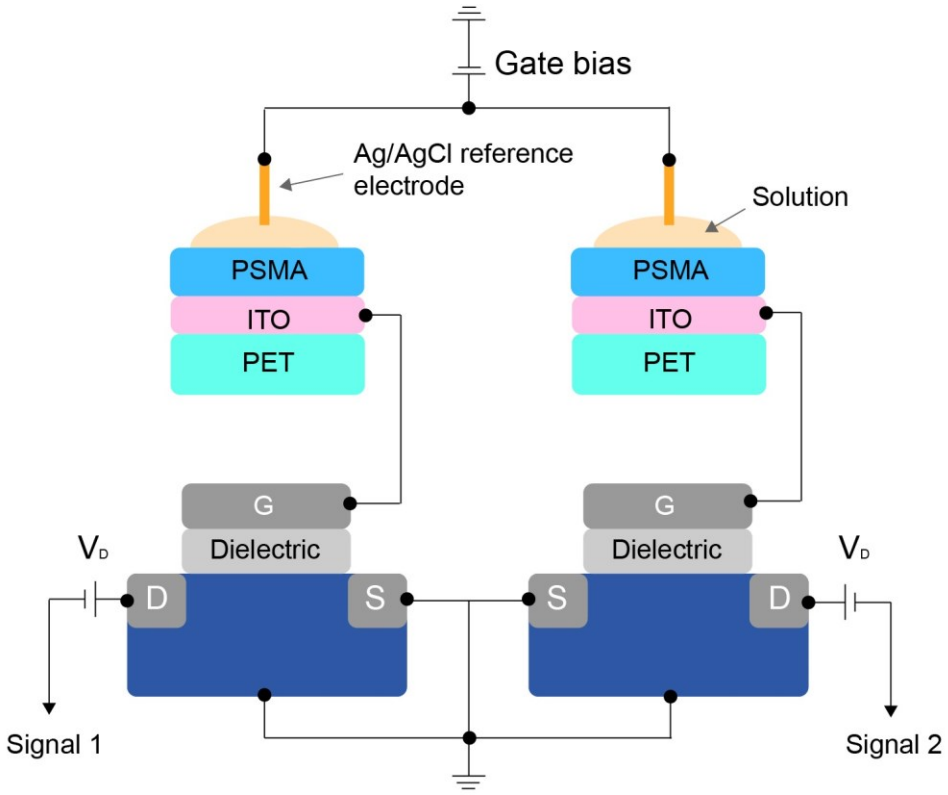

Figure 4.3. Schematic image of the measurement system. Two different remote sensing gates were coupled to the gate of each commercial FET.

Our measurement system allowed the acquisition of two different electrical signals at the same time from two different sensing gates as shown in Figure 4.3. One of two sensing gates is monitored as a control setup. ITO/PET substrate is chosen as substrate of the RG to demonstrate sensing performance on the flexible materials. Each RGFET system in Figure 4.3 yields almost the same transfer curves in Figure 4.4 although each PSMA membrane is independently connected to the individual FET as shown in Figure 4.3. Also, there is no hysteresis observed during double sweeping mode, which indicates high stability of the transducing system as well as high reproducibility of the sensing system.

Any change in electrical signal on the sensing surface is transmitted to the gate of each FET[91,92].

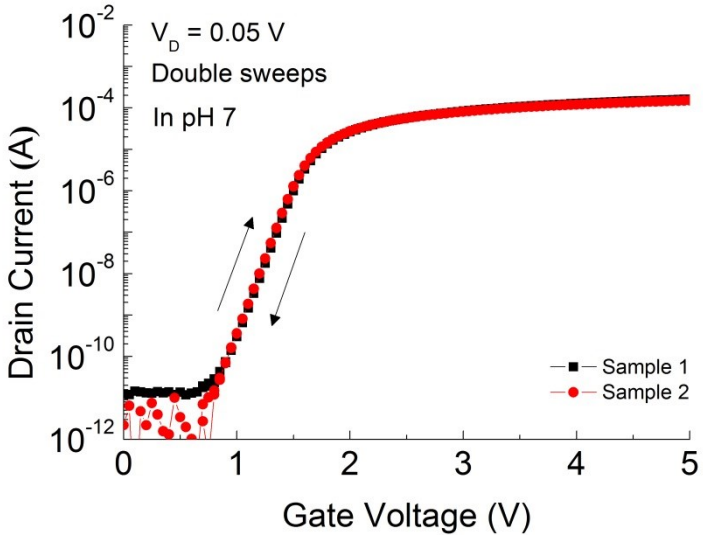

Figure 4.4. Transfer curves of two PSMA RGs separately coupled to two different Si-FET. The measurements are performed in pH7, simultaneously.

4.2.3. ELISA test

Two different types of samples are prepared for a fluorescence scan: surface functionalized PSMA samples and antibody embedded PSMA samples. Following the antibody functionalization methods discussed above, an ethanolamine treatment is applied prior to the ELISA FI measurement. Without ethanolamine, additional non-specific binding occurs by the detection antibody. Therefore, ethanolamine is added to deactivate COOH groups on the surface to minimize non-specific binding. Ethanolamine (pH 13) is brought to pH 8.5 by adding hydrochloric acid.

For ELISA on the surface functionalized membrane, 10 mg/ml PSMA in the same organic solution as before is spin-coated on ITO/PET substrate with surface sensing area of 0.5 cm x 0.5 cm. 25 μL of 1 mg/ml of the primary antibody (anti-cortisol) is then drop-coated and left at room temperature for 6 hours. After 6 hours, the surface is washed 5 times using 1× PBS. Ethanolamine solution is used to cover the functional surface and reacted for 20 minutes at room temperature. After 20 minutes, the surface is washed 5 times using 1× PBS. 100 μL of 100 μg/mL cortisol solution is then dropped on the surface and left at room temperature for reaction with the surface functionalized primary antibody. After 30 minutes of reaction time, the surface is washed 5 times using 1× PBS. Finally, 80 μL of 200 ng/ml fluorescein isothiocyanate (FITC) conjugated cortisol antibody (LS-C305750, LifeSpan BioSciences) is dropped on the washed surface and left at room temperature for reaction with the cortisol-antibody complex immobilized on the surface. After 30 minutes of reaction time, the surface is washed 5 times using 1× PBS. Fluorescence scans are conducted on the samples via a plate reader. For antibody-embedded samples, 10 mg/ml PSMA in DCM/DMF and EDC/NHS samples are prepared as above. The primary antibody is injected into the PSMA solution 20 minutes after adding NHS. The PSMA solution is stirred at room temperature for 4 hours. The same procedures as surface functionalized samples are repeated to measure the FI.

4.3. Results and Discussion

4.3.1. Surface-functionalized PSMA

Physiological stress is considered a silent contributor to diverse diseases[93,94]. Cortisol sensors based on sweat test enable the monitoring of stress levels non-invasively.

Physiological cortisol levels in human perspiration reported ranges from 8.16 to 141.7 ng/ml[88,89].

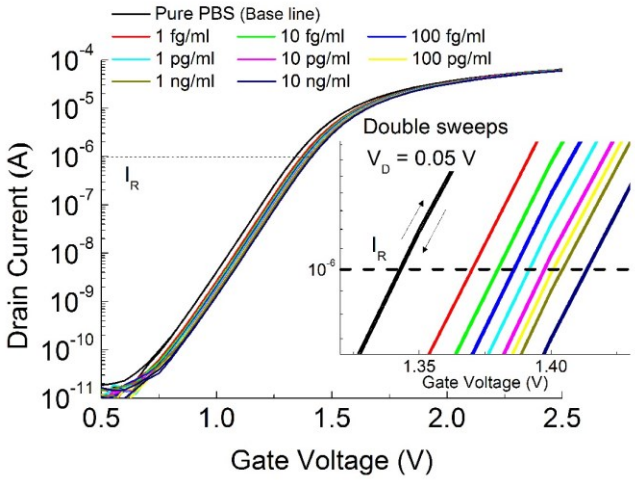

Figure 4.5. Representative transfer curves of anti-suf PSMA with increasing cortisol concentrations in 0.05× PBS at the gate voltage ranges from 0 to 2.5 V. Inset: close-up transfer curves.

Shifts in transfer curve switching voltages for different concentrations of cortisol indicate the cortisol sensitivity from anti-suf PSMA (Figure 4.5). Close-up transfer curves are shown in inset of Figure 4.5. No significant hysteresis by double sweeping mode is observed in transfer curves. Cortisol increases V_R levels of n-type FET transducer, which indicate that negative charges are imposed on the RG system due to interactions between cortisol and anti-cortisol.

Figure 4.6 shows the response of transfer curves from pure PSMA that has no anti-cortisol on PSMA surfaces for different cortisol concentrations. There are random shifts of transfer curves observed.

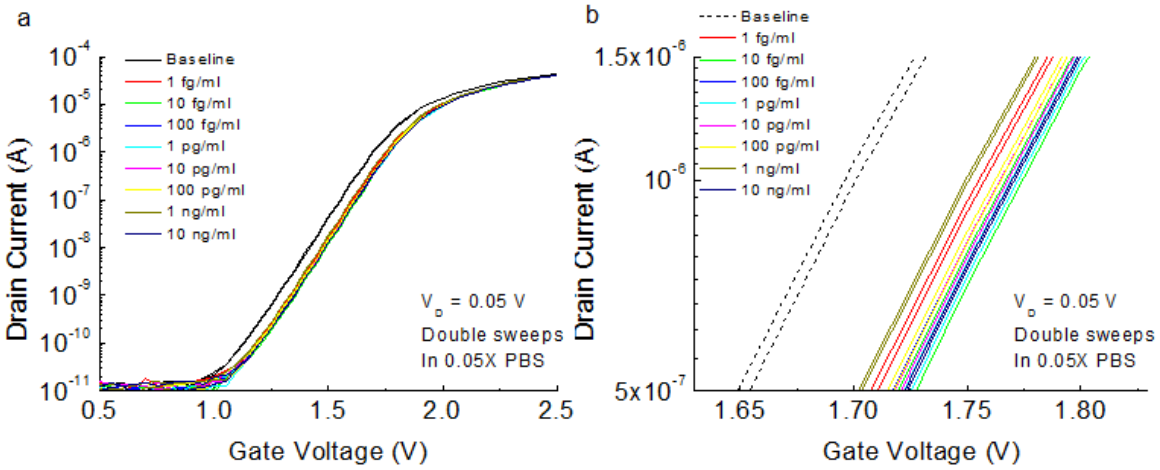

Figure 4.6. (a) Representative transfer curves of the pure PSMA with increasing cortisol concentrations in 0.05× PBS at the gate voltage ranges from 0 to 2.5 V. (b) Close-up transfer curves of Figure 4.6a.

Figure 4.7 presents the response of transfer curves of anti-suf PSMA for 17-a-HPG concentrations as control. 17-a-HPG is a biochemical precursor of cortisol and is chosen for our specificity tests because it has a structure and size similar to those of cortisol. The anti-cortisol antibody [CORT-2] we used has 100% reactivity to Cortisol and 0% reactivity to 17-α-HPG according to a data sheet provided by Abcam. This reactivity is reflected in our data. There are random shifts of transfer curves observed.

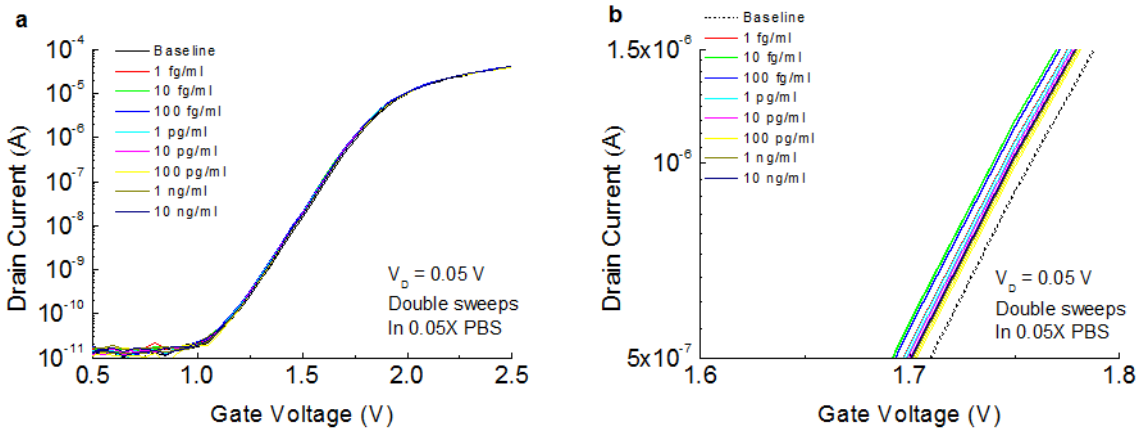

Figure 4.7. (a) Representative transfer curves of anti-suf PSMA with increasing 17-α-HPG concentrations in 0.05× PBS at the gate voltage ranges from 0 to 2.5 V (b) Close-up transfer curves of Figure 4.7a.

All changes in V_R are compared in Figure 4.8. I_R of 1 µA is consistently used in calculating V_R for all the following plots. ΔV_R is normalized with respect to V_{Base} where V_{Base} is V_R of each surface in the pure 0.05× PBS. Figure 4.8 shows ΔV_R for cortisol ranging from 1 fg/ml to 10 ng/ml, sensed by anti-suf PSMA in 0.05× PBS to increase λ_D. The anti-cortisol and cortisol complexes impose negative net charge on the PSMA sensing membrane. Mean ΔV_R values for experimental samples linearly increase by 0.3 % with a R-square of 97.5%, ranging from 1 fg/ml to 10 ng/ml. Random signals are observed for two control setups when adding the same cortisol solutions to sensing gate without any anti-cortisol surface functionalization and adding the same 17-α-HPG concentrations with anti-suf PSMA. The LOD is obtained at the lowest concentration that can be clearly

distinguished from a max fluctuation by any control sample, which is estimated as 1 pg/ml. A higher selectivity appears in higher cortisol concentration levels.

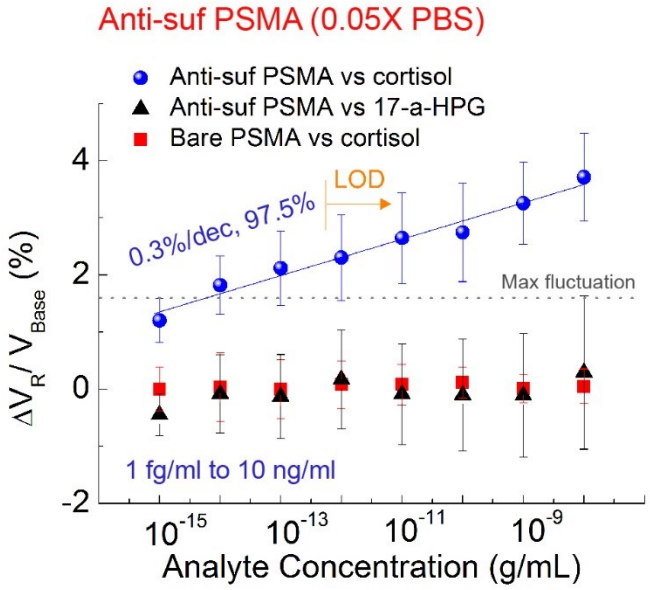

Figure 4.8. ΔV_R distributions of anti-suf PSMA over at least 6 samples in terms of cortisol and 17-α-HPG concentrations in 0.05× PBS. ΔV_R response of the bare PSMA for cortisol is compared.

To confirm sensitivity and specificity shown above, the drift of the RGFET system is evaluated in Figure 4.9 by measuring transfer curve switching voltages with the same frequency after stabilization of the membrane as in the cortisol sensing tests over 50 minutes in 1× and 0.05× PBS. Drift rate of anti-suf PSMA is estimated to be -0.1 %/min and -0.3 %/min for 1× PBS and 0.05× PBS, respectively. In both cases, the drift has a negative slope which is opposite to that of sensitivity curves shown in Figure 4.8.

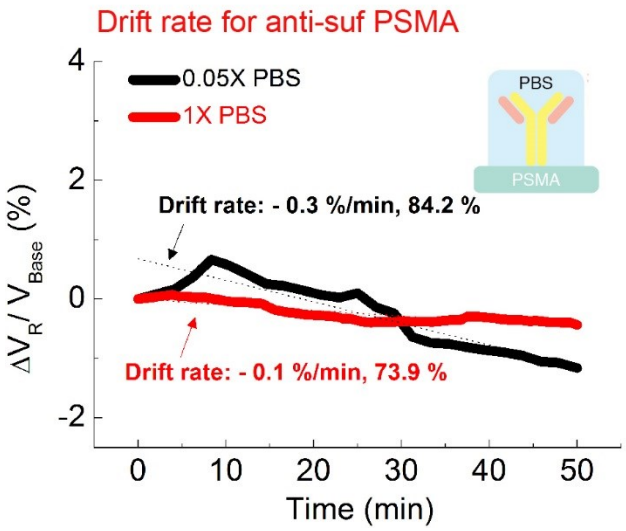

Figure 4.9. Drift rate of anti-suf PSMA measured in 1× and 0.05× PBS by repeating the transfer curve for 50 min after stabilization.

We repeat the same experiments for cortisol detection performed in Figure 4.6 but changing the media from 0.05× PBS to 1× PBS where λ_D is 0.7 nm. Figure 4.10 presents the response of transfer curves from anti-suf PSMA in terms of cortisol concentrations in 1× PBS. After initial increase in V_R, increasing cortisol concentrations reduces V_R steadily.

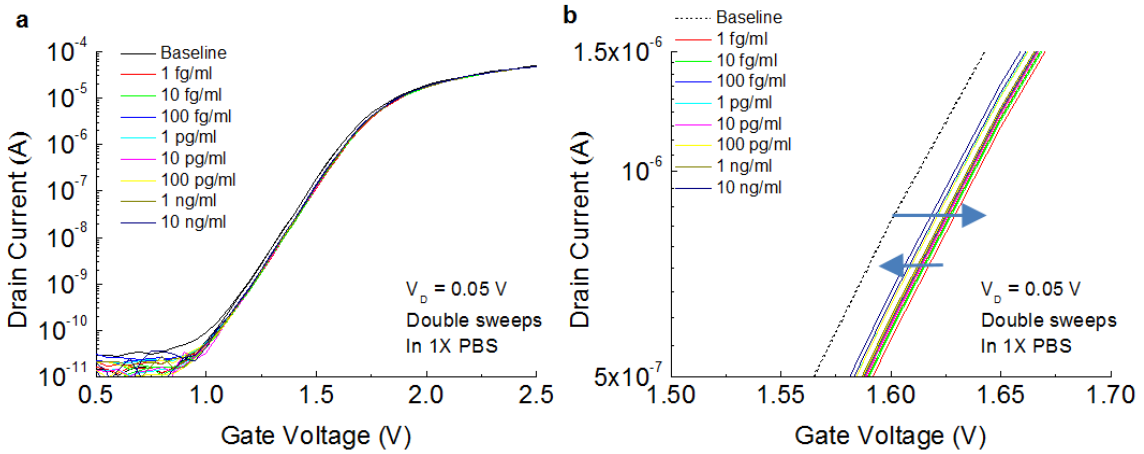

Figure 4.10. (a) Representative transfer curves of anti-suf PSMA with increasing cortisol concentrations in 1× PBS at the gate voltage ranges from 0 to 2.5 V. (b) Close-up transfer curves of Figure 4.10a.

Figure 4.11 shows ΔV_R of anti-suf PSMA with increasing concentrations of cortisol in 1× PBS solution over three samples. A negative slope is observed for increasing cortisol concentrations which is the opposite propensity to that of sensitivity curves shown in Figure 4.9. However, the characteristic of negative slope is similar to that of drift in Figure 4.10. Also, the total amounts of ΔV_R from Figure 4.10 and Figure 4.12 are comparable, indicating the negative slope in Figure 4.12 probably originates from a drift component. As a result, sensing ability of surface-functionalized membrane is limited by the λ_D of the media.

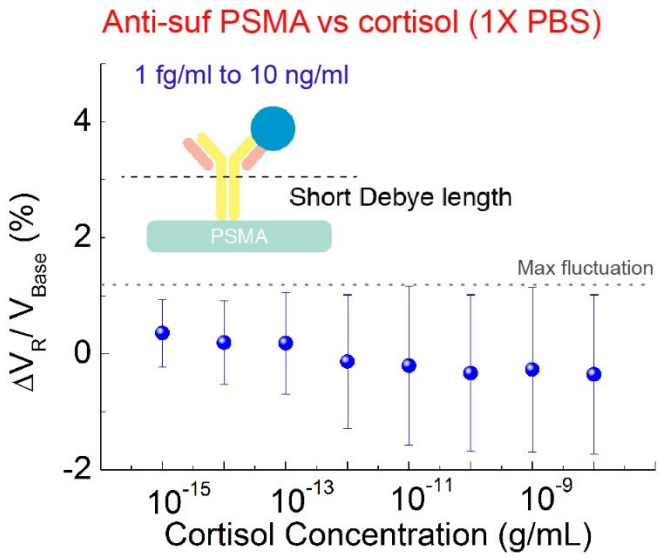

Figure 4.11. ΔV_R distributions of anti-suf PSMA over 3 samples with increasing cortisol concentrations in 1× PBS solution.

4.3.2. Antibody-embedded PSMA

Electric properties of antibody-embedded geometric in PSMA polymer are evaluated in this section. Representative transfer curves from anti-em PSMA that responds to cortisol concentrations are shown in Figure. 4.12. The cortisol measurement is performed in 1× PBS solution instead of 0.05× PBS. Interestingly, shifts in transfer curves correspond to that of anti-suf PSMA in 0.05× PBS shown in Figure 4.6.

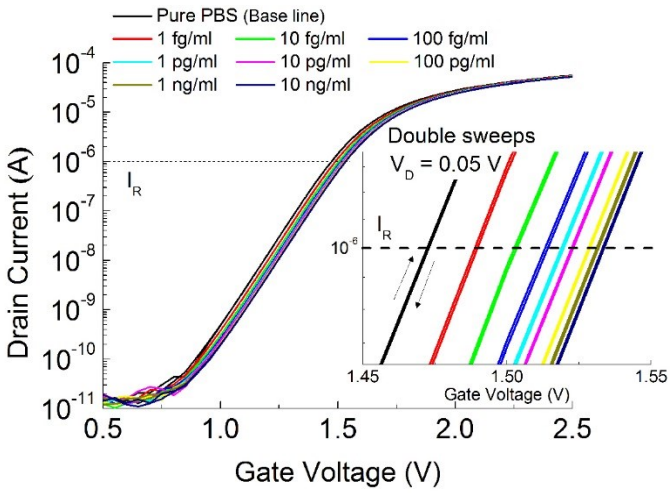

Figure 4.12. Representative transfer curves of anti-suf PSMA with increasing cortisol concentrations in 1× PBS at the gate voltage ranges from 0 to 2.5 V. Inset: close-up transfer curves of Figure 4.12a.

We conducted a specificity test of anti-em PSMA for cortisol by observing non-specific signals from 17-a-HPG. Figure. 4.13 presents representative transfer curves from anti-em PSMA with increasing concentrations of 17-a-HPG. Random shifts in V_R occur.

Drift properties of anti-em PSMA are evaluated in Figure 4.14. ΔV_R drift has a negative slope of -0.6 % min, which is in accordance with the anti-suf PSMA result of Figure 4.9.

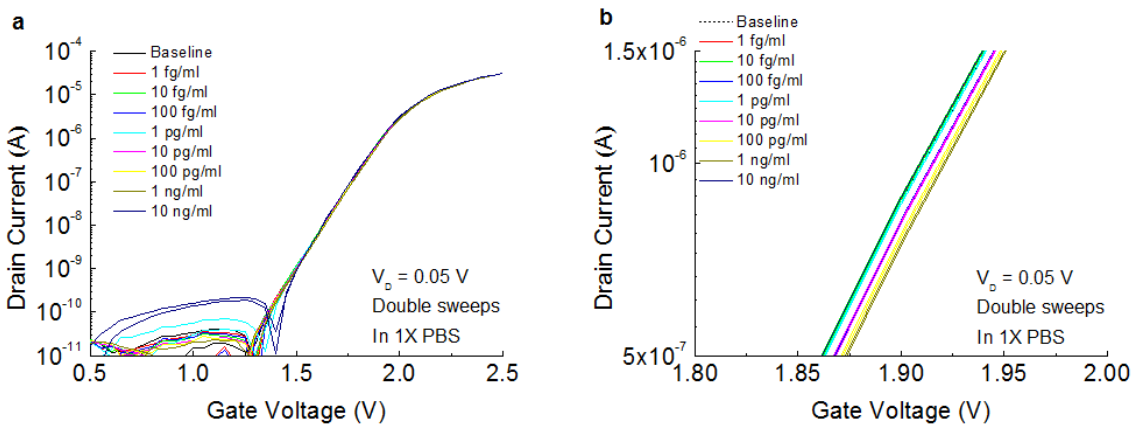

Figure 4.13. (a) Representative transfer curves of anti-em PSMA with increasing 17-a-HPG concentrations in 1× PBS at the gate voltage ranges from 0 to 2.5 V. (b) Close-up transfer curves of Figure 4.13a.

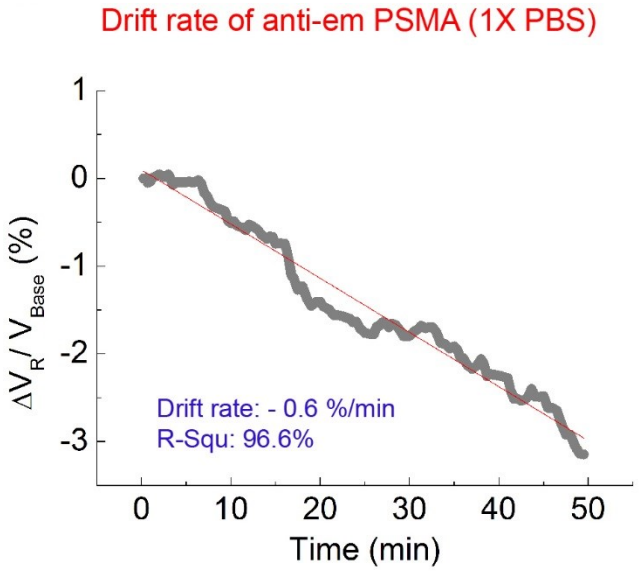

Figure 4.14. Drift rate of anti-em PSMA measured in 1× PBS by repeating the transfer curve for 50 min after stabilization.

Figure 4.15 demonstrates ΔV_R for cortisol and 17-α-HPG ranging from 1 fg/ml to 10 ng/ml measured by anti-em PSMA in 1× PBS. No definite trend for 17-α-HPG is observed. Comparing the control samples, sensitivity of anti-em PSMA for cortisol appears from 10 fg/ml and mean ΔV_R values linearly increase by 0.3 % with a R-square of 94.6%, similar to that of anti-suf PSMA, yet achieved in 1× PBS. LOD is estimated as 1 pg/ml, which is clearly distinguished from a max fluctuation by any control sample. The antibody embedded in polymer matrix leads to detection of charge variations much closer to the membrane-substrate interface, reducing the λ_D constraint on the sensing signal.

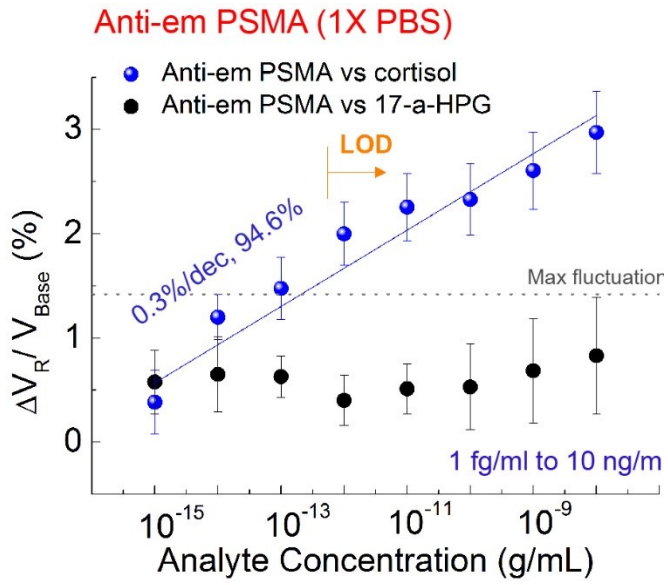

Figure 4.15. ΔV_R distributions of anti-em PSMA over at least 6 samples in terms of cortisol and 17-α-HPG concentrations in 1× PBS.

We further investigate duration of the sensitivity of anti-em PSMA in 1× PBS. The anti-em PSMA samples are stored at 4 °C. Figure 4.16 shows cortisol sensitivity of anti-em PSMA as a function of days stored. Anti-em PSMA samples immediately measured shows stable and uniform sensitivity with small standard deviations depending on specific cortisol concentrations. The sensitivity of anti-em PSMA is maintained up to 1.7 days although a larger standard deviation is shown. However, device sensitivity degrades over two or more days, and shows random signals with lower R-square, corresponding to previously described non-responsive control experiments.

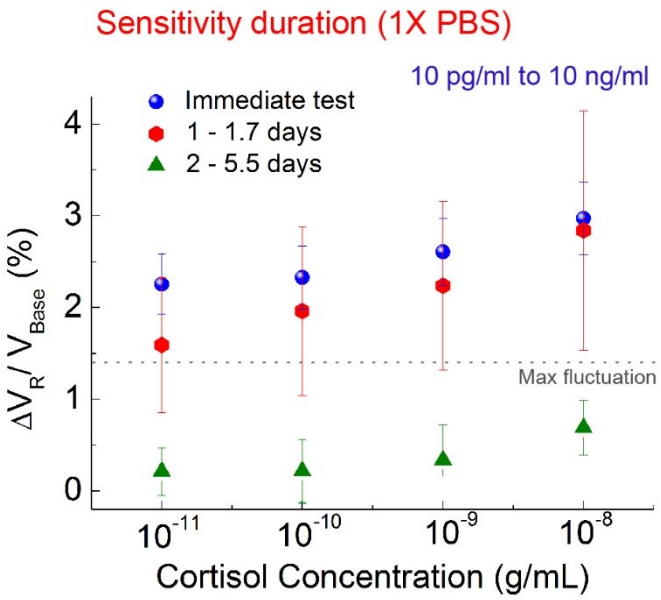

Figure 4.16. Cortisol sensitivity of anti-em PSMA as a function of days stored, in a range of cortisol from 10 pg/mL to 10 ng/mL (10 and 6 samples for immediate and stored samples, respectively).

pH values in human sweat vary from pH2 to 8.2[95]. pH 7.4 of the artificial sweat is chosen for our sweat tests in compliance with the conditions performed above. Also, 10% 1× PBS is added to the artificial sweat as a buffer against changing pH of media to avoid any interference of signal from background media pH[96,97]. Figure 4.17 shows cortisol sensitivity of anti-em PSMA in artificial sweat with pH 7.4 in a range from 1 fg/mL to 100 µg/mL for five samples out of a total of 8. Three other samples give little or no response as separately shown in Figure 4.18.

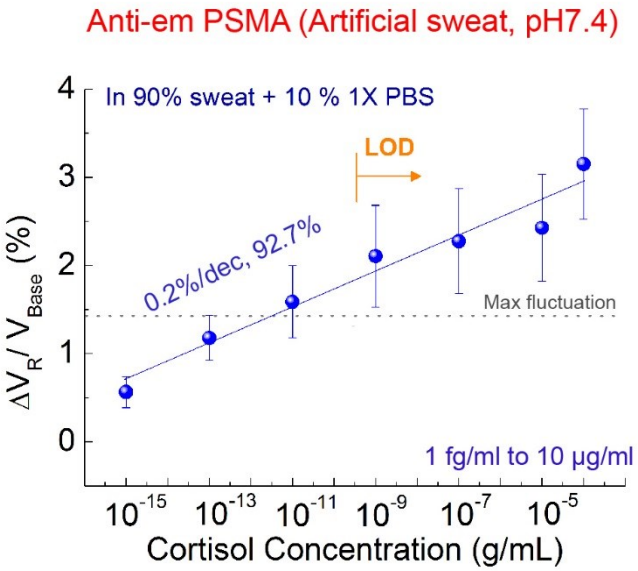

Figure 4.17. Cortisol sensitivity of anti-em PSMA in artificial sweat with pH 7.4 in a range from 1 fg/mL to 100 µg/mL for five samples.

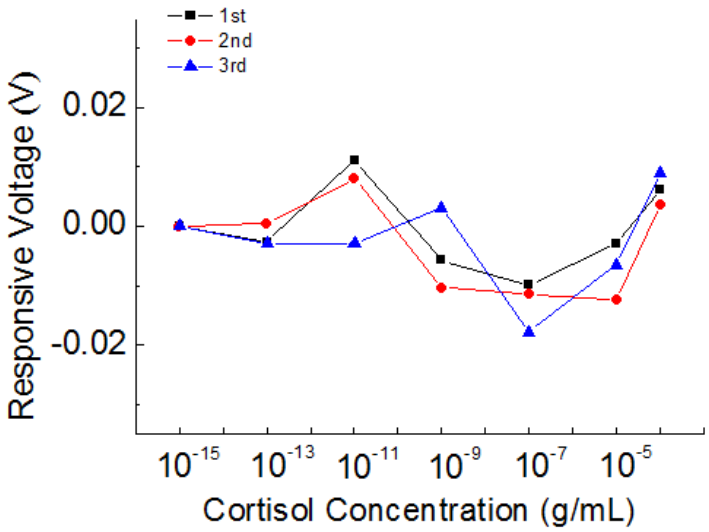

Figure 4.18. V_R vs. different concentrations of cortisol in artificial sweat with pH 7.4 showing random signals from 3 samples out of a total of 8.

While reproducible detection of cortisol in artificial sweat apparently requires greater sample quality control than for simple buffers, 5 samples out of a total of 8 showed a linear response for cortisol in artificial sweat with pH 7.4, in a range from 1 fg/ml to 100 µg/ml (Figure 4.17). LOD approximately estimated by considering the max fluctuation in Figure 4.17 is 1 ng/ml. ΔV_R increases by 0.2 % for every ten folds increase in cortisol concentration, which is smaller than those shown in the PBS solution. One possible reason is that sweat includes more salts and the resultant Debye screening effect would be exponentially larger.

It is noted that the yield to show sensitivity is highly reduced for pure artificial sweat tests without adding 10% PBS (2 samples out of a total of 8) as shown in Figure 4.19.

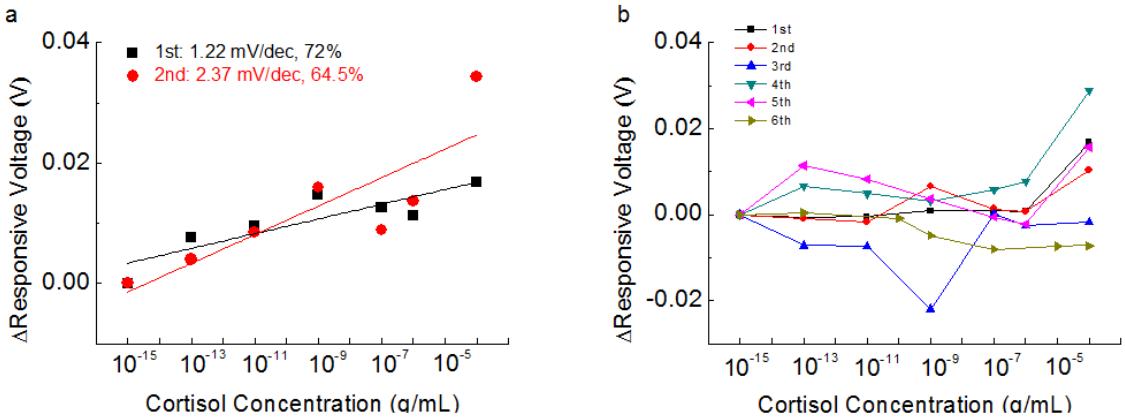

Figure 4.19. (a) Two samples out of a total of 8 showing slight cortisol sensitivity of anti-em PSMA in artificial sweat in a range from 1 fg/mL to 100 µg/mL but without any addition of pH 7.4 buffer solution into artificial sweat. (b) The rest six samples showing no cortisol sensitivity.

In the same context, none of the samples in sweat with pH 4.5 shows sensitivity as shown in Figure 4.20. Sweat with pH 4.5 is diluted by 1× PBS to 10% and 5% where it is still not in the controlled pH regime of background media. 6 samples out of a total of 6 showed random signals in 10% artificial sweat. 4 samples out of a total of 4 showed random signals in 5% artificial sweat.

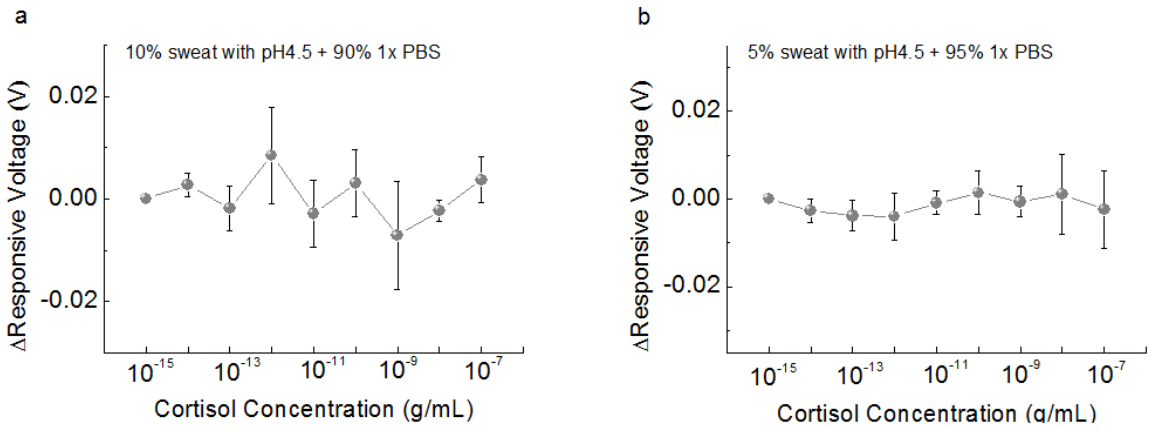

Figure 4.20. V_R vs. different concentrations of cortisol in (a) 10% artificial sweat in (b) 10% artificial sweat with pH 4.5 diluted in 1× PBS.

The sensing mechanism of FET biosensors based on varying isoelectric points causes pH levels to fluctuate in the media, often leading to a different charge distribution on the surface even though the sensors detect the same analyte[78]. This leads to a situation where the various pH levels of the physiological samples have different sensitivities for the same biomarker or produce no of signals, which is one of the huge challenges in clinical applications of FET biosensors in addition to Debye screening length issues[96,97]. The capture-release method mentioned in the introduction could address this issue. Another way is to highly dilute physiological sweat with a reference buffer solution to reach the controlled pH regime. In this case, a higher sensing capacity sensor would be required because the sensor needs to detect lower cortisol concentrations in the highly diluted solution. Detecting analyte in physiological sweat is still challenging because of the reasons mentioned above, but our anti-em PSMA shows the way to ameliorate λ_D constraints

showing sensitivity and selectively for cortisol in controlled artificial sweat even if the λ_D values are less than those in PBS solution.

4.3.3. ELISA results

We confirm sensitivity and specificity of anti-em PSMA by using a standard sandwich ELISA in Figure 4.21. FITC-conjugated antibodies are used as detection antibody. Higher fluorescence intensity (FI) is observed for the standard sandwich ELISA with antibody-antigen-fluorescein complex (Figure 4.21a). However, lower FI is shown for the control samples with a sandwich ELISA excluding cortisol and primary antibody. Similarly, a standard sandwich ELISA with anti-em PSMA-antigen-fluorescein complex (Figure 4.21b) shows higher FI than those of control samples excluding cortisol or replacing cortisol with 17-α HPG for selectivity testing. This confirms that there is significant specificity of binding and that the anti-cortisol protein remains active in anti-em PSMA although the orientation of antibody inside the PSMA polymer may be random.

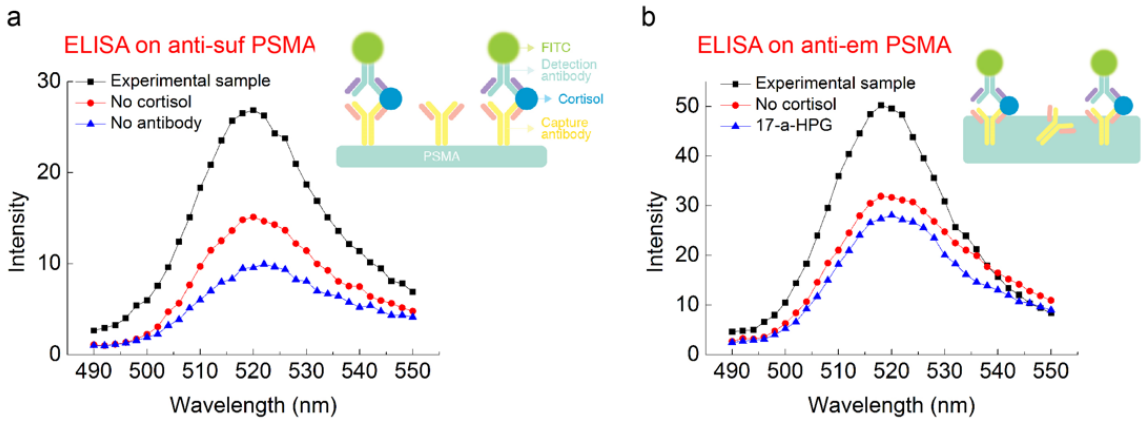

Figure 4.21. (a) FI of FITC-labeled anti-suf PSMA via standard ELISA. Control setups without the addition of cortisol and without the addition of a primary antibody are compared. (b) FI of FITC-labeled anti-em PSMA. Control setups without the addition of cortisol and adding 17-α HPG instead of cortisol are compared.

By considering intensity in ELISA data in Figure 4.22 and intensity from the pure detection antibody including FITC in Figure 4.23, we further estimate the population of active antibody in anti-em PSMA.

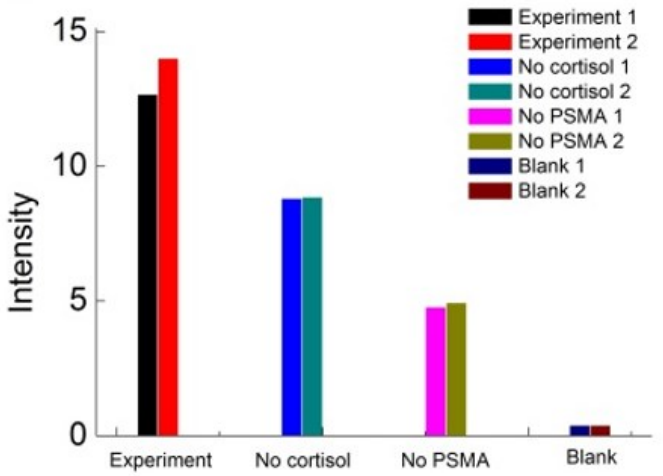

Figure 4.22. Maximum intensity of anti-em PSMA and control samples. Each case is repeated 2 times.

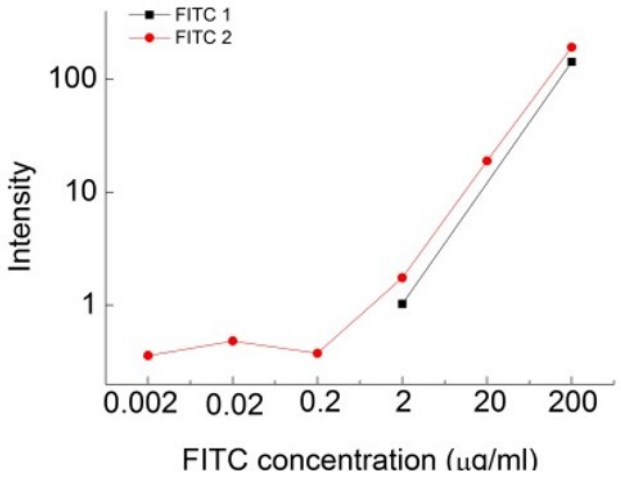

Figure 4.23. Calibration curve is drawn from the pure detection antibody including FITC via two repeated measurements. Intensity of fluorescence is saturated in concentration below 200 pg/ml, which is the detection limit of this ELISA kit.

We approximate the concentration of the activated antibody through ELISA results with following steps:

1. Intensity from detection antibody with cortisol: 13.33 (average)
2. Nonspecific binding fluorescence intensity: 8.85 (average)
3. Fluorescence intensity from blank (system noise): 0.4 (average)
4. Fluorescence intensity from specific binding: $13.33 - 8.85 - 0.4 = 4.08$
5. Intensity of 4.08 is equivalent to 4.33 ug/mL on the calibration plot (Fig. S12c).
6. Multiply sample volume of detection antibody (30 uL) used in calculation plot by 4.33 ug/mL: 0.129 ug active capture antibody in the polymer (presumably corresponding to active antibody in anti-em PSMA)
7. Molecular weight of detection antibody: IgG (150 kg/mol) + FITC (389.382 g/mol). Approximate molecular weight of detection antibody is 150 kg/mol.
8. Mole of antibody would be $\frac{1.29 \times 10^{-6}\text{g}}{1.5 \times 10^{5}\text{g/mol}} = 8.66 \times 10^{-13}$ M
9. The number of antibody would be 8.66×10^{-13} M $\times 6.02 \times 10^{23}$ $\frac{\text{molecules}}{\text{M}} = 5.21 \times 10^{11}$ molecules in anti-em PSMA.
10. Sample size of anti-em PSMA is 0.5 cm by 0.5 cm. Thickness of the polymer is 300 nm. Volume of anti-em PSMA is $0.5\text{ cm} \times 0.5\text{ cm} \times 3 \times 10^{-5}\text{ nm} = 7.5 \times 10^{-3}\text{ cm}^3$.
11. Number density of antibodies is $\frac{5.21 \times 10^{11}\text{ molecules}}{7.5 \times 10^{-3}\text{ cm}^3} = 6.95 \times 10^{13}\ molecules/cm^3$
12. Mass concentration $= \frac{6.95 \times 10^{13}\frac{molecules}{cm^3} \times 1.5 \times 10^{5}\frac{g}{mol}}{6.02 \times 10^{23}\frac{molecules}{mol}} = 17.3\ \mu g/cm^3$
13. 90 ug/ml antibody mixed in PSMA solution (1100 uL).

14. 550 µL out of 1100µL solution spin-coated on PET/ITO substrate (1 x 1.5 cm)
15. Spin-coated film was divided into 6 films (0.5 x 0.5 cm), so 91.6 µL of solution per film
16. The amount of antibody used for each sample $90\frac{\mu g}{mL} \times 91.6\ \mu L = 8.24\ ug$
17. When we assume all antibodies immobilized on antibody-embedded PSMA.
18. About **1.53** % of this antibody was active in the final film.

For anti-em PSMA, orientation of antibody inside the PSMA polymer may be random. The calculation based on ELISA data above indicates active antibodies of 1.53 % in the anti-em PSMA.

4.4. Conclusions

We demonstrate electrical detection of cortisol using RGFET. In particular, the newly proposed anti-em PSMA shows sensitivity from 10 fg/ml to 10 ng/ml in 1× PBS while clear selectivity is shown from 1 pg/ml. Anti-em PSMA is stable up to 1.7 days stored at 4 °C. In our sweat tests, anti-em PSMA showed potential to overcome the λ_D constraint showing LOD of 1 ng/ml in lightly buffered artificial sweat. Specificity of anti-em PSMA is also demonstrated by ELISA. This technique increases the possibility of detecting cortisol in saliva or sweat using transistor biosensors in clinical settings.

As established concepts in the operation mechanism, FET sensors are known to detect the change in pI upon binding events on the sensing part. Inevitably, the operation of typical FET sensors is associated with issues of λ_D [75] and pH interference of background media[96,97]. In particular, λ_D arising from the interaction between the sensing surface and electrolyte makes sensors apparently unresponsive to analyte when physical lengths of antibody−antigen complexes are more than λ_D associated with physiological media.

4.5. References

(67) Kokot, G.; Bespalova, M. I.; Krishnan, M. *Journal of Chemical Physics* **2016**, *145*.

(68) Zheng, G.; Patolsky, F.; Cui, Y.; Wang, W. U.; Lieber, C. M. *Nat Biotechnol* **2005**, *23*, 1294.

(69) Lee, I. K.; Lee, K. H.; Lee, S.; Cho, W. J. *ACS applied materials & interfaces* **2014**, *6*, 22680.

(70) Zhou, G.; Chang, J.; Cui, S.; Pu, H.; Wen, Z.; Chen, J. *ACS applied materials & interfaces* **2014**, *6*, 19235.

(71) Huang, W. G.; Besar, K.; LeCover, R.; Dulloor, P.; Sinha, J.; Hardigree, J. F. M.; Pick, C.; Swavola, J.; Everett, A. D.; Frechette, J.; Bevan, M.; Katz, H. E. *Chemical Science* **2014**, *5*, 416.

(72) Zheng, G. F.; Patolsky, F.; Cui, Y.; Wang, W. U.; Lieber, C. M. *Nature Biotechnology* **2005**, *23*, 1294.

(73) Patolsky, F.; Zheng, G.; Lieber, C. M. *Nat Protoc* **2006**, *1*, 1711.

(74) Jang, H. J.; Ahn, J.; Kim, M. G.; Shin, Y. B.; Jeun, M.; Cho, W. J.; Lee, K. H. *Biosensors & Bioelectronics* **2015**, *64*, 318.

(75) Stern, E.; Wagner, R.; Sigworth, F. J.; Breaker, R.; Fahmy, T. M.; Reed, M. A. *Nano Letters* **2007**, *7*, 3405.

(76) Huang, W. G.; Diallo, A. K.; Dailey, J. L.; Besar, K.; Katz, H. E. *Journal of Materials Chemistry C* **2015**, *3*, 6445.

(77) Elnathan, R.; Kwiat, M.; Pevzner, A.; Engel, Y.; Burstein, L.; Khatchtourints, A.; Lichtenstein, A.; Kantaev, R.; Patolsky, F. *Nano Lett* **2012**, *12*, 5245.

(78) Makowski, M. S.; Ivanisevic, A. *Small* **2011**, *7*, 1863.

(79) Stern, E.; Vacic, A.; Rajan, N. K.; Criscione, J. M.; Park, J.; Ilic, B. R.; Mooney, D. J.; Reed, M. A.; Fahmy, T. M. *Nat Nanotechnol* **2010**, *5*, 138.

(80) Ohno, Y.; Maehashi, K.; Matsumoto, K. *Journal of the American Chemical Society* **2010**, *132*, 18012.

(81) Khatayevich, D.; Page, T.; Gresswell, C.; Hayamizu, Y.; Grady, W.; Sarikaya, M. *Small* **2014**, *10*, 1505.

(82) Lo, Y. S.; Nam, D. H.; So, H. M.; Chang, H.; Kim, J. J.; Kim, Y. H.; Lee, J. O. *ACS Nano* **2009**, *3*, 3649.

(83) Munje, R. D.; Muthukumar, S.; Panneer Selvam, A.; Prasad, S. *Sci Rep* **2015**, *5*, 14586.

(84) Stevens, R. C.; Soelberg, S. D.; Near, S.; Furlong, C. E. *Anal Chem* **2008**, *80*, 6747.

(85) Kumar, A.; Aravamudhan, S.; Gordic, M.; Bhansali, S.; Mohapatra, S. S. *Biosens Bioelectron* **2007**, *22*, 2138.

(86) Kaushik, A.; Vasudev, A.; Arya, S. K.; Pasha, S. K.; Bhansali, S. *Biosens Bioelectron* **2014**, *53*, 499.

(87) Singh, A.; Kaushik, A.; Kumar, R.; Nair, M.; Bhansali, S. *Appl Biochem Biotechnol* **2014**, *174*, 1115.

(88) Kinnamon, D.; Ghanta, R.; Lin, K. C.; Muthukumar, S.; Prasad, S. *Sci Rep* **2017**, *7*, 13312.

(89) Russell, E.; Koren, G.; Rieder, M.; Van Uum, S. H. *Ther Drug Monit* **2014**, *36*, 30.

(90) Rehan, M.; Younus, H. *Int J Biol Macromol* **2006**, *38*, 289.

(91) Jang, H. J.; Gu, J. G.; Cho, W. J. *Sensors and Actuators B-Chemical* **2013**, *181*, 880.

(92) Lee, I. K.; Jeun, M.; Jang, H. J.; Cho, W. J.; Lee, K. H. *Nanoscale* **2015**, *7*, 16789.

(93) Rozanski, A.; Blumenthal, J. A.; Kaplan, J. *Circulation* **1999**, *99*, 2192.

(94) Rozanski, A.; Bairey, C. N.; Krantz, D. S.; Friedman, J.; Resser, K. J.; Morell, M.; Hiltonchalfen, S.; Hestrin, L.; Bietendorf, J.; Berman, D. S. *New England Journal of Medicine* **1988**, *318*, 1005.

(95) Harvey, C. J.; LeBouf, R. F.; Stefaniak, A. B. *Toxicology in Vitro* **2010**, *24*, 1790.

(96) Hammock, M. L.; Knopfmacher, O.; Naab, B. D.; Tok, J. B. H.; Bao, Z. A. *Acs Nano* **2013**, *7*, 3970.

(97) Khan, H. U.; Jang, J.; Kim, J. J.; Knoll, W. *Journal of the American Chemical Society* **2011**, *133*, 2170.

Chapter 5

Conclusion and Future Outlook

By using the RGFET characterization, we investigated diverse fundamental mechanisms of electrochemical interactions from (1) molecular doping effects in a conjugated polymer, (2) solution interfaces, and (3) biological interfaces associated with Debye length issues.

In Chapter 2, we showed self-consistency in spectroscopic, conductivity, and RGFET characterization of assaying the interfacial interactions between surface electron donors and electron acceptor molecules bound from solution. RGFET characterization provided a new way to calculate hole concentrations in a doped polymer in terms of $\Delta V_{th,RG}$ depending on dopant concentrations of F4TCNQ on conjugated polymer P3HT surfaces. F4TCNQ occupies sites on electron donor surfaces by creating surface dipoles and the associated hole carriers imposed positive charges in P3HT, which were detected by the RGFET system. The data add significant insight about the mechanism of "sequential doping" of conductive polymers, under consideration as an approach to increase their conductivity and preserving their mobility while doping.

Also, a remarkable analogy between polymer doping and surface dipole formation at electrodes was found, while no effects were observed on fully insulating films, as expected. Finally, the electroanalytical RGFET system was demonstrated as a means of measuring diffusion rates of small molecules through inert polymer films as we monitored physical diffusion of F4TCNQ in polystyrene driven by concentration gradients. This analysis provides a new electronic analysis tool to describe doping effects and diffusion in organic materials and this technique could be further expanded to diverse fields such as

surface science, conducting polymers, electroanalytical chemistry, and polymer science more broadly

In Chapter 3, we investigated how drift and hysteresis varied according to different surface polarities and solution dipole moments in an RGFET system. Fast, stable orientational ordering of dipoles on charged surfaces increased electrochemical stability. Therefore, charged conjugated polymers with physical stability in aqueous solution are recommended for use in biosensing layers. We demonstrated that P3HT and PT-COOH had superior electrochemical stability, almost comparable to that of ITO. Also, the pH sensitivity of P3HT (17 mV/pH) is demonstrated, presumably occurring by ionic doping. The pH sensitivity of PT-COOH is further increased due to the incorporation of additional ionizable functionalities (30 mV/pH).

Our results suggest a criterion in designing new polymers for biosensing interfaces requiring receptor attachment combining conjugation and charged components in the materials in order to rapidly equilibrate solution dipole moments with the applicatoin of E_F. This criterion is in fact met by PEDOT-PSS and related polymers now used in organic electrochemical transistors, and is now suggested even for sensing layers that interact with analytes purely by polarization mechanisms.

In Chapter 4, we introduced a way to overcome Debye length issues by using newly proposed polymer sensing membranes incorporating antibodies in the polymer. To be specific, we compared sensing signals from a polymer sensing layer with antibody functionalization either on the top surface or within the bulk. The response to cortisol in sweat is only shown for antibody-embedded polymer sensing layer, likely because the binding occurs with less Debye screening of the gate electrode. To the best of our

knowledge, the sensitivity to cortisol is the highest yet reported. Non-responses in the absence of the antibody, or when a different steroid is used as the control analyte, offered evidence of selectivity. Increased fluorescence of a detection antibody after cortisol binding to its capture antibody also supports the activity of the capture antibody bound to the polymer. We further estimated the population of active antibody in anti-em polymer based on ELISA result.

Antibody-embedded sensing membrane is a platform technology that can be applicable for diverse FET biosensors designed for detecting bio-makers in physiological samples. This concept may have an immense effect on positioning FET biosensors for clinical settings as an alternative for the optical immunoassay.

Appendix

Biography

Hyun-June Jang was born on the 31th of July 1986 in Seoul, South Korea. He received his B.E. and M.E. degrees in Electronic Materials Engineering from Kwangwoon University, Seoul, Korea, in 2011 and in 2013, respectively. During those studies, he proposed a way to increase electrochemical stability and sensitivity of ion-sensitive FETs (ISFET) by employing the dual-gate structure in the ISFETs. In particular, he discovered that an ultra-thin film in the semiconducting layer (ca. 5 nm) caused stronger capacitive coupling effects over dual-gate structure, which led to higher stability and sensitivity beyond the performance of a conventional ISFET

He worked as a research scientist at the Korea Institute of Science and Technology in 2014. He developed a concept of electrical ELISA by combining the ISFET and ELISA. The newly developed platform holds a large potential for point-of-care tools in a variety of infectious diseases, without being limited by the need for expensive equipment for optical ELISA.

He also worked as a research scientist at the Korea Research Institute of Bioscience & Biotechnology in 2015. He established a new top-down approach in fabricating nanowire of inorganic amorphous oxide semiconductors (AOSs) without using any chemical or plasma etching processes. As proof-of-concept, he demonstrated the fabrication of laterally oriented nanowires of indium-gallium zinc oxide (IGZO) on the polyimide substrate. He presented outstanding mobility of 132 cm^2/Vs from the thin-film transistor of IGZO nanowire on SiO_2 substrate under the maximum processing temperature of 85°C.

Since 2015, he has been carrying out graduate research in Materials Science and Engineering at the Johns Hopkins University. He proposed a new analytical platform that determines charge carrier density and mobility in a conductive polymer film by using a remote-gate FET (RGFET) detection setup. He reported that the RGFET can monitor the kinetics of diffusion of small molecules in a passive polymer such as polystyrene. This platform holds the potential to add insight into doping effects and inter-diffusions in diverse organic/polymer films with non-spectroscopic characterization.

Curriculum Vita

EDUCATION

Aug. 2015 – Present	Ph.D. candidate, Materials Science and Engineering Johns Hopkins University
Feb. 2013 – Mar. 2011	M. E., Electronic Materials Engineering Kwangwoon University, Seoul, Korea
Feb. 2011 – Mar. 2005	B. E., Electronic Materials Engineering Kwangwoon University, Seoul, Korea

WORK EXPERIENCE

Feb. 2015 – Jul. 2015	Research Scientist, Bionanotechnology Research Center Korea Research Institute of Bioscience & Biotechnology, Daejeon, Korea
Feb. 2014 – Jan. 2015	Research Scientist, Biomedical nano-Monitoring Lab. Korea Institute of Science and Technology, Seoul, Korea

PEER-REVIEWED PUBLICATIONS

29. **Jang, H.-J**.; Wagner, J.; Song, Y.; Lee, T.; Zhang, Q. Katz, H. E. "Carboxylic Acid-Functionalized Conjugated Polymer Promoting Diminished Electronic Drift and Amplified Proton Sensitivity of Remote Gates Compared to Nonpolar Surfaces in Aqueous Media" (submitted)
28. Wagner, J.; **Jang, H.-J**.; Han, J; Katz, H. E. "Enhanced and unconventional responses in chemiresistive sensing devices for nitrogen dioxide and ammonia from carboxylated alkylthiophene polymers", *Mater. Horiz*, in press, (2020), DOI: 10.1039/D0MH00049C
27. **Jang, H.-J**.; Wagner, J.; Li, H.; Zhang, Q.; Mukhopadhyaya, T.; Katz, H. E. "Analytical Platform To Characterize Dopant Solution Concentrations, Charge Carriers Densities in Films

and Interfaces, and Physical Diffusion in Polymers Utilizing Remote Field-Effect Transistors" *J. Am. Chem. Soc.,* 141, 4861-4869 (2019)

26. Li, H.; Shi, W.; Song, J.; **Jang, H.-J**.; Dailey, J.; Yu, J.; Katz, H. E. "Chemical and biomolecule sensing with organic field-effect transistors" *Chem. Rev.*, 119, 3-35 (2019)
25. Huang, J.; Li, H.; Kirksey, E.; Hoffman, C.; **Jang, H.-J**.; Wagner, J.; Madan, D.; Katz, H. E. "Contributions to composite conductivity and Seebeck coefficient in commercial Bi_2Te_3-Conjugated polymer composites" *J. Appl. Phys*. 125, 12550 (2019)
24. Dailey, J.; Li, H. Song; J, Besar; K. **Jang; H.-J**; Chu Y.; Katz, H. E. "Material and circuit design for organic electronic vapor sensors and biosensors" *SPIE: Organic and Hybrid Sensors and Bioelectronics XII*, 11096, 110960A (2019)
23. **Jang, H.-J**.; Lee, T.; Song, J.; Russell, L.; Li, H.; Dailey, J.; Searson, P. C.; Katz, H. E. "Electronic Cortisol Detection Using an Antibody-Embedded Polymer Coupled to a Field-Effect Transistor" ACS *Appl. Mater. Interfaces*, 10, 16233-16237 (2018)
22. Song, J.; Dailey, J.; Li, H.; **Jang, H.-J**.; Russell, L.; Zhang, P.; Searson, P. C.; Wang, J. T.-H.; Everett, A. D.; Katz, H. E. "Influence of Bioreceptor Layer Structure on Myelin Basic Protein Detection using Organic Field Effect Transistor-Based Biosensors" *Adv. Funct. Mater*. 28, 1802605 (2018)
21. **Jang, H.-J**.; Lee, K. J.; Jo, K.-W.; Katz, H. E.; Cho, W.-J.; Shin, Y.-B. "Top-down Fabrication and Enhanced Active Area Electronic Characteristics of Amorphous Oxide Nanoribbons for Flexible Electronics" *Sci. Rep*., 7, 5728 (2017)
20. Song, J.; Dailey, J.; Li, H.; **Jang, H.-J**.; Zhang, P.; Wang, J. T.-H.; Everett, A. D.; Katz, H. E. "Extended Solution Gate OFET-Based Biosensor for Label-Free Glial Fibrillary Acidic Protein Detection with Polyethylene Glycol-Containing Bioreceptor Layer" *Adv. Funct. Mater*., 27, 1606506 (2017)
19. Ireland, R. M.; Jones, T.; Li, H.; **Jang, H.-J**.; West, J. E.; Katz, H. E. "Statically Charged Electret Polymers as Solid, Nonvolatile Gates Encapsulating and Tuning Polymer Thermoelectric Parameter" *ACS Energy Lett*., 1, 612–617 (2016)
18. **Jang, H.-J**.; Ahn, J.; Kim, M.-G.; Shin, Y.-B.; Jeun, M.; Lee, K. H.; Cho, W.-J. "Electrical Signaling of Enzyme-Linked Immunosorbent Assays with an Ion-Sensitive Field-Effect Transistor" *Biosens. Bioelectron*., 64, 318-323 (2015)
17. Lee, I.-K.; Jeun, M.; **Jang, H.-J**.; Cho, W.-J.; Lee, K. H. "A self-amplified transistor immunosensor under dual gate operation: highly sensitive detection of hepatitis B surface antigen, *Nanoscale* 7, 16789-16797 (2015)

16. **Jang, H.-J**.; and Cho, W.-J. "Performance Enhancement of Capacitive-Coupling Dual-gate Ion-Sensitive Field-Effect Transistor in Ultra-Thin-Body" *Sci. Rep.,* 4, 5248 (2014)
15. Oh, J. Y.; Park, J.-T.; **Jang, H.-J**.; Cho, W.-J.; Islam, M. S. "3D-Transistor Array Based on Horizontally Suspended Silicon Nano-Bridges Grown via a Bottom-up Technique" *Adv. Mater*., 26, 1929-1934 (2014)
14. Park, J.-K.; **Jang, H.-J**.; Park, J.-T.; Cho, W.-J. "SOI Dual-gate ISFET with Variable Oxide Capacitance and Channel Thickness" *Solid-State Electron*., 97, 2-7 (2014)
13. Lau, H.-C.; Bae, T.-E.; **Jang, H.-J.**; Kwon, J.-Y.; Cho, W.-J.; Lim, J.-O. "Saliva-Based Screening Approach for Alzheimer's Disease via the Cell-Oriented Ion-Sensitive Field-Effect Transistor" *Sens. Lett.,* 12, 1096-1101 (2014)
12. **Jang, H.-J**.; Gu, J.-G.; Cho, W.-J. "Sensitivity Enhancement of amorphous InGaZnO Thin Film Transistor based Extended Gate Field-Effect Transistors with Dual-Gate Operation" *Sens. Actu. B*, 181, 880-884 (2013)
11. Lau, H.-C.; Bae, T.-E.; **Jang, H.-J**.; Kwon, J.-Y.; Cho, W.-J.; Lim, J.-O. "Biomimetic Trehalose Biosensor Using Gustatory Receptor (Gr5a) Expressed in Drosophila Cells and Ion-Sensitive Field-Effect Transistor" *Jpn. J. Appl. Phys*., 52, 04CL02 (2013)
10. Bae, T.-E.; **Jang, H.-J**.; Yang, J.-H.; Cho, W.-J. "High Performance of Silicon Nanowire Based Biosensors using a High-k Stacked Sensing Membrane" *ACS Appl. Mater. Interfaces,* 5, 5214-5218 (2013)
9. Jang, K.-H.; **Jang, H.-J**.; Park, J.-K.; Cho, W.-J. "Self-Amplified Dual Gate Charge Trap Flash Memory for Low Voltage Operation" *IEEE Elect. Dev. Lett.,* 34, 756-758 (2013)
8. Bae, T.-E.; **Jang, H.-J**.; Lee, S.-W.; Cho, W.-J. "Enhanced Sensing Properties by Dual-Gate Ion-Sensitive Field-Effect Transistor Using the Solution-Processed Al_2O_3 Sensing Membrane" *Jpn. Appl. Phys*., 52, 06GK03 (2013)
7. **Jang, H.-J**.; and Cho, W.-J. "Fabrication of High-Performance Fully Depleted Silicon-on-Insulator Based Dual-Gate Ion-Sensitive Field-Effect Transistor Beyond the Nernstian Limit" *Appl. Phys. Lett*., 100, 073701-4 (2012)
6. **Jang, H.-J**.; Bae, T.-E.; Cho, W.-J. "Improved Sensing Performance of Polycrystalline-Silicon Based Dual-Gate Ion-Sensitive Field-Effect Transistors Using High-k Stacking Engineered Sensing Membrane" *Appl. Phys. Lett*., 100, 253703-4 (2012)
5. **Jang, H.-J**.; and Cho, W.-J. "Fabrication of High Performance Ion-Sensitive Field-Effect Transistors Using an Engineered Sensing Membrane for Bio-Sensor Application" *Jpn. Appl. Phys*., 51, 02BL05 (2012)

4. Oh, J. Y.; **Jang, H.-J**.; Cho, W.-J.; Islam, M. S. "Highly Sensitive Electrolyte-Insulator-Semiconductor pH Sensors Enabled by Silicon Nanowires with Al_2O_3/SiO_2 Sensing Membrane" *Sens. Actu. B*, 171-172, 238-243 (2012)
3. Oh, J. Y.; **Jang, H.-J**.; Cho, W.-J.; Pala, N.; Islam, M. S. "Silicon Nanowire Integrated Electrolyte-Insulator-Semiconductor Sensor with an Above-Nernstian Sensitivity for Bio-Sensing Applications" *Mater. Res. Soc. Proc*., 1439, 127-132 (2012)
2. **Jang, H.-J**.; and Cho, W.-J. "High Performance Silicon-on-Insulator Based Ion-Sensitive Field-Effect Transistor Using High-k Stacked Oxide Sensing Membrane" *Appl. Phys. Lett.*, 99, 043703-3 (2011)
1. **Jang, H.-J**.; Kim, M.-S.; Cho, W.-J. "Development of Engineered Sensing Membranes for Field-Effect Ion-Sensitive Devices Based on Stacked High-k Dielectric Layers" *IEEE Elect. Dev. Lett.*, 32, 973-975 (2011)

BOOK CHAPTER

1. Li, H.; Shi, W.; Dailey, J.; **Jang, H.-J**.; Song, J. Yu, J.; Katz, H. E. "Vapor sensing using organic, polymer, and nanomaterial field-effect transistors" Handbook of Organic Materials for Electronic and Photonic Devices, 785-815

SLECTED PRESENTATIONS

6. **Jang, H.-J**.; Wagner, J.; Li, H.; Zhang, Q.; Lee, T.; Song, J.; Katz, H. E. "Sensing applications of remote-gate field-effect transistor combining polymer sensing membrane" Materials Research Society (MRS), USA, Nov., 2018.
5. **Jang, H.-J**.; Moon, S.-W.; Cho, W.-J. "Signal Amplification of Immune-Field-Effect Transistors Using Enzyme Catalyzed Ag Reduction to Overcome Debye Screening Length" Solid State Devices and Materials (SSDM), Japan, Sep., 2014.
4. **Jang, H.-J**.; Park, J.-T.; Cho, W.-J. "Enhancement of Sensing Performance on Dual-Gate Ion-Sensitive Field-Effect Transistors using Ultra-Thin Body Silicon-on-Insulator" EUROSOI 2013, Paris, Jan., 2013.
3. **Jang, H.-J**.; and Cho, W.-J. "Signal Enhancement of Human IL5 Immunoassay by Enzyme Catalyzed Ag Reduction Beyond Limit of Debye Screening Length on Ion-Sensitive Field Effect Transistors" SSDM, Japan, Sep., 2012.

2. **Jang, H.-J.**; Cho, W.-J.; Oh, J.; Islam, M. S. "High Sensitive Dual- Gate SOI based Ion-Sensitive Field-Effect Transistor beyond Nernst limit of 59 mV/pH for Biosensor Application" MRS, USA, Apr., 2012.
1. **Jang, H.-J**.; Kim, M.-S.; Cho, W.-J. "Realization of Ion-Sensitive Field-Effect Transistor on SOI substrate with Engineered Sensing Membrane for High Stability" SSDM, Japan, Sep., 2011

TEACHING EXPERIENCE

Sep. 2017 – Dec. 2017	Teaching assistant (laboratory), Nanomaterials Lab Johns Hopkins University, Course #: EN.510.442.01.FA17
Jul. 2017 – Aug. 2017	Teaching assistant (laboratory), Women in Science and Engineering (WISE) Summer Internship, Johns Hopkins University
Jan. 2017 – May. 2017	Teaching assistant, Micro and Nano Structured Materials & Device, Johns Hopkins University, Course #: EN.510.422.01.SP17